Feasibility studies of the $\overline{p}p \rightarrow \pi^{\circ}e^{+}e^{-}$ electromagnetic channel at $\overline{\mathrm{P}}$ANDA

Dissertation
submitted to attain the academic degree

**"Doctor
of Natural Sciences"**

at the Department of Physics, Mathematics and Computer Science
of the Johannes Gutenberg University
Mainz

Jérôme Boucher
born in Châtenay-Malabry

Mainz 2011

Contents

Chapter 1

Introduction

The phenomena of the confinement of quarks, the existence of glueballs and hybrids and the origin of the mass of strongly interacting, composite systems are long-standing puzzles and represent a challenge in our attempt to understand the nature of the strong interaction and of the hadronic matter. The strong force governs the microscopic structure of the matter. It bounds the nucleons within the atomic nucleus. It also determines the interaction between the quarks within the nucleon and other hadrons.

Among all possible realizations of quark and antiquark assembly, the nucleon (the proton and the neutron), is the most stable of all hadrons and consequently has been the subject of intensive studies. Mass, shape, radius and more complex representations of its internal structure are measured since several decades using different probes.

The electron elastic scattering has played a major role in the quest for understanding the intimate nature of the proton. As early as 1953, electron elastic scattering experiment were performed at the Stanford Linear Accelerator Center (SLAC).

The composite structure of the proton was shown in the 1956 at SLAC. Since then a whole set of tools (elastic scattering, deep inelastic scattering, exclusive and inclusive scattering, polarization observables), has allowed a breakthrough on its structure. The hadron form factors are considered fundamental quantities as they characterize the internal structure of a non point-like particle. A particle of spin S is parametrized by 2S+1 form factors. The proton (S=1/2) is then described by 2 form factors traditionally the electric G_E and magnetic G_M form factors. G_E and G_M are function of one kinematical variable q^2 related to the internal distance. Schematically, at large distances (low energy), they are interpreted in terms of charge and magnetic distributions and at small distances (high energy) they probe the quark and gluon structure.

The simplest way to measure the proton form factors consists in measuring the angular distribution of the electron-proton elastic scattering accessing the so-called Space-Like region where $q^2 \leq 0$. Using the crossed channel $\overline{p}p \leftrightarrow e^+e^-$, one accesses another kinematical region, the called Time-Like region where $q^2 > 0$. However, the $\overline{p}p \leftrightarrow e^+e^-$ has a threshold q^2_{th}. Consequently, within this reaction only the kinematical domain $q^2 > q^2_{th}$ is available. To access the region below the threshold so-called unphysical region, one

may use the $\overline{p}p \to \pi^\circ e^+ e^-$ reaction where the π° take away a part of the system energy allowing q^2 to be varied between q^2_{th} and almost 0.

The study of the nucleon structure using electromagnetic processes is one of the research fields of the $\overline{\text{P}}$ANDA project to be installed at the future Facility fo Antiproton and Ion Research (FAIR).

The present thesis aims to show the feasibility of the proton electromagnetic form factor measurements using the $\overline{p}p \to \pi^\circ e^+ e^-$ reaction. It also comprises a technical work dedicated to the study of the $\overline{\text{P}}$ANDA electromagnetic calorimeter.

After this introduction, the second chapter presents both FAIR experimental program and the FAIR facility. Then, the $\overline{\text{P}}$ANDA physics program is detailed and finally the description of the $\overline{\text{P}}$ANDA detector is given with an emphasis on the electromagnetic calorimeter.

The third chapter summarizes the present knowledge on the nucleon electromagnetic form factors. I start by presenting the different kinematical domain and the nucleon electromagnetic form factors. Then extraction methods are described and the world data are displayed. Finally, model predictions and foreseen measurements are discussed.

The fourth chapter focuses on the $\overline{p}p \to \pi^\circ e^+ e^-$ reaction. The kinematics of this 3-body final state is detailed. Then an overview of the existing models is given. While the very first calculation based on one nucleon exchange is presented, I show why it was necessary to extend the model.

The fifth chapter deals with the feasibility studies. Background channels are first listed. Then a model for $\overline{p}p \to \pi^\circ \pi^+ \pi^-$ is presented and background rejection factors are shown. Finally, estimates for the signal contamination are given and the proton electromagnetic form factors are extracted from electron angular distributions.

A part of this work was devoted to experimental aspects. Indeed, in a reaction like $\overline{p}p \to \pi^\circ e^+ e^-$ where $\pi^\circ \to \gamma\gamma$ at almost 100%, it is important to cover the overall phase space as much as possible and to understand the resolution of the detectors which contribute the most to the identification of electrons, positrons and photons.

The sixth chapter is devoted to backward end cap electromagnetic calorimeter and the determination of its resolution and efficiency.

The seventh chapter is dedicated to the prototype of the barrel electromagnetic calorimeter. After a brief description of the prototype, the calibration method is presented. Finally, the prototype resolution is shown.

The eighth chapter ends this thesis work, results are summarized. The conclusions and outlook are then derived.

Chapter 2

The $\overline{\text{P}}$ANDA project at FAIR

2.1 Facility for Antiproton and Ion Research

The concept for the FAIR facility (Facility for Antiproton and Ion Research, [1]) is based on extensive discussions over a period of several years. It also adopted priority recommendations from high level science committees.

2.1.1 The FAIR experimental program

The general goals and scientific objectives can be grouped into four fields: physics with high energy antiprotons, nuclear matter physics, NuSTAR physics (Nuclear Structure, Astrophysics and Reactions) and APPA physics (Atomic, Plasma Physics and Applications).

The $\overline{\text{P}}$ANDA (anti$\overline{\text{P}}$roton ANnihilation at DArmstadt) collaboration aims to study fundamental questions of hadron and nuclear physics using interactions of high energy antiprotons with nucleons and nuclei (see section 2.2 and [2]). The physics of strange and charmed quarks will be accessible with unprecedented accuracy hence allowing tests of the strong interaction.

The nuclear matter physics will be explored by the CBM (Compressed Baryonic Matter, see [3]) collaboration. CBM aims at the investigation of strongly interacting matter at very high density in relation with the questions of deconfinement and chiral phase transitions.

Using rare isotope beams, the NuSTAR collaboration [4] proposes a broad research spectrum from nuclear structure physics to nuclear astrophysics through fundamental interactions and symmetries.

The APPA collaborations [5] take advantage of heavy ion beams to focus on matter under extreme conditions of temperature and pressure, on optical properties of matter under these conditions, on the effects of irradiations on large area samples, also on atomic spectroscopy and collisions. Moreover with low energy antiprotons, spectroscopy of antiprotonic atoms and antihydrogen will be possible.

2.1.2 The FAIR facility

The concept of the Facility for Antiproton and Ion Research (FAIR, see layout Fig. 2.1) to be built at Darmstadt (Germany) has been developed in cooperation of an international community of 45 countries and about 2500 scientists and engineers. Once upgraded for high intensities, the existing GSI accelerators UNILAC (UNIversal Linear ACcelerator) and SIS18 (synchrotron with a maximum magnetic rigidity of 18 Tm) as well as a proton LINAC (to be built) will serve as pre-accelerator and injector for the new complex. Its heart is a double-ring accelerator namely SIS100/300 (heavy ion synchrotron) with a 1100 meter circumference and with magnetic rigidities of 100 and 300 Tm respectively. Coupled with a cooler system and storage rings, the synchrotrons will deliver high intensity and high energy beams from protons to heavy ions.

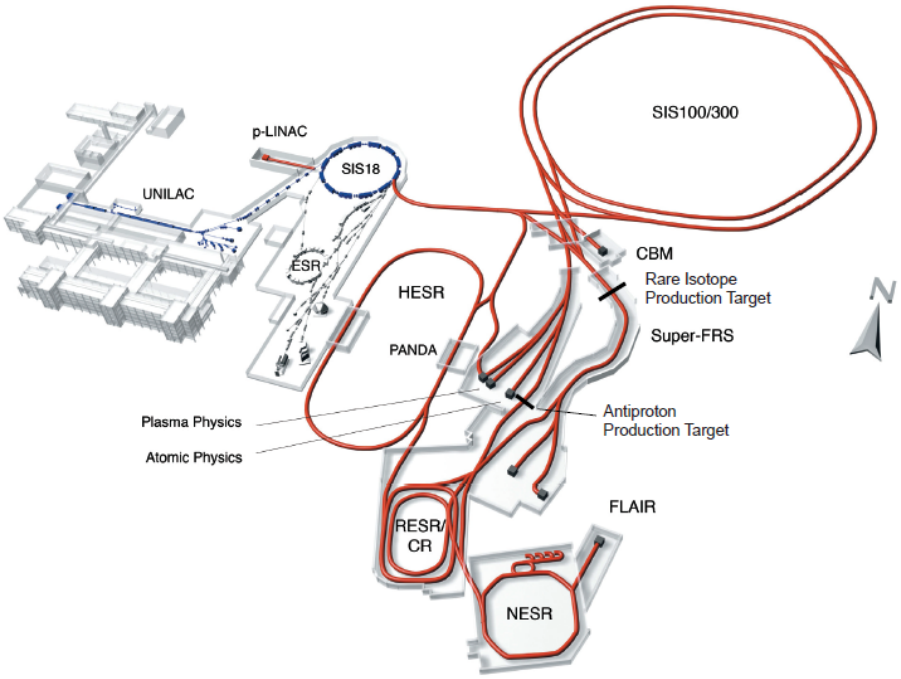

Figure 2.1: Facility for Antiproton and Ion Reseach (FAIR, from [1]). Blue color stands for the existing GSI facility (UNILAC, SIS18, ESR). The planned FAIR facility is plotted in red color (SIS100/300 synchrotrons, the collector and accumulator rings CR and RESR respectively, the new experimental storage ring NESR, the rare isotope production target and the superconducting fragment separator Super-FRS, the proton linac, the antiproton production target and the high energy storage ring HESR). Experimental stations are also displayed for antiproton physics ($\overline{\text{P}}$ANDA), plasma physics, atomic physics, relativistic nuclear collisions (CBM), radioactive ion beams (after Super-FRS) and low energy antiproton and ion physics (FLAIR).

Antiproton will be produced on a metal target [6] bombarded with 30 GeV/c proton beams from SIS100. Antiprotons are collected and transfered in a Collector Ring (CR) to be accumulated and cooled down to 3.8 GeV/c before being injected either in the High Energy Storage Ring (HESR) or in the New Experimental Storage Ring (NESR). The HESR will be used for high energy antiproton physics experiment like $\overline{\text{P}}$ANDA . The HESR will be equiped with both stochastic and electron cooling to provide high

luminosity and high resolution beams. It consists of two 180° arcs and two straight sections. One straight section will be occupied by the $\overline{\text{P}}$ANDA detector investigating antiproton annihilation reactions from an internal hydrogen target [7] and the other one by the electron cooling. Table 2.1 presents the specifications and the operating modes of the HESR. The NESR will also be equiped with stochastic and electron cooling. It serves to cool and decelerate stable and radioactive ions as well as antiprotons for low energy experiments and trap experiment at FLAIR (Facility for Low Antiproton and Ion physics).

Primary ion beams can be accelerated in the SIS100 and produce radioactive secondary beams selected via the Super-FRS (Superconducting FRagment Separator). Using SIS100/300, high energy heavy ion beams are produced from nuclear collision experiments, plasma and atomic physics.

HESR specifications	
Ion species	Antiprotons
$\overline{\text{p}}$ production rate	2 10^7 s^{-1} (1.2 10^{10} per 10 min)
Momentum range	1.5 to 15 GeV/c
HESR operation modes	
High resolution	Luminosity of 2 $10^{31}cm^{-2}s^{-1}$ for 10^{10} $\overline{\text{p}}$
	momentum spread $\sigma_p/p \leq 2\ 10^{-5}$
	1.5 to 9 GeV/c, electron cooling up to 9 GeV/c
High luminosity	Luminosity of 2 $10^{32}cm^{-2}s^{-1}$ for 10^{11} $\overline{\text{p}}$
	momentum spread $\sigma_p/p \sim 10^{-4}$
	1.5 to 15 GeV/c, stochastic cooling above 3.8 GeV/c

Table 2.1: HESR specifications and operation modes

2.2 $\overline{\text{P}}$ANDA

The strong force governs the microscopic structure of the matter. It bounds the nucleons within the atomic nucleus. It also determines the interaction between the quarks within the nucleon and other hadrons. The modern theory of the strong interactions is the Quantum ChromoDynamics (QCD). Together with the electroweak theory, QCD is part of the Standard Model of particle physics.

The building blocks of the QCD are the quarks and the vectors of the interaction are the gluons. QCD is well understood at short distances (i.e.: shorter than the nucleon size) where the strong coupling constants small and perturbation theory can be applied. The perturbative approach fails when the distance becomes comparable to the nucleon size. In that case the force between quarks becomes so strong that they cannot be separated anymore. As a consequence, quarks have never been observed as free particles and are confined within hadrons made of three quarks or a pair quark-antiquark.

A few micro seconds after the big bang, the quark sea evolved to hadron with masses. The elementary quarks up and down have very small masses and represent only few percents of the nucleon mass. The main part of the nucleon mass arises from the quark confinement and the spontaneous breaking of chiral symmetry.

The confinement of quarks, the origin of mass, the existence of hybrids and glueballs are long standing open fields. A major part of the $\overline{\text{P}}$ANDA physics program is designed to address these questions.

2.2.1 $\overline{\text{P}}$ANDA physics program

High energy and intensity antiproton beams provided by FAIR together with $\overline{\text{P}}$ANDA are an excellent tool to explore hadronic physics and strong interaction, see [7]. With a momentum range from 1.5 GeV/c to 15 GeV/c, the antiproton beam will allow the production of heavy strange and charmed hadrons as well as hybrids (combinations of quarks and gluons) and glueballs (consisting only of gluons). Fig. 2.2 shows a spectrum of accessible states of matter (light and heavy hadrons, gluonic excitations, ...).

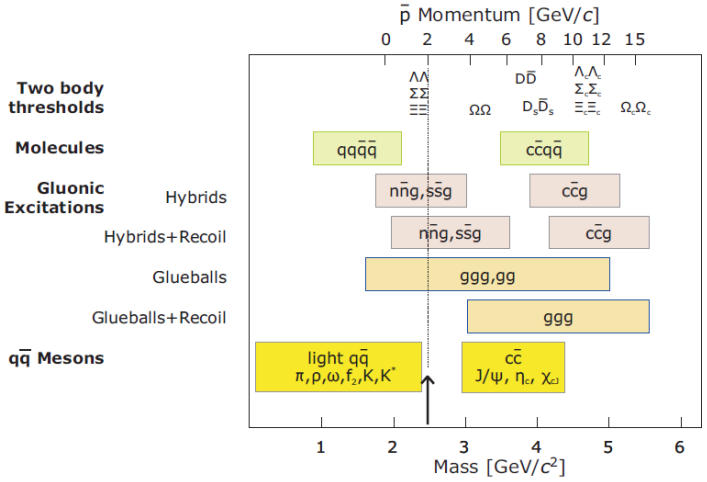

Figure 2.2: Accessible hadrons with the antiproton beam at FAIR, from [1]. The upper scale displays the antiproton momentum and the lower one the hadron mass. The vertical line shows the maximum mass that can be produced in $\bar{p}p$ annihilations at the former Low Energy Antiproton Ring (LEAR) at CERN.

- Non relativistic potential models, effective field theories and lattice QCD can predict particle spectra. To determine the good approach and have a better understanding of QCD precise measurements are needed. $\overline{\text{P}}$ANDA will not only allow standard meson and baryon spectroscopy (built of up, down, strange, charmed quarks and antiquarks) but also more complicated configurations such as exotic states (hybrids and glueballs).

- The hyperon pair production involves the creation of a quark-antiquark pair or the knock out of such pairs out of the nucleon sea. The measurement of the reaction antiproton proton to antihyperon hyperon (e.g.: $\overline{p}p \rightarrow \Lambda_c\overline{\Lambda}_c$) will enable to study the mechanism of these quark antiquark pair creation.

- The study of hadronic matter will help to understand the origin of hadron masses in the context of spontaneous chiral symmetry breaking and its partial restoration in hadronic matter. Up to now, that was studied in the light quark sector. The high energy antiproton beam will extend this sector to heavier hadron masses.

- Hypernuclei are systems in which up and/or down quarks are replaced by strange quarks. Efficient production of hypernuclei will open new perspectives for nuclear structure spectroscopy and allow to study the interactions between hyperons and nucleons.

- By producing D-mesons, rare weak decays can be observed allowing to study electroweak physics by probing predictions of the standard model.

- The nucleon structure can also be investigated using electromagnetic processes. $\overline{p}p \rightarrow e^+e^-$ [8] will allow the determination of the electromagnetic form factors of the proton in the Time-Like region (see Chapter 3). The process $\overline{p}p \rightarrow \pi^\circ e^+e^-$ may provide access to the electromagnetic proton form factors in the unphysical region. The measurement of the electromagnetic proton form factors with the reaction $\overline{p}p \rightarrow \pi^\circ e^+e^-$ is addressed in the present document.

2.2.2 $\overline{\text{P}}$ANDA detector

The $\overline{\text{P}}$ANDA detector (Fig. 2.3) is a fixed target detector based on two spectrometers [9] to fulfil the requirements imposed by the physics cases: 4Π acceptance, high resolution tracking, electromagnetic calorimetry and particle identification for e, μ, π, K, p and their antiparticles as well as photons. High rate capabilities and on-line trigger are also key features.

The target spectrometer based on a superconducting solenoid magnet surrounding the target will measure the particles with polar θ angle above 5° (10°) in the vertical (horizontal) plane whereas the forward spectrometer based on a dipole magnet will be used for the particles emitted at small polar θ angles i.e.: θ below 5° (10°) in the vertical (horizontal) plane. For both spectrometers, tracking, electromagnetic calorimetry, particle identification as well as muon identification are available.

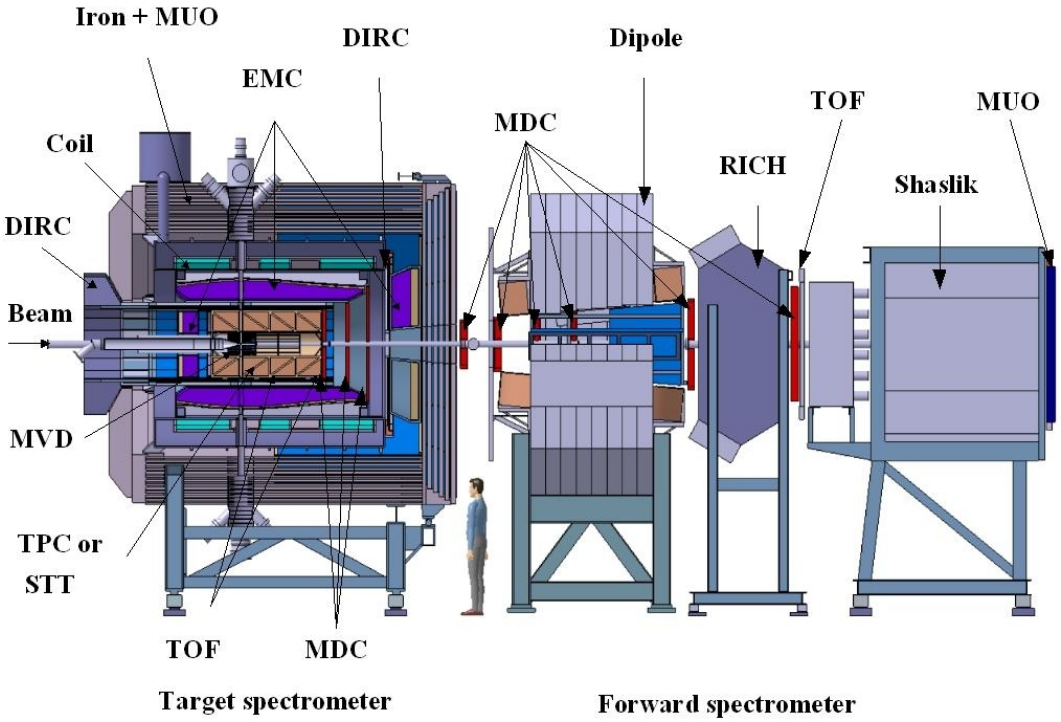

Figure 2.3: Side view of the $\overline{\text{P}}$ANDA detector with both target and forward spectrometers, adapted from [2]. The target spectrometer comprises a MicroVertex Dectector (MVD), a central tracker (Time Projection Chamber (TPC) or STraw Tubes (STT)), a Cherenkov (DIRC) and a Time Of Flight (TOF) detectors, an ElectroMagnetic Calorimeter (EMC), Gas Electron Multiplier chambers (GEM) and a MUOn (MUO) detector. The forward spectrometer is based on STT chambers, Cherenkov (RICH), TOF, Shaslik calorimeter and MUO detectors.

2.2.2.1 Target spectrometer

The target spectrometer surrounds the interaction point with a 2T solenoidal field. One of the key points of the design is the compactness: all sub-detectors must fit inside the superconducting solenoid magnet.

The electromagnetic calorimeter (EMC, Fig. 2.4) is used to measure γ and $e^{\pm}$ energy via the electromagnetic shower phenomena. In association with the tracking system, the electromagnetic calorimeter will help for particle identification of charged particles. Furthermore, the EMC providing precise photon and electron energy measurements (from few MeV up to 10 GeV), will open a broad range of studies from the electromagnetic form factors to excited states of charmonium studies [10].

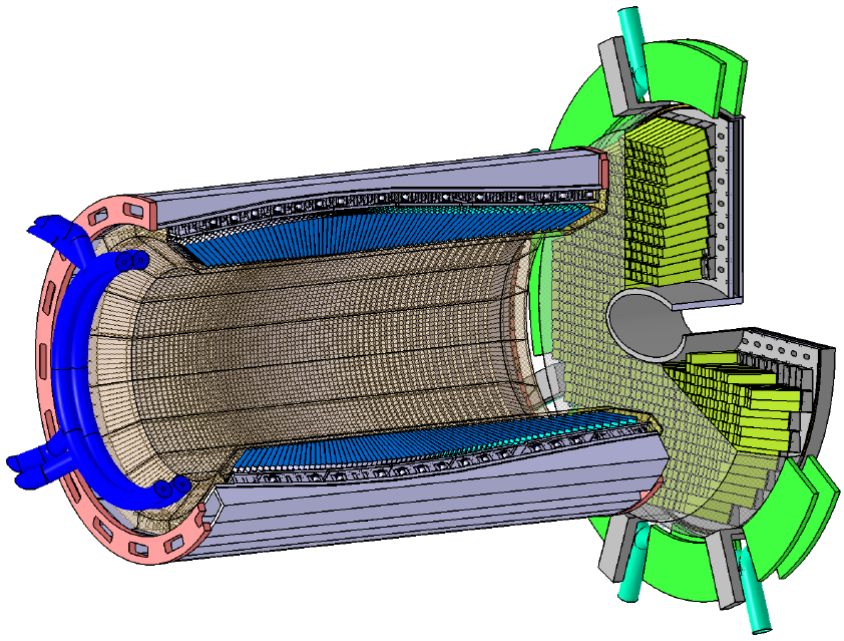

Figure 2.4: The barrel and forward end cap EMC, from [10]

The EMC consists of one central barrel and two end caps (backward and forward). Fig. 2.4 displays the barrel and the forward endcap. The central barrel is composed of 11360 crystals for a weight of 11 186 kg, a 2.50 meter length and an entrance radius of 0.57 meter. It is divided into 16 identical sectors. To avoid photons going between two crystals, their axes are tilted by 4° which corresponds to a 4 cm shift of the focus point. Taking into account the barrel dimensions and crystal orientations, the barrel covers from 22° up to 140°. 6864 crystals form the forward end cap and 816 crystals compose the backward end cap. Both end caps are divided in 4 sectors. In a similar way to the central barrel, crystals are not pointing directly to the interaction point. Furthermore, the forward (backward) end cap covers the angles from 5° - 10° up to 22° (from 147.5° up to ∼165°).

$\overline{\text{P}}$ANDA will use lead tungstate crystals ($PbWO_4$) commonly named PWO crystals (see Fig. 2.5) produced by the Bogoroditsk Techno Chemical Plant (BTCP) in Russia. PWO crystals were used in the Compact Muon Solenoid (CMS, [11]) experiment at CERN. $\overline{\text{P}}$ANDA takes advantage of ten years of expertise in PWO crystal production (improvement of the crystal quality and light yield). PWO has been chosen due to its attractive characteristics (see Table 2.2). Its high density allows to have a relatively compact detector and its fast decay time of 6 ns (dominant at 97%) to afford the high counting rate especially at forward angle (10^7 annihilations per second are expected at $\overline{\text{P}}$ANDA).

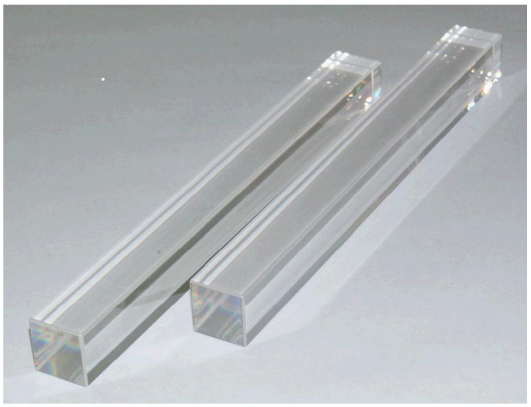

Figure 2.5: Two $PbWO_4$ crystals, from [9]

$PbWO_4$ crystals have important drawbacks like the temperature dependence of the light yield, the low light yield (approximatively 0.6% of NaI for the fast decay) and finally its sensitivity to radiation. To increase the light yield of PWO crystals, they are cooled down to -25°C with a 0.1°C stability (One goes from 20 phe/MeV at 25°C to 95 phe/MeV at -25°C).

PWO light is produced by WO_4^{2-}, WO_4^{3-} (center of higher luminosity in PWO crystals) and WO_3. $\overline{\text{P}}$ANDA will use PWO 2^{nd} generation (PWOII) which is PWO doped with few ppm[1] of Lanthanum or Yttrium. PWOII crystals have a light yield increase (due to the different doping and temperature) by 80% compared to PWO crystals used by CMS. In comparison to NaI which has a light yield of 40 γ/keV of energy deposit, PWO light yield is 240 γ/MeV of energy deposit for the fast decay and 38 γ/MeV of energy deposit for the slow decay. Such values are very low.

An important activity on the radiation sensitivity at -25°C has been conducted by several groups in the collaboration [12]. Although the final answer is not clear yet, the gain obtained on the light yield largely compensates the loss due to radiation.

Parameter	$PbWO_4$
Density(ρ)	8,28 g.cm^{-3}
Radiation length (X_0)	0,89 cm
Energy loss (dE/dx) at MIP	10.2 MeV.cm^{-1}
Decay time (τ_{decay})	6 ns
Light yield (LY)	0,6 (fast)% of NaI
	0,1 (slow)% of NaI
d(ln(LY))/dT	-3%.°C^{-1}

Table 2.2: Relevant PWOII properties.

[1] ppm: parts per million

One has to note that, with the important magnetic field, photomultipliers can not be used. Avalanche PhotoDiodes (APD) being not sensitive to magnetic fields, were then chosen for the photon detection. They also exhibit a gain depending on temperature. In such conditions, it is necessary to stabilize both APDs and crystals to 0.1°C which corresponds to light yield variations of 0.3%.

An avalanche photodiode is a PIN diode (PN diode with an inverse polarization) in which a current amplification is obtained in the depleted zone. This method allows the extraction of a good electric signal even if the light signal is very low. In fact, when a gamma is absorbed in the depleted area, if its energy is above the energy gap, an electron-hole pair is created. This electron is then accelerated by the electric field. Furthermore, it can give to another electron of the valence band the sufficient energy to go to the conduction band. So, there are two free electrons in the conduction band. That is called ionization by collisions.

On one hand, APD have advantages such as insensitivity to magnetic fields and low energy consumption but on the other hand, they exhibit drawbacks: small sizes (only a small fraction of the photons are directly detected, the present Hamamatsu S8664-1010 APD is 10x10 mm^2 and covers 14% of the rear crystal surface), small gain (signals must be further amplified) and temperature sensitivity (gain increases when temperature decreases, [13]). Studies are ongoing to use two rectangular APDs instead of one to cover the major part of the rear crystal face.

The electromagnetic calorimetry is a method of energy measurement based on electromagnetic showers using high density materials with high Z values. An electromagnetic shower is produced when a particle enters any material if its energy is higher than the critical energy. The critical energy is defined as [14]:

$$E_c^e \approx 800/(Z + 1.2) \text{ GeV} \tag{2.1}$$

i.e.: approximatively 9 MeV in case of $PbWO_4$. For high energy, the Bremsstrahlung effect for electrons and positrons as well as the pair creation for gammas i.e. : $e \rightarrow e'\gamma$ and $\gamma \rightarrow e^+e^-$ are contributing. If the particle energy is below the critical energy, Bremsstrahlung and pair creation are no longer dominating, but only ionization, Compton effect and photoelectric effect have the leading role.

Knowing the radiation length X_0, the shower depth can be calculated. The following formula gives the depth X in which 95% of the shower is contained, [15]:

$$\frac{X}{X_0} \approx \frac{1}{ln(2)} ln(\frac{E_0}{E_c}) + 0.008Z + 9.6. \tag{2.2}$$

For a 15 GeV electron, $\frac{X}{X_0}$ =21 has to be compared to the length of $\overline{\text{P}}$ANDA calorimeter crystals of 22 (where X_0 is equal to 0.89 cm for $PbWO_4$).

The relative resolution $\frac{\sigma(E)}{E}$ of a calorimeter is usually parametrised as:

$$\frac{\sigma}{E} = \frac{a}{\sqrt{E}} \oplus \frac{b}{E} \oplus c, \tag{2.3}$$

where $\frac{a}{\sqrt{E}}$ stands for the sampling, $\frac{b}{E}$ for the background (electronic noise, pile up, ...) and c for the constant term (bad calibration, inhomogeneity, ...). So, higher is the energy of the incident particle, better is the resolution. The design goal for $\overline{\text{P}}$ANDA resolution is: $\sigma/E \approx 1/\sqrt{E} \oplus 1$. Tests done at the Mainz photon tagger facility at -25°C are detailed in Chapter 7.

The magnet is used to bend charged particle trajectories [16]. Once combined with the microvertex detector and the central tracker, it will allow to determine the charged particle momenta. It is a superconducting solenoid coil with an inner radius of 90 cm producing a 2 Tesla field. A field inhomogeneity below 2% over the volume of the microvertex and the central tracker is expected to achieve the precision needed by the physics cases. Furthermore, the transverse field should be as small as possible in order to allow uniform drift of charges.

A target thickness of 4 10^{15} hydrogen atoms per cm^2 is required to reach the design luminosity of 2 10^{32}cm^{-2}s^{-1}.

The pellet target is based on a stream of frozen hydrogen micro-spheres called pellets. With this technique, the design luminosity is reached with a 4 10^{15} atoms per cm^{-2} (average) target density. The use of other gases like deuterium, N_2 or Argon is possible.

The cluster-jet target is another possible design and it is based on the expansion of pressurized cold hydrogen gas into vacuum through a Laval-type nozzle. The advantage of such a target is the homogeneous density profile but at the moment only 8 10^{14} hydrogen atoms per cm^2 target can be done (which is below the requirements).

The pipe for the target material injection will be perpendicular to the beam pipe. The request to have the MicroVertex Detector at the minimal distance from the interaction point combined with the compact detector design leaves very little space for the target installation.

The Micro-Vertex Detector (MVD) is used to reconstruct charged particle trajectories and aims to detect secondary vertices from D and hyperons decays ($c\tau < 150$ μm). Combined with central and forward trackers, it will also improve the momentum resolution. The MVD is based on radiation hard silicon pixel and silicon strip detectors. The design includes 4-layer barrel from 4.4 cm to 10.5 cm and six detector wheels arranged perpendicularly to the beam to have the best acceptance for forward angles.

The central tracker is designed to reconstruct charged particle trajectories, to detect secondary vertices ($c\tau$ = 2.69 cm for K^0_S, $c\tau$ = 7.89 cm for Λ) out of the MVD and to measure energy losses. With a 2 $10^{32}cm^{-2}s^{-1}$ luminosity, the central tracker must also deal with high fluxes of particles and also provide a momentum resolution $\delta p/p < 2\%$ at 1 GeV/c. Two possibilities have been considered in details up to recently: one based on Straw Tubes (STT) or a Time-Projection Chamber (TPC) which need to fit in a 150 cm long barrel with an inner radius of 15 cm and an outer radius of 42 cm.

Straw Tubes are aluminized mylar tubes filled with an Argon CO_2 mixture at 1 bar overpressure. The tubes are 150 cm long for a 10 mm diameter with a mylar foil thickness of 30 μm and 20 μm diameter gold plated tungsten wires. The 4200 straw tubes will be arranged in 24 planar layers and mounted in an hexagonal shape around the micro-vertex detector. Eight layers are tilted to measure the z coordinate. The expected resolutions are 150 μm and 3 mm in the xy and z coordinates respectively. The energy loss measurements can be obtained via flash ADCs.

Time Projection Chamber could be a good option providing identification capabilities through energy loss measurements. The TPC consists of two large gas-filled half-cylinders surrounding the beam pipes, the target and the MVD. Within an electric field along the cylinder axis, positive ions are separated from electrons which are then detected by a pad readout plane. The information from the readout plane and the measurement of the drift time leads to the three coordinates of the track. To avoid a continous backflow of ions in the drift volume which could distort the electric field, the amplification stage is based on Gas Electron Multiplier (GEM) foils. Due to the slow drift (2.7 cm per μs for electrons) and the high rate, the challenge for the TPC will be the accumulation of charge (around 3000 tracks at any given time) and the fast on-line reconstruction of the tracks.

In september 2011, the collaboration voted for the straw tubes as central tracker.

Gas electron multiplier (GEM) detectors cover the forward angles below 22°. The advantage of these detectors is to stand the high particle rate (3 $10^4cm^{-2}s^{-1}$). Since drift chambers do not fulfil this rate requirements, gaseous micropattern detectors based on GEM foils will be used.

Cherenkov detectors combined with the central tracker can help to identify particles with momenta from 0.8 GeV/c up to about 5 GeV/c. For slower particles, Time of flight detectors should be efficient. The particle identification is really important to remove background from a channel of interest. Crossing a radiator with a refraction index n, a charged particle with a velocity $\beta > \beta_{threshold}$ (with $\beta_{threshold}$=1/n) emits radiations with a θ angle following the formula $cos\theta = 1/(\beta\ \text{n})$. Knowing the particle momenta (from the central tracker) and measuring the θ angle, the particle can be identified. The Fig. 2.6 shows for n=1.47, the Cherenkov angle as a function of momentum for electron (black), muon (red), pion (green), kaon (blue) and proton (light blue).

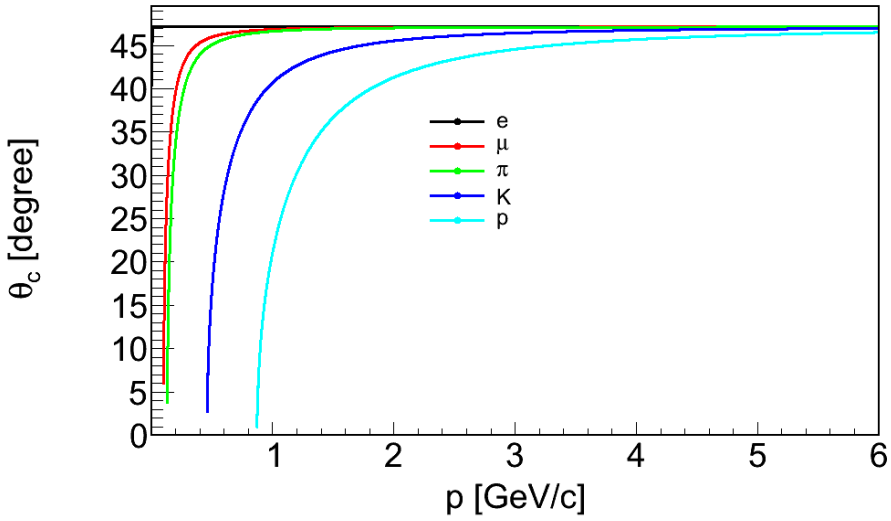

Figure 2.6: Cherenkov angle depending on momentum for electron (black), muon (red), pion (green), kaon (blue) and proton (light blue) taking into account a refractive index n of 1.47.

The Cherenkov detector is composed by one barrel for angles above 22° and a forward end cap for angles from 5° to 22°. The barrel DIRC (Dectection of Internally Reflected Cherenkov light) covers angles from 22° to 140° and surrounds the beam line at a radial distance from 45 to 54 cm i.e. just in front of the EMC crystals. Fused silica (i.e.: artificial quartz) with a refractive index of 1.47 was chosen as radiator material. The advantage is the thickness of the quartz slabs, here only 1.7 cm which limits the creation of pre-shower since the DIRC is located in front of the EMC. The imaging will be achieved by lenses focusing on micro-channel plate photomultiplier tubes (MCP PMTs) which are insensitive to magnetic fields. In addition, the MCP PMTs provide good time resolution. For the forward end cap DIRC, the same concept is used: the radiator material consists of fused silica and MCP PMTs for the imaging. The forward end cap is a 2 cm thick disk which fits within a 110 cm radius.

Time of Flight information combined with the momentum measured in the tracker is helpful for the identification of slow particles at polar angles from 22° to 140°. It will be located between the central tracker and the DIRC. Therefore the time of flight must fit within a radial interval of 3 cm. It is also designed to minimize its effects on the electromagnetic calorimeter resolution.

The time of flight t is defined as $t = l/(\beta c)$ where l is the path length and β is the charged particle velocity. Within a 2 T magnetic field and knowing that the minimal path length is 0.42 m, the minimum particle momenta to be detected is $|\overrightarrow{p_\perp}| = 0.3B\rho = 0.125$ GeV, where B is the magnetic field in Tesla and ρ stands for the radius curvature in meter (here the minimal value of the curvature radius is 0.21 m). Since the pions and the muons are the two particles with the closest masses, it is clear that the separation of pions from muons will be the most difficult. To better quantify the required precision of the time of flight, one needs to look at the time difference between two particles. The Fig. 2.7 presents the time difference for the same path length. Black markers stand for

$|t_\pi\text{-}t_e|$, red ones for $|t_\pi\text{-}t_\mu|$, green ones for $|t_\pi\text{-}t_K|$ and blue ones for $|t_\pi\text{-}t_p|$. It shows that the resolution must be of the order of the 10-20 ps to distinguish muons from pions but also electron from pion at 1 GeV/c which is out of reach. The yellow line represents the typical time of flight resolution of 100 ps. Therefore the time of flight will help for electron/pion identification only below 0.4 GeV/c.

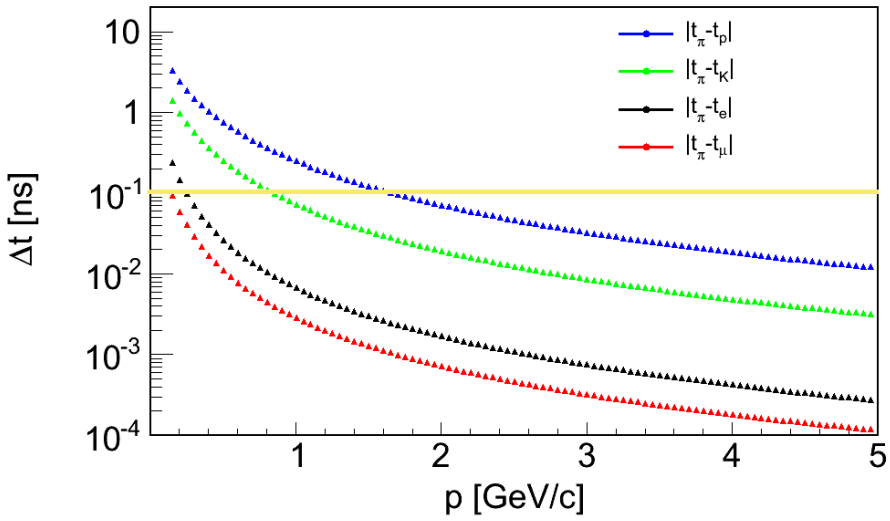

Figure 2.7: Time of flight difference depending on momentum assuming a 0.42 m path length for $|t_\pi\text{-}t_e|$ (black), $|t_\pi\text{-}t_\mu|$ (red), $|t_\pi\text{-}t_K|$ (green) and $|t_\pi\text{-}t_p|$ (blue). Yellow line represents the typical time of flight resolution of 100 ps.

Muon detector The goal of the muon detector is to separate primary muons from secondary muons coming from pion decays. A segmentation of the yoke of the solenoid magnet which acts as absorber with interleaved tracking detectors to measure energy losses and decays. The barrel part is segmented in a first layer of 6 cm iron followed by 12 layers of 3 cm thickness with 3 cm gap for tracking detectors. The end cap is divided into 5 layers of 6 cm iron plus a removable muon filter of 5 additional layers of 6 cm iron. Aluminium drift tubes with read out on both ends (to obtain longitudinal coordinate) are used as detectors.

2.2.2.2 Forward spectrometer

The Forward Spectrometer, covering the angular acceptance of $\pm 10°$ ($\pm 5°$) in the horizontal (vertical) direction, is designed to study the forward tracks. It is built around a dipole magnet.

Similarly to the target spectrometer, the dipole magnet [16] will bend the charged particle trajectories. The bending power of the dipole magnet will be 2 T.m corresponding to a deflection of 2.2° for 15 GeV/c antiprotons.

The tracking will be handled by 6 straw tube chambers. Two will be located in front, two within and two behind the dipole magnet to detect both high and low momentum

particles. Each chamber will contain 4 double-layers, the second and the third layer being respectively tilted by 5° and -5° to fully reconstruct tracks in both x and y direction in each chamber separately and to handle multi-track events.

Both RICH (for high momentum particles) and Time of Flight (for low momentum particles) detectors will contribute to the particle identification (with the tracking information) of pions, kaons and protons. The RICH detector will be composed of two radiators: one made of silica aerogel (n=1.0304) and one made of C_4F_{10} gas (n=1.00137) and provide π, K and p separation from 2 to 15 GeV/c. Fig. 2.8 presents for both radiators the Cherenkov angle as a function of momentum for electron (black), muon (red), pion (green), kaon (blue) and proton (light blue). In the second radiator, in the available kinematical range, the proton velocity is always below the threshold and therefore protons will not radiate. The resolution is assumed to be $\sigma_\theta = 4$ mrad $= 0.2$ degree. The Time of Flight detector will be based on plastic scintillators coupled to fast phototubes on both ends for the read out.

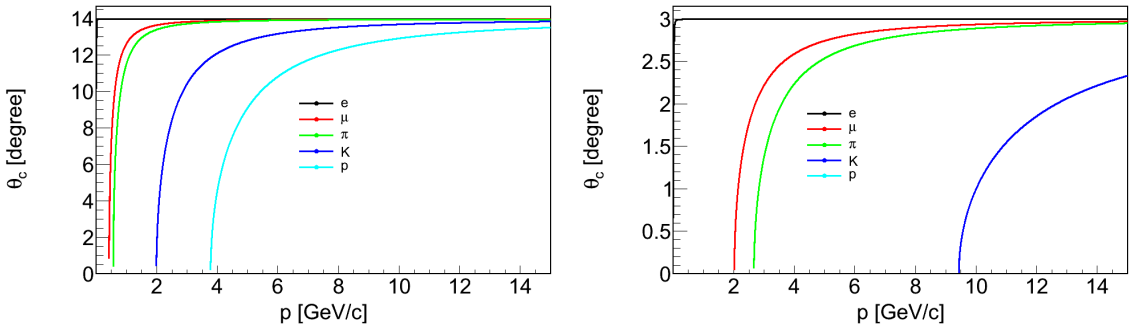

(a) Silica aerogel radiator (b) C_4F_{10} radiator

Figure 2.8: Cherenkov angle depending on momentum for electron (black), muon (red), pion (green), kaon (blue) and proton (light blue) taking into account a refractive index n of 1.0304 (2.8(a)) and n=1.00137 (2.8(b)).

The detection and identification of high momentum photons and electrons will be managed by a high resolution and efficient Shashlyk-type calorimeter based on lead scintillator sandwiches. The read out will be done via wavelength shifting fibers coupled to photomultipliers.

Muon detectors will discriminate pions from muons and detect the pion decays. It will be similar to the muon detector of the target spectrometer but will be suited for higher momenta.

2.2.2.3 Data acquisition and trigger

In $\overline{\text{P}}$ANDA, every sub-detector system is a self-triggering entity. All detectors will preprocess signals in order to extract and transmit only the physically relevant information. This requires hit detection, noise suppression and clustering at the read out level. The data related to a particle hit, with a substantially reduced rate in the preprocessing step, is marked by a precise time stamp and buffered for further processing. The final trigger

selection will be done in computing nodes which access the buffers via a high bandwidth network fabric.

To have such a flexible data acquisition and trigger, the hardware infrastructure will be based on intelligent front-end electronics capable of autonomous hit detection and data preprocessing, on a precise time distribution system to correlate all detector information, on data concentrators providing point to point communication via optic links and on compute nodes.

A major component providing the link for the hardware is the network fabric. The network fabric is a network where each node is connected to all others via one or several switches.

Chapter 3

Nucleon electromagnetic form factors

3.1 Introduction

The nucleon is an object composed of interacting quarks and gluons. Its cohesion is due to the strong interaction described by the quantum chromodynamics (QCD). However, a clean understanding of the nucleon structure is far from being reached.

In this respect, the electromagnetic probe is an excellent tool. The nucleon electromagnetic form factors are key observables to characterize the nucleon internal structure.

Tab. 3.1 shows the notations used in the following chapters.

Notation	Definition
p_i	4-momentum of the particle i (GeV/c)
E_i	total energy of the particle i (GeV)
T_i	kinetic energy of the particle i (GeV)
$\overrightarrow{p}_i$	3-momentum of the particle i (GeV/c)
$\lvert\overrightarrow{p}_i\rvert$	3-momentum modulus of the particle i (GeV/c)
M_i	mass of the particle i (GeV/c^2)
Ω_i	solid angle of the particle i (sr)
m_i	spin projection of the particle i
$\mathcal{L}$, $\mathcal{H}$	matrices

Table 3.1: General notations

In this thesis, the variable q^2 is taken to be homogeneous to a mass squared and is consequently expressed in terms of (GeV/c^2)^2. In the litterature, other conventions can be found.

3.2 Kinematical Region

The proton form factors can be accessed via the elastic scattering reaction $ep \to e'p'$ (Fig. 3.1(a)) in Space-Like (SL) region or via the annihilation reactions $e^+e^- \to \overline{p}p$ (Fig. 3.1(b)) and $\overline{p}p \to e^+e^-$ (Fig. 3.1(c)) in Time-Like (TL) region, in the one photon exchange approximation.

For these three reactions, only initial and final states as well as kinematics are different whereas $e^+e^-\gamma$ and γNN vertices and also the photon propagator are the same. The four-momentum transfer squared (q^2) is defined as the invariant mass squared of the virtual photon (i.e.: $q^2 = M^2_{\gamma*}$) which is the vector of the electromagnetic interaction.

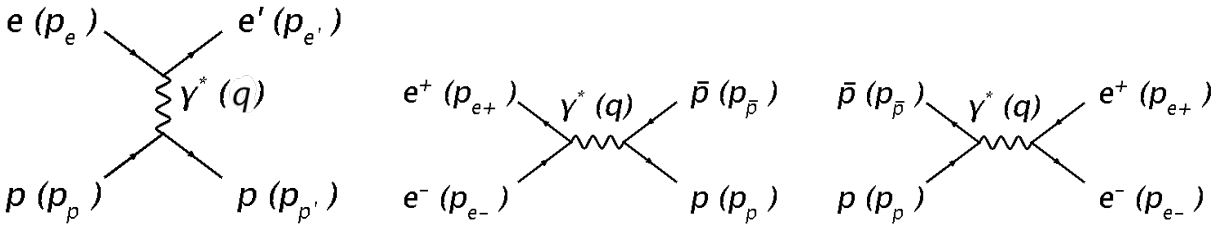

(a) $ep \to e'p'$ (b) $e^+e^- \to \overline{p}p$ (c) $\overline{p}p \to e^+e^-$

Figure 3.1: Possible reactions for the form factor studies: (a) ep scattering reaction in Space-Like, (b) $e^+e^- \to \overline{p}p$ annihilation reaction in Time-Like and (c) its time reversed reaction $\overline{p}p \to e^+e^-$ in Time-Like.

In the Space-Like (SL) region, the form factors are real while in the Time-Like (TL) region they have a non-zero imaginary part due to the presence of annihilation channels $e^+e^- \to \gamma^* \to \pi^+\pi^-/\rho/\omega/\phi/\ldots$ However, below the 2π threshold $q^2 = 4m^2_\pi$, the Time-Like form factors are real.

3.2.1 Space-Like region

In the case of electron-proton scattering, by writing the q^2 expression starting from the initial and recoil proton momenta in the lab frame one can see that q^2 is negative.

$$q^2 = (p_p - p_{p'})^2 = -2M_pT_{p'} < 0 \tag{3.1}$$

where, in the lab frame, p_p and $p_{p'}$ are the four-momenta of the initial and recoil protons, $T_{p'}$ is the kinetic energy of the recoil proton and M_p is the proton mass. One therefore uses $Q^2{=}{-}q^2$.

Q^2 can also be expressed in terms of the incident and scattered electron energies.

$$Q^2 = 4E_eE_{e'}sin^2(\theta_{e'}/2) \tag{3.2}$$

where, in the lab frame, E_e and $E_{e'}$ are the energy of the incident and scattered electrons, $\theta_{e'}$ is the scattered electron angle and the electron mass is neglected. To access different Q^2 values, one may either change the incident energy for a given $\theta_{e'}$ or detect at different $\theta_{e'}$ angles if the incident energy cannot be changed easily.

3.2.2 Time-Like region

For both $e^+e^- \to \overline{p}p$ and $\overline{p}p \to e^+e^-$ annihilation reactions, q^2 is positive. It is fixed at a given system energy and greater than the threshold energy of $4M_p^2$.

In case of $\overline{p}p \to e^+e^-$,

$$q^2 = s = 2M_p(T_{\overline{p}} + 2M_p) > 4M_p^2 \tag{3.3}$$

where M_p is the proton mass and $T_{\overline{p}}$ is the antiproton laboratory kinetic energy. The region where $0 < q^2 < 4M_p^2$ is called the unphysical region and cannot be accessed by these reactions.

3.2.3 Time-like unphysical region

The under threshold region $0 < q^2 < 4M_p^2$ is called unphysical region because it cannot be accessed experimentally by an on shell process. A particle i with a 4-momentum that satisfies $E_i^2 - |\overrightarrow{p}_i|^2c^2 = M_i^2c^4$ is called on-shell. One way to access the unphysical region, is to use the $\overline{p}p \to \pi^\circ e^+e^-$ reaction [17] where the q^2 value may undergo below the threshold due to pion emission (Fig. 3.2(a) shows one diagram). Another way is to study $\overline{p} + A \to e^+e^-(A-1)$ reactions (more details in [18]) where the antiproton annihilates with a bound proton (see Fig. 3.2(b) shows one diagram).

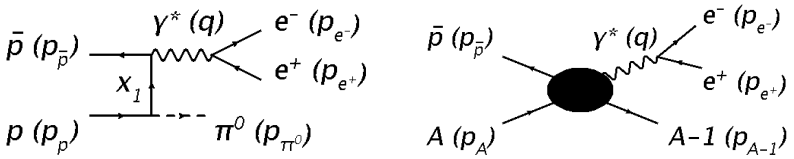

(a) $\overline{p}p \to \pi^\circ e^+e^-$ (b) $\overline{p} + A \to e^+e^-(A-1)$

Figure 3.2: Possible reactions for the form factor studies in the unphysical region. 3.2(a): the antiproton collides on a proton producing a neutral pion and a virtual photon. 3.2(b): the antiproton collides on a proton of the nucleus (A) producing a nucleus (A-1) and a virtual photon.

To summarize, Fig. 3.3 displays as a function of q^2 bothSpace-like and Time-like regions and possible reactions to access them.

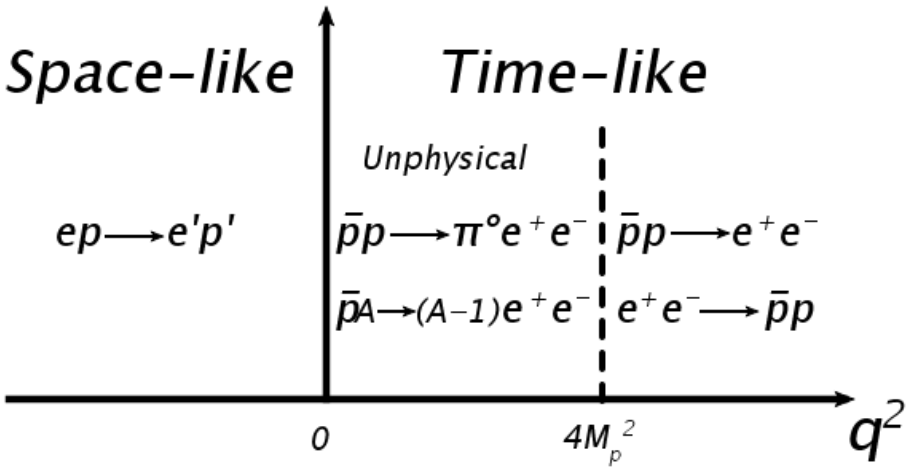

Figure 3.3: Space-like and Time-like regions and possible reactions to access them.

3.3 Proton electromagnetic form factors

In the beginning of the 20^{th} century, Stern [19] observed that the proton magnetic moment was 2.8 times higher than expected for a point-like particle. In 1950, Rosenbluth defined reduced charge and magnetic moment [20] related to the $ep \to e'p'$ cross section. In 1956, Hofstadter [21] interpreted the $ep \to e'p'$ cross section in terms of form factors.

3.3.1 The Dirac and Pauli form factors

$F_1(Q^2)$ and $F_2(Q^2)$ are respectively the Dirac and Pauli form factors. At $q^2 = 0$, $F_1(Q^2)$ and $F_2(Q^2)$ are:

$$F_1^p(0) = 1, \quad F_2^p(0) = \frac{\mu^p}{\mu^N} - 1 = \kappa^p, \quad F_1^n(0) = 0, \quad F_2^n(0) = \frac{\mu^n}{\mu^N} = \kappa^n, \tag{3.4}$$

where μ^p and μ^n are the proton and neutron magnetic moments, $\mu_N = \frac{|e|\hbar}{2M_p}$ is the nuclear magneton, κ^p and κ^n are the anomalous part of the magnetic moment for the proton and the neutron.

The experimental values of the nucleon magnetic moments are:

$$\mu^p = 2.792847351(28)\mu_N \quad \text{and} \quad \mu^n = -1.9130427(5)\mu_N \tag{3.5}$$

in rather good agreement with values deduced from the constituent quark model (in which the u and d quark masses are fixed to 333 MeV):

$$\mu^p = \left(2\mu^u + \mu^d\right) = 2.82\mu_N \quad \text{and} \quad \mu^n = \left(2\mu^d + \mu^u\right) = -1.88\mu_N, \tag{3.6}$$

where

$$\mu^u = \frac{2}{3}\frac{|e|}{2M_u}, \quad \mu^d = -\frac{1}{3}\frac{|e|}{2M_d}. \tag{3.7}$$

3.3.2 The Sachs form factors

The Sachs form factors are linear combinations of Dirac and Pauli´s form factors:

$$G_E^p(q^2) = F_1(q^2) + \frac{q^2}{4M_p^2}F_2(q^2), \tag{3.8}$$

$$G_M^p(q^2) = F_1(q^2) + F_2(q^2). \tag{3.9}$$

They are used because the $ep \to e'p'$ cross section has a simpler form when expressed in terms of Sachs form factors as shown in sec. 3.4.1.

At $q^2 = 0$, Sachs form factors are:

$$G_E^p(0) = 1, \qquad G_M^p(0) = \frac{\mu^p}{\mu^N}, \tag{3.10}$$

$$G_E^n(0) = 0, \qquad G_M^n(0) = \frac{\mu^n}{\mu^N}, \tag{3.11}$$

and at threshold ($q^2 = 4M_p^2$), $G_E^p(4M_p^2) = G_M^p(4M_p^2)$.

At low q^2 within the Breit frame (where $E_p = E_{p'}$), the Space-Like form factors $G_E(q^2)$ and $G_M(q^2)$ are equal to the Fourier transforms of the spatial charge and magnetization distributions in the nucleon. At higher q^2, this simple relation is not valid anymore and the relation between form factors and spatial charge and magnetization distributions is quite complex due to relativistic effects. Recent calculations using constituent quark proton wave functions demonstrated the relation between form factors and transverse charge and magnetic densities [22].

3.3.3 Boundary and asymptotic behaviour

At high Q^2, the form factors should follow the perturbative QCD predictions:

$$F_1(Q^2) \sim \frac{\alpha_s^2(Q^2)}{Q^4}, \; F_2(Q^2) \sim \frac{\alpha_s^2(Q^2)}{Q^6} \tag{3.12}$$

which gives in Space-Like:

$$G_E^{SL}(Q^2) \sim G_M^{SL}(Q^2) \sim \frac{\alpha_s^2(Q^2)}{Q^4} \sim \frac{1}{Q^4 ln^2(Q^2/\Lambda^2)} \tag{3.13}$$

and in Time-Like:

$$G_E^{TL}(q^2) \sim G_M^{TL}(q^2) \sim \frac{\alpha_s^2(q^2)}{q^4} \sim \frac{1}{q^4 ln^2(q^2/\Lambda^2)}, \tag{3.14}$$

where α_s is the strong coupling constant and $\Lambda = 0.3$ GeV/c^2.

In addition, as the form factors are analytical functions, the Phragmén-Lindelhöf theorem [23] implies that:

$$\lim_{q^2 \to -\infty} F_i(q^2) = \lim_{q^2 \to +\infty} F_i(q^2). \tag{3.15}$$

In Space-Like, F_1 and F_2 form factors are real. Therefore, this means that, in Time-Like, the imaginary part of F_1, F_2, G_E and G_M (related to the pair creation channel) have to vanish at large q^2.

The form factor $f(q^2)$ is an analytic function and the relation between Space-Like and Time-Like can be expressed as (dispersion relation for the imaginary part):

$$f(q^2) = \frac{1}{\pi}\left[\int_{4M_\pi^2}^{4M_p^2} \frac{Imf(s)ds}{s-q^2} + \int_{4M_p^2}^{\infty} \frac{Imf(s)ds}{s-q^2}\right], \tag{3.16}$$

with $q^2 \leq 0$.

3.4 World data

3.4.1 Space-Like

To extract form factors, the Rosenbluth and the polarization methods can be used. Both method are based on the assumption that the interaction between the electron and the proton occurs via a one-photon exchange.

The Rosenbluth technique

The Rosenbluth technique allows to obtain separated values for ${G_M^p}^2$ and ${G_E^p}^2$ knowing the cross section for $ep \to e'p'$ at a number of electron scattering angles for a fixed Q^2 by varying the beam energy.

The differential cross section in the laboratory of $ep \to e'p'$ is written as follows:

$$\left(\frac{d\sigma}{dcos\theta_{e'}}\right)^{lab} = \left(\frac{d\sigma}{dcos\theta_{e'}}\right)_{Mott} \frac{\tau}{\epsilon(1+\tau)}\left({G_M^p}^2 + \frac{\epsilon}{\tau}{G_E^p}^2\right) \tag{3.17}$$

where:

$$\left(\frac{d\sigma}{dcos\theta_{e'}}\right)_{Mott} = \left(\frac{q_e^2}{2E_e}\right)^2 \frac{cos^2\theta_{e'}/2}{sin^4\theta_{e'}/2}, \tag{3.18}$$

$$\tau = Q^2/(4M_p^2), \tag{3.19}$$

$$\epsilon^{-1} = 1 + 2(1+\tau)tan^2(\theta_{e'}/2), \tag{3.20}$$

$$\tag{3.21}$$

ϵ is the virtual photon polarization and E_e is the incident electron energy, q_e is the electron charge and $\theta_{e'}$ is the final electron angle.

Defining the reduced cross section as:

$$\left(\frac{d\sigma}{dcos\theta_{e'}}\right)_{red}^{lab} = \frac{\epsilon(1+\tau)}{\tau}\left(\frac{d\sigma}{dcos\theta_{e'}}\right)^{lab} / \left(\frac{d\sigma}{dcos\theta_{e'}}\right)_{Mott} \tag{3.22}$$

one gets the linear relation:

$$\left(\frac{d\sigma}{dcos\theta_{e'}}\right)_{red}^{lab} = {G_M^p}^2 + \frac{\epsilon}{\tau}{G_E^p}^2. \tag{3.23}$$

Many data points [24], [25] and [26] were measured for G_E^p and G_M^p up to $Q^2 = 8.83$ $(\mathrm{GeV/c^2})^2$ (see Fig. 3.4(a) and 3.4(b) from [27]). At higher Q^2, the ϵ/τ dependence of the reduced cross section leads to large uncertainties on the extraction of G_E^p, however G_M^p could be extracted up to $Q^2 = 31$ $(\mathrm{GeV/c^2})^2$ assuming $\mu_p G_E^p = G_M^p$.

Up to 8 $(\mathrm{GeV/c^2})^2$, the q^2 dependence of the magnetic form factor is close to the dipole behaviour ([28], see Fig. 3.4(b)):

$$G_M^p(Q^2) \sim \mu_p G_d(Q^2) \tag{3.24}$$

with

$$G_d(Q^2) = \left(\frac{1}{1+\frac{Q^2}{M_d^2}}\right)^2, \tag{3.25}$$

$$M_d^2 = 0.71\ (\mathrm{GeV/c^2})^2. \tag{3.26}$$

Despite the larger errors on G_E^p and the large dispersion of the data sets, a similar behaviour could be observed for G_E^p up to 6 $(\mathrm{GeV/c^2})^2$.

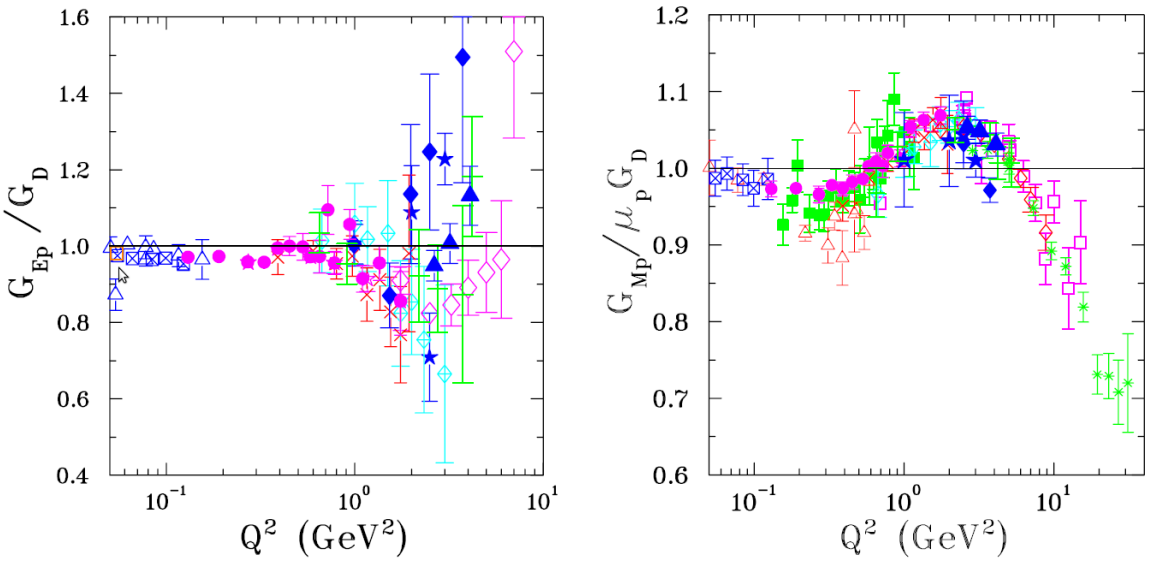

(a) G_E^p/G_d (b) $G_M^p/(\mu_p G_d)$

Figure 3.4: Data base for G_E^p/G_d and $G_M^p/(\mu_p G_d)$ obtained with the Rosenbluth technique as a function of Q^2 in Space-Like, from [27].

Polarization transfer experiments

These experiments use polarized electron beams or polarized proton targets. Measuring the longitudinal (P_l) and tranverse (P_t) polarizations of the outgoing proton, one can determine the ratio G_E^p/G_M^p as:

$$R = \frac{G_E^p}{G_M^p} = -\frac{P_t}{P_l}\frac{E_e + E_{e'}}{2M_p} tan\frac{\theta_{e'}}{2} \tag{3.27}$$

where E_e $(E_{e'})$ is the initial (final) electron energy in laboratory.

G_E^p is determined from R using G_M^p measured in previous experiments using the Rosenbluth method. The results, shown in Fig. 3.5, from [29], [30] and [31] (respectively empty green squares, circles and triangles) are not compatible with the ones from [24], [25] and [26] (red circles, triangles and squares) obtained via Rosenbluth method. Because the extraction of G_E^p with the polarization method is less sensitive to systematic errors than with the Rosenbluth method, it is believed that the polarization method gives correct determination of G_E^p. Consequently, there is a lot of activity aiming at (re)measuring the electromagnetic form factors in SL region with higher precision. There are also ongoing investigations concerning radiative corrections and possible two-photon exchange to explain the discrepancy between these different data sets [27]. However the latter is not fully understood.

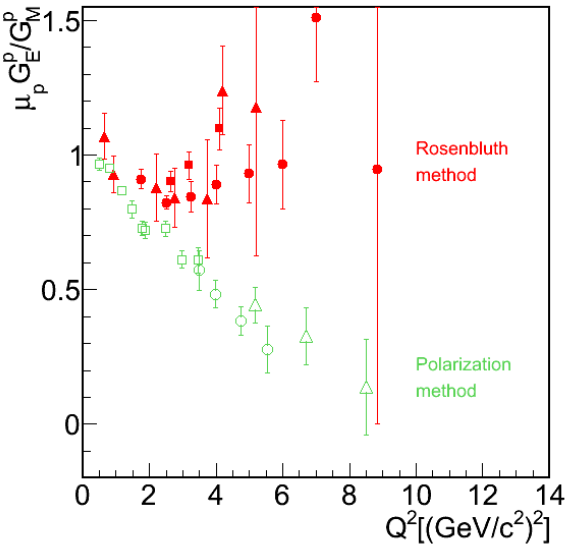

Figure 3.5: Data base for $\mu_p G_E^p/G_M^p$ as a function of Q^2. Results from [29], [30] and [31] (respectively empty green squares, circles and triangles) are obtained using the polarization method. Results from [24], [25] and [26] (red circles, triangles and squares) are obtained via the Rosenbluth method. It is clear that both methods give a different trend for the ratio $\mu_p G_E^p/G_M^p$.

3.4.2 Time-Like

Using the QED lagrangian within one-photon exchange, the differential cross section for $\bar{p}p \to e^+e^-$ in the center of mass (CM) can be expressed as (neglecting the electron mass):

$$\left(\frac{d\sigma}{dcos\theta_e^*}\right)^{CM} = \frac{\pi(\alpha_{em}\hbar c)^2}{8M_p^2\sqrt{\tau(\tau-1)}}\left[|G_M^p|^2(1+cos^2\theta_e^*) + \frac{|G_E^p|^2}{\tau}sin^2\theta_e^*\right] \tag{3.28}$$

where $\tau = \frac{q^2}{4M_p^2}$ and $\alpha_{em} = \frac{1}{137}$ is the fine-structure constant. In a similar way to the Space-Like region, the sensitivity to G_E^p will become lower as one goes to higher q^2 since the corresponding contribution scales with $1/\tau$.

After integration, one obtains:

$$\sigma = \frac{\pi(\alpha_{em}\hbar c)^2}{6M_p^2}\frac{(2\tau|G_M^p|^2 + |G_E^p|^2)}{\tau\sqrt{\tau(\tau-1)}}, \tag{3.29}$$

and using Eq. 3.28:

$$\left(\frac{d\sigma}{dcos\theta_e^*}\right)^{CM} = \frac{2\sigma}{3+A}\left(1 + Acos^2\theta_e^*\right) \tag{3.30}$$

where

$$A = \frac{\tau - R^2}{\tau + R^2}, \tag{3.31}$$

$$R = |G_E^p|/|G_M^p|. \tag{3.32}$$

The first observation is that by measuring the $cos\theta_e^*$ distribution, it is a priori possible to obtain the ratio $R = |G_E^p|/|G_M^p|$. Whereas the shape of the angular distribution allows to access the ratio R, the separate determination of $|G_M^p|$ and $|G_E^p|$ requires a precise knowledge of the normalization and of the luminosity.

If the angular distribution cannot be measured, one extracts an effective form factor from the total cross section (Eq. 3.33):

$$\sigma = \frac{\pi(\alpha_{em}\hbar c)^2}{6M_p^2}\frac{(2\tau+1)|G_{eff}|^2}{\tau\sqrt{\tau(\tau-1)}}. \tag{3.33}$$

G_{eff} is then defined by:

$$|G_{eff}|^2 = \frac{2\tau|G_M^p|^2 + |G_E^p|^2}{2\tau+1} \tag{3.34}$$

Fig. 3.6 displays $|G_{eff}^p|/G_d$ as a function of q^2 obtained in $e^+e^- \to \overline{p}p$ and $\overline{p}p \to e^+e^-$ experiments. It is worth to note that $|G_E^p|$ and $|G_M^p|$ have never been measured separately up to now.

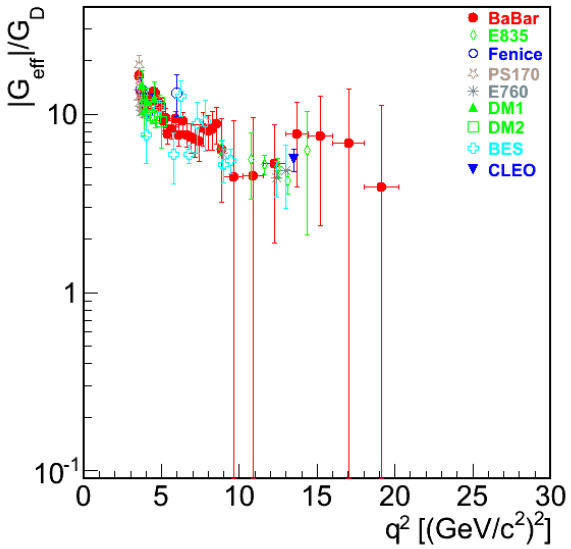

Figure 3.6: Experimental ratio $|G^p_{eff}|/G_d$ in Time-Like (adapted from [8]). Data points from $e^+e^- \to \overline{p}p$ and $\overline{p}p \to e^+e^-$ experiments.

R was measured at BABAR (electron-positron collider) and at LEAR (proton-antiproton collider) for q^2 from 3.66 up to 7.29 $(\mathrm{GeV/c^2})^2$. Both sets of data show incompatible trends (see Fig. 3.7).

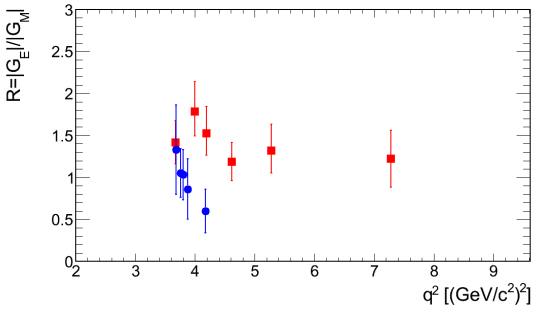

Figure 3.7: Experimental ratio $R = |G^p_E|/|G^p_M|$ as a function of q^2. Red squares display BABAR data [32] and blue circles show the LEAR ones [33].

To conclude, more precise data are needed in Time-Like region especially at high q^2. This will be the main goal of the $\overline{p}p \to e^+e^-$ measurements at $\overline{\mathrm{P}}$ANDA . On the other hand the measurement of $\overline{p}p \to \pi^\circ e^+e^-$ at $\overline{\mathrm{P}}$ANDA which is the subject of this work may allow to access the form factors in the unphysical region for the first time.

3.5 Form factor parametrizations

To interpret these data, different models are used [27]. Most of them are developed in the space like region. We use in the following two models which are able to fit both space like and time like data.

3.5.1 Vector Meson Dominance (VMD) model

A serie of models is inspired by the vector meson dominance which assumes that the electromagnetic interaction is mediated by a vector meson [34]. A vector meson is a meson with total spin 1 and odd parity ($J^P = 1^-$) i.e. the same quantum numbers as the photon. The dominance of vector mesons such as ρ, ω and ϕ in the Time-Like region should then play a major role.

In Ref. [35], Iachello and Wan proposed a parametrization describing both electric and magnetic form factors in Space-Like and Time-Like regions within the framework of VMD (ρ, ω, ϕ). They started from the hadronic current and to have isospin invariance they introduced two isoscalar form factors F_1^S and F_2^S and two isovector form factors F_1^V and F_2^V.

In case of proton form factors:

$$F_1^p = (F_1^S + F_1^V), \tag{3.35}$$
$$F_2^p = (F_2^S + F_2^V). \tag{3.36}$$

Sachs form factors can be determined via the following formula:

$$G_M^p = (F_1^S + F_1^V) + (F_2^S + F_2^V), \tag{3.37}$$
$$G_E^p = (F_1^S + F_1^V) - \tau(F_2^S + F_2^V), \tag{3.38}$$
$$G_M^n = (F_1^S - F_1^V) + (F_2^S - F_2^V), \tag{3.39}$$
$$G_E^n = (F_1^S - F_1^V) - \tau(F_2^S - F_2^V), \tag{3.40}$$

where $\tau = \frac{Q^2}{4M_p^2} = -\frac{q^2}{4M_p^2}$.

3.5.1.1 Space-Like parametrization

In this model, the Space-Like Dirac and Pauli form factors are parametrized as:

$$F_1^S(Q^2) = \frac{1}{2}g(Q^2)\left[(1-\beta_\omega-\beta_\phi) + \beta_\omega\frac{M_\omega^2}{M_\omega^2+Q^2} + \beta_\phi\frac{M_\phi^2}{M_\phi^2+Q^2}\right], \tag{3.41}$$
$$F_1^V(Q^2) = \frac{1}{2}g(Q^2)\left[(1-\beta_\rho) + \beta_\rho\frac{M_\rho^2}{M_\rho^2+Q^2}\right], \tag{3.42}$$
$$F_2^S(Q^2) = \frac{1}{2}g(Q^2)\left[(-0.12-\alpha_\phi)\frac{M_\omega^2}{M_\omega^2+Q^2} + \alpha_\phi\frac{M_\phi^2}{M_\phi^2+Q^2}\right], \tag{3.43}$$
$$F_2^V(Q^2) = \frac{1}{2}g(Q^2)\left[3.706\frac{M_\rho^2}{M_\rho^2+Q^2}\right], \tag{3.44}$$

where $g(Q^2) = (1 + \gamma Q^2)^{-2}$ is the intrinsic form factor and $\gamma = 0.25$ (GeV/c^2)$^{-2}$ a size parameter also fitted to data. $\beta_\rho = 0.672$, $\beta_\omega = 1.102$, $\beta_\phi = 0.112$ and $\alpha_\phi = -0.052$ are coupling constants given in Table I which were adjusted to fit the data in Ref. [36]. Standard values of the masses ($M_\rho = 0.765$ (GeV/c^2), $M_\omega = 0.783$ (GeV/c^2) and $M_\phi = 1.019$ (GeV/c^2)) and width ($\Gamma_\rho = 0.112$ GeV/c^2) were used. The isoscalar form factors only depend on ω and ϕ mesons whereas ρ meson only contributes to the isovector form factors. F_1^S, F_1^V, F_2^S and F_2^V are defined to ensure the observed nucleon charges and magnetic moments at $q^2 = 0$ (GeV/c^2)^2.

To take into account the ρ width, the following change is applied [37]:

$$\frac{M_\rho^2}{M_\rho^2 + Q^2} \rightarrow \frac{M_\rho^2 + 8\Gamma_\rho M_\pi/\pi}{M_\rho^2 + Q^2 + (4M_\pi^2 + Q^2)\Gamma_\rho \alpha(Q^2)/M_\pi}, \tag{3.45}$$

where

$$\alpha(Q^2) = \frac{2}{\pi}\left[\frac{Q^2 + 4M_\pi^2}{Q^2}\right]^{1/2} ln\left[\frac{\sqrt{Q^2 + 4M_\pi^2} + \sqrt{Q^2}}{2M_\pi}\right]. \tag{3.46}$$

3.5.1.2 Time-Like parametrization

In Time-Like, the expressions are obtained by replacing Q^2 by $-q^2$:

$$F_1^S(q^2) = \frac{1}{2}g(q^2)\left[(1 - \beta_\omega - \beta_\phi) + \beta_\omega \frac{M_\omega^2}{M_\omega^2 - q^2} + \beta_\phi \frac{M_\phi^2}{M_\phi^2 - q^2}\right], \tag{3.47}$$

$$F_1^V(q^2) = \frac{1}{2}g(q^2)\left[(1 - \beta_\rho) + \beta_\rho \frac{M_\rho^2}{M_\rho^2 - q^2}\right], \tag{3.48}$$

$$F_2^S(q^2) = \frac{1}{2}g(q^2)\left[(-0.12 - \alpha_\phi) \frac{M_\omega^2}{M_\omega^2 - q^2} + \alpha_\phi \frac{M_\phi^2}{M_\phi^2 - q^2}\right], \tag{3.49}$$

$$F_2^V(q^2) = \frac{1}{2}g(q^2)\left[3.706 \frac{M_\rho^2}{M_\rho^2 - q^2}\right]. \tag{3.50}$$

An imaginary part is introduced in the intrinsic form factor

$$g(q^2) = \frac{1}{(1 - \gamma e^{i\theta} q^2)^2}, \tag{3.51}$$

where $\theta = 53°$. The phase θ takes into account the annihilation channels in the Time-Like region and is adjusted to fit the data for $|G_M^p|$ (see for instance Fig. 3.8).

The ρ meson term becomes also complex:

$$\frac{M_\rho^2}{M_\rho^2 - q^2} \rightarrow \frac{M_\rho^2 + 8\Gamma_\rho M_\pi/\pi}{M_\rho^2 - q^2 + (4M_\pi^2 - q^2)\Gamma_\rho \alpha(q^2)/M_\pi + i\Gamma_\rho 4M_\pi \beta(q^2)}, \tag{3.52}$$

where

$$\alpha(q^2) = \frac{2}{\pi}\left[\frac{q^2 - 4M_\pi^2}{q^2}\right]^{1/2} ln\left[\frac{\sqrt{q^2 - 4M_\pi^2} + \sqrt{q^2}}{2M_\pi}\right], \tag{3.53}$$

and

$$\beta(q^2) = \sqrt{\frac{\left[\frac{q^2}{4M_\pi^2} - 1\right]^3}{\frac{q^2}{4M_\pi^2}}} \quad \text{when } q^2 \geq 4M_\pi^2, \tag{3.54}$$

$$\beta(q^2) = 0 \quad \text{when } q^2 < 4M_\pi^2. \tag{3.55}$$

The phase vanishes for $q^2 < 4M_\pi^2$ due to the absence of hadronic channels in this case.

To avoid the ω and ϕ divergences, we added two changes

$$M_\omega \to M_\omega + i\Gamma_\omega/2 \quad \text{and} \quad M_\phi \to M_\phi + i\Gamma_\phi/2, \tag{3.56}$$

leading to

$$M_\omega^2 \to M_\omega^2 + iM_\omega\Gamma_\omega \quad \text{and} \quad M_\phi^2 \to M_\phi^2 + iM_\phi\Gamma_\phi, \tag{3.57}$$

since we neglect the $\Gamma^2/4$ terms (3 order of magnitude smaller than $M\Gamma$ terms). With $M_\omega = 0.783$ (GeV/c^2) and $\Gamma_\omega = 0.0085$ (GeV/c^2) from the particle data book, one finds $\Delta M^2 = 2M\Delta M = 0.013$ (GeV/c^2)^2. By introducing the changes to avoid the ω divergence, ΔM^2 becomes 0.022 (GeV/c^2)^2.

In Fig. 3.8, $|G_M^p|$ ($|G_E^p|$) on the left (right) hand side are displayed as a function of q^2 in Time-Like and unphysical region. ρ, ω and ϕ resonances are clearly visible in the unphysical region.

This parametrization verify the asymptotic behaviour and that

$$G_E^p(0) = 1, \qquad G_M^p(0) = \frac{\mu^p}{\mu^N}. \tag{3.58}$$

3.5.2 "pQCD inspired"

A second model [38] able to describe the data in Time-Like region is inspired by the perturbative QCD (pQCD) prescription and does not show any resonances. The G_E^p and G_M^p are expressed as follows (valid when $q^2 > \Lambda^2$):

$$|G_E^p| = |G_M^p| = \frac{A(N)}{q^4(ln^2\frac{q^2}{\Lambda^2} + \pi^2)}, \tag{3.59}$$

where $\Lambda = 0.3$ (GeV/c^2) and $A(p) = 98$ (GeV/c^2)^4 was obtained fitting data. Assuming $|G_E^p| = |G_M^p|$, implies that $F_1^p + F_2^p = F_1^p + \tau F_2^p$ therefore $F_2^p = 0$ and $|G_E^p| = |G_M^p| = F_1^p$.

Fig. 3.8 presents, as a function of q^2, $|G_M^p|$ on the left side and $|G_E^p|$ on the right one. For the "pQCD inspired" (red curves) both curves are identical ($|G_E^p| = |G_M^p|$).

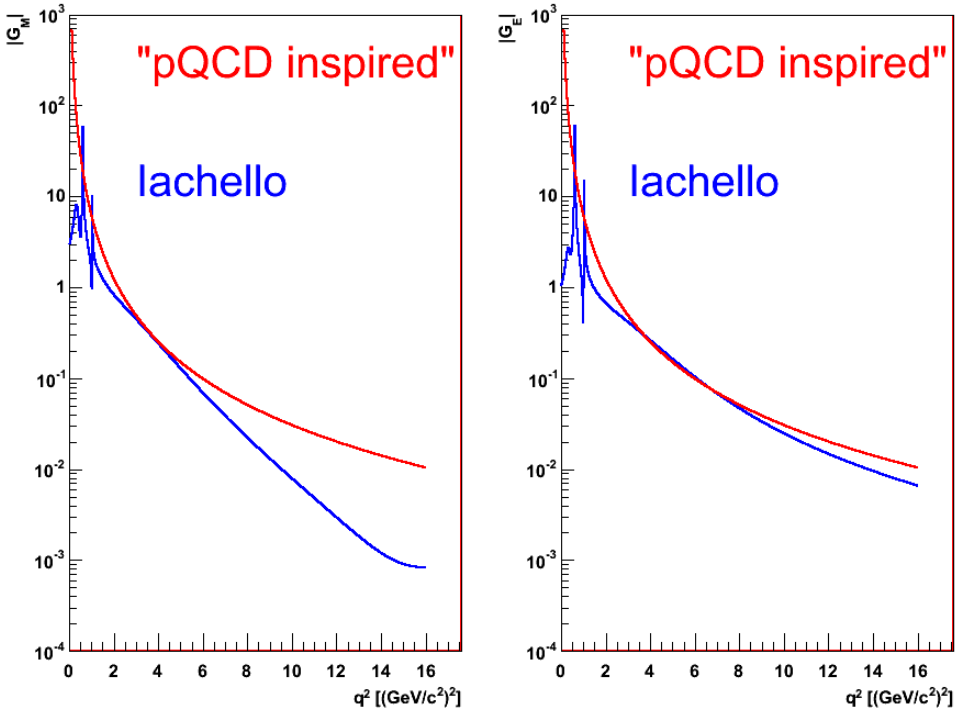

Figure 3.8: Sachs Form Factors: $|G_M^p|$ (left side) and $|G_E^p|$ (right side) are displayed depending on q^2 in TL including the unphysical region. Red (blue) color corresponds to the "pQCD inspired" (VMD) parametrization.

3.5.3 Comparison

Fig. 3.9 presents $|G_{eff}^p|$ determined for both parametrizations as a function of q^2 in Time-Like and unphysical region. Data from [32], [39], [40] and [41] (BABAR, BES and E835) are also plotted. "pQCD inspired" parametrization nicely reproduces the data. Above $q^2 = 8$ (GeV/c^2)^2, a discrepancy appears between VMD parametrization and E835 data.

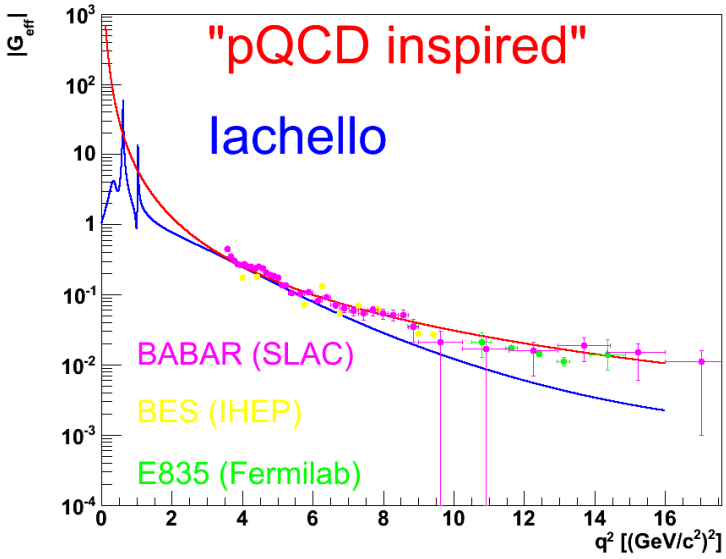

Figure 3.9: $|G^p_{eff}|$ is displayed depending on q^2 in TL including the unphysical region. Red (blue) color corresponds to the "pQCD inspired" (VMD) parametrization. Data are from BABAR (purple, [32]), BES (yellow, [39]) and E835 (green, [40] and [41]).

Another way to compare both parametrizations consists in looking at the ratio $R = |G^p_E|/|G^p_M|$ as a function of q^2. Red color stands for the "pQCD inspired" parametrization. In this case, R is equal to one (i.e.: $|G^p_E| = |G^p_M|$). Blue color represents Iachello parametrization. Its behaviour has a complete different trend due to the structures at the meson poles are visible also in the ratio which yields to a maximum around 15 $(\mathrm{GeV/c^2})^2$. BABAR [32] and LEAR [33] data sets do not help to separate the parametrizations.

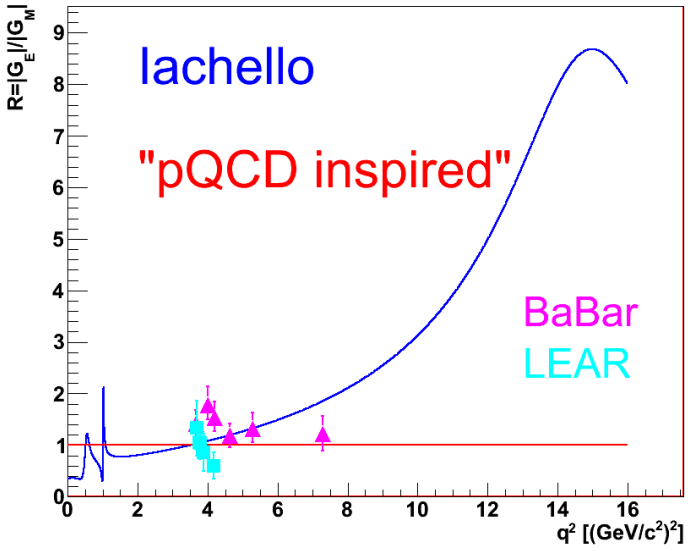

Figure 3.10: Ratio $R = |G^p_E|/|G^p_M|$. Red (blue) corresponds to "pQCD inspired" (Iachello) parametrization.

3.6 Other form factor studies

3.6.1 Foreseen measurements via $\overline{p}p \to e^+e^-$ reaction

The full study of the feasibility of the proton form factor measurements at $\overline{\text{P}}$ANDA in the Time-Like region within the annihilation process $\overline{p}p \to e^+e^-$ can be found in [8].

The differential cross section $\frac{d\sigma}{dcos\theta_e^*}$ in the center of mass for this process is given in Eq. 3.28. It depends on the moduli squared of the proton electromagnetic form factors as [42]. The individual determination of $|G_E^p|$ and $|G_M^p|$ requires the measurement of the angular distribution of the outgoing leptons, at a fixed total energy $s = q^2$.

Counting rates were evaluated on the basis of Eq. (3.28). A parametrization of the effective form factor G_{eff} measurements in the Time-Like region was used [43] and three different hypothesis were taken for $|G_E^p|$. Besides the case $|G_E^p| = |G_M^p|$, $(R = 1)$, which is strictly valid only at threshold, the cases $R = 0$ and the case $R = 3$, were also considered. The corresponding angular distributions were built keeping the same total cross section at each q^2. They are shown in Fig. 3.11, for three values of $q^2 = 5.4$, 8.2, 13.8 $(\text{GeV/c}^2)^2$. The reported error bars are statistical only. The sensitivity to R decreases when q^2 increases, due the fast decrease of the cross section and of the relative weight of the electric term.

The identification of hadrons and leptons requires information from the micro vertex detector, the straw tubes, the GEM detectors, the time of flight detector, the electromagnetic calorimeter and the Cherenkov detectors.

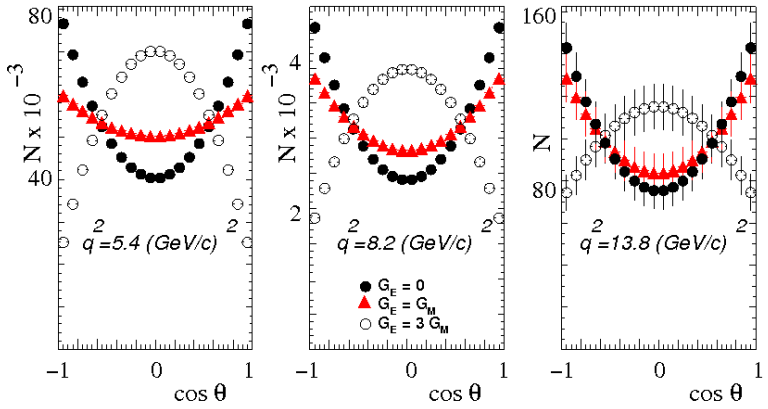

Figure 3.11: $\overline{p}p \to e^+e^-$ CM angular distributions at q^2=5.4, 8.2, and 13.8 $(\text{GeV/c}^2)^2$, and three different hypothesis: $R = 0$ (black solid circles), $R = 1$ (red triangles), and $R = 3$ (black open circles), keeping the same value of the total cross section [8].

Simulations were based on the same $\overline{\text{P}}$ANDA software as the one used for the physics benchmark simulations presented in [7]. Simulations are done in two steps, the first one being the propagation of the particles through the detectors and the digitalization of the information including a model for electronic noise. The second step is the reconstruction of physical quantities (momentum, ratio energy loss to path length in each straw tubes, energy loss in the electromagnetic calorimeter, Cherenkov angle) important for electron

identification. The probability of a given particle to be identify as an electron, muon, pion, kaon or proton is calculated for each $\overline{\text{P}}$ANDA sub-detector. Then a global Particle IDentification (PID) likelihood is determined. Thresholds can be adjusted to ensure a high background suppression while keeping as much as signal as possible.

Reactions involving two or more hadrons in the final channel constitute an important background. In particular, the annihilations into two hadrons ($\overline{p}p \to \pi^0\pi^0$, $\overline{p}p \to \pi^+\pi^-$ and $\overline{p}p \to K^+K^-$) are the most difficult to eliminate since the angular correlation of the two charged particles is very different in a 3-body reaction. Only in a 2-body reaction, one has back to back emission in the center of mass system. Moreover, the two charged particles missing mass is an efficient tool to separate 3-body from 2-body reactions. Concerning $\overline{p}p \to \pi^0\pi^0$, photons from the π° can produce e^+e^- pairs after conversion in material. One (both) π° via Dalitz decay can also give e^+e^- pair(s) but with probability 10^{-2} (10^{-4}). For $\overline{p}p \to \pi^+\pi^-$ and $\overline{p}p \to K^+K^-$, kaons, being heavier, have lower probability of misidentification than pions. Therefore, the $\overline{p}p$ annihilations into two pions were studied using detailed simulations.

To simulate $\overline{p}p \to \pi^0\pi^0$ and $\overline{p}p \to \pi^+\pi^-$, angular distributions were extrapolated from parametrization of data [44, 45, 46, 47, 48, 49]. Both $\overline{p}p \to \pi^0\pi^0$ and $\overline{p}p \to \pi^+\pi^-$ cross sections were estimated to be about six orders of magnitude larger than for the reaction $\overline{p}p \to e^+e^-$.

Due to the background to signal cross section ratio of about 10^6, background samples with at least 10^8 events were simulated at several q^2 values. To discriminate pions from electrons, cuts have been applied to the PID likelihood for the assumption that the detected particle is an electron. Applying the PID cut a rejection factor of a few times 10^7 is reached. Further selection based on the reaction vertex and on the kinematical fit (which includes 4-momentum constraint) is applied. From this a confidence level (CL) is calculated for both e^+e^- and $\pi^+\pi^-$ hypothesis. Confidence level brings in an additional rejection factor of the background of $\simeq 100$. Finally, combining the confidence level with the PID cuts, it results an overall background suppression factor of the order of a few 10^9 which leads to a contamination far below the percent level.

Fig. 3.12 shows the expected statistical uncertainty on R as a function of q^2 as a yellow band for the case $R = 1$, and compared with the existing values from Ref. [33] (squares) and [32] (triangles).

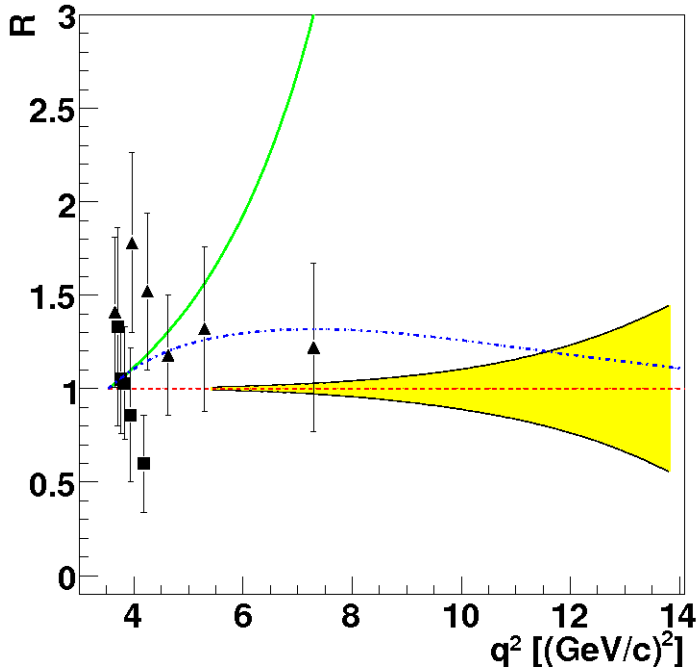

Figure 3.12: Expected statistical precision on the determination of the ratio R from [8], (yellow band) for $R = 1$, as a function of q^2, compared with the existing data from [32] (triangles) and [33] (squares). Curves are theoretical predictions: "pQCD inspired" (red dashed line [50, 51]), VMD (green solid line [36] and blue dashed line [52]).

Model predictions display quite a large dispersion, as shown in Fig. 3.12. A detailed description of the models can be found in Ref. [53]. It is also worth noting that these models give different values for the polarization observables.

At larger q^2, where the sensitivity of the experiment will make the extraction of R meaningless, it will then be possible to extract $|G_M^p|$ under a definite hypothesis on the ratio, notably $R = 1$, as done in previous measurements. Conditioned by a precise knowledge of the luminosity, the absolute cross section can be measured up to $q^2 \sim 28$ $(\mathrm{GeV/c^2})^2$, and moreover the individual measurement of $|G_M^p|$ and $|G_E^p|$ will be possible.

3.6.2 The $\overline{p}p \to \mu^+\mu^-$ reaction

The expression of the angular distribution of $\overline{p}p \to \mu^+\mu^-$ is the same as $\overline{p}p \to e^+e^-$ since the lepton mass difference has a negligible effect. Measuring the $\overline{p}p \to \mu^+\mu^-$ could bring complementary information on the proton electromagnetic form factors. Since the muon mass is closer to pion mass than the electron mass to the pion mass, the kinematics constraints do not help to reject the huge hadronic background. The muon identification relies only on the muon detector. As previously said, the yoke is segmented to allow the separation of primary muons from secondary muons coming from the pion decays. Detailed simulations will be performed soon within the collaboration to determine if a sufficient rejection background factor can be achieved to extract the electromagnetic proton form factors.

3.6.3 The interest of polarization

Although the challenges are technically large, having polarized antiproton beam at FAIR and/or polarized target in $\overline{\mathrm{P}}$ANDA is discussed. Polarization would open a new field of investigation and give access to new observables. Such a beam would allow to access for the first time the phase difference of the electric and magnetic form factors.

A general formalism to calculate the polarization observables for the reaction $\overline{p}p \to \pi^{\circ}e^{+}e^{-}$ is developed in [54]. The matrix element and the observables can be expressed in terms of six scalar amplitudes (complex functions of three kinematical variables) which determine the reaction dynamics. The concrete expression of these amplitudes contains the model which is chosen for the description of the underlying physics. The numerical prediction are given in the frame of the model [38] in the kinematical range accessible in the PANDA experiment at FAIR.

The main results are illustrated here for single and double spin observables. The observables are represented in Fig. 3.13 as a function of $\cos\theta$ (where θ is the angle between the momenta of the antiproton and the virtual photon) for a center-of-mass energy squared s= 5.5 GeV^2 (corresponding to $E_{\bar{p}}^{Lab} = 2$ GeV) and three q^2 values: 0.5 (GeV/c^2)^2 (solid line), 2 (GeV/c^2)^2 (dashed line) and 4 (GeV/c^2)^2 (dash-dotted line). It was shown that the single spin observables A_y and $\bar{A}_y$ coincide in Born approximation. A difference between these two values, would be an experimental signature of the presence of terms beyond the Born approximation.

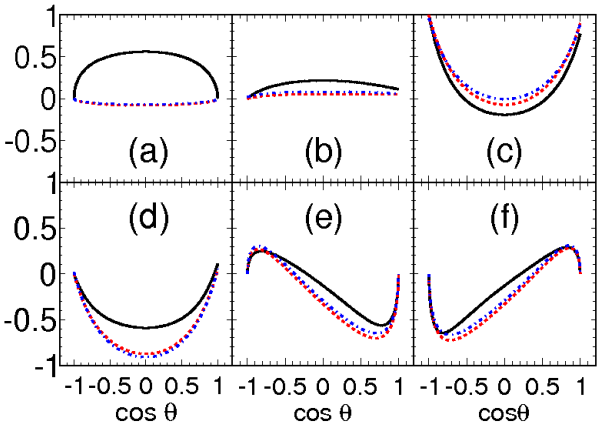

Figure 3.13: From [54], polarization observables as function of $\cos\theta$ (where θ is the angle between the momenta of the antiproton and the virtual photon) for $s = 5.5$ GeV^2 and for three values of the momentum transfer squared q^2 : $q^2 = 0.5$ (GeV/c^2)^2(solid line), $q^2 = 2$ (GeV/c^2)^2(dashed line), $q^2 = 4$ (GeV/c^2)^2 (dash-dotted line): (a) single spin asymmetry A_y ($\equiv \bar{A}_y$ in Born approximation); double spin correlations: (b) C_{yy}; (c) C_{zz}; (d) C_{xx}; (e) C_{xz}; (f) C_{zx}.

The double spin correlations are in general large and strongly depend on energy and angle. This is illustrated in Fig. 3.14 for a particular case in the 2D plot of C_{zx} as function of $\cos\theta$ (where θ is the angle between the momenta of the antiproton and the virtual photon) and q^2. The large structures correspond to the masses of the mesons resonances considered in the form factor parametrization from [36]. Forward and backward angles are the most favourable for the experimental measurements of this correlation.

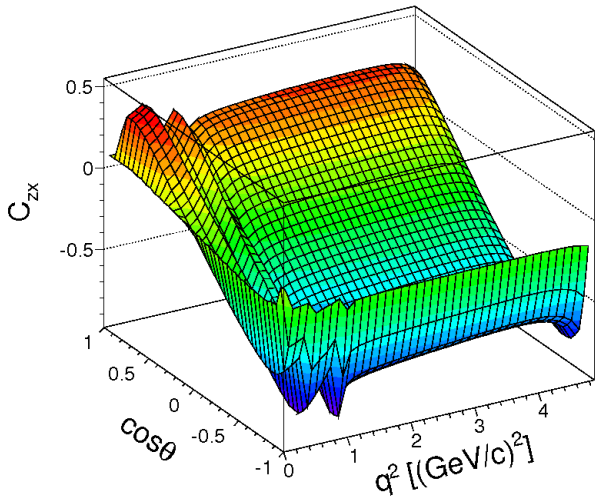

Figure 3.14: C_{zx} as function of $\cos\theta$ and q^2 at $s = 5.5$ GeV^2, from [54].

Chapter 4

Description of $\overline{p}p \to \pi^\circ e^+ e^-$

In this chapter, I will first present the specificity of the reaction kinematics. Then I will recall briefly the available theoretical predictions. While the TDA approach [55], based on Transition Distribution Amplitude (TDA), is focusing on a specific kinematical region where factorization arguments can be used, namely q^2 close to the total CM energy squared, the one nucleon exchange model [38] will be recalled in a more detailed way. It will be shown how this model was considerably reworked for our purposes. In particular, through a full derivation [56], I will show how one can extract the physical informations out of the e^+e^- angular distribution in a similar way to the one used for the extraction of $|G_E|$ and $|G_M|$ from the angular distribution of the electron in $\overline{p}p \to e^+e^-$ reaction. In order to realize meaningful simulations, which include not only acceptance, efficiency and resolution effects but also the role played by the limited statistics, I will show the importance of having realistic counting rates. For this, the one nucleon exchange model was asked to reproduce the already available data on the reaction $\overline{p}p \to \pi^\circ\gamma$, which corresponds to the photon point where the e^+e^- invariant mass is equal to 0.

4.1 $\overline{p}p \to \pi^\circ e^+ e^-$ kinematics

The reaction $\overline{p}p \to \pi^\circ e^+ e^-$ has a three body final state. Useful relations can be derived among the kinematical variables. Using the notation of Fig. 4.7, the virtual photon mass squared q^2 is defined as follows:

$$\begin{aligned} q^2 &= (p_{e^+} + p_{e^-})^2 , \qquad (4.1) \\ &= (p_{\overline{p}} + p_p - p_{\pi^0})^2 , \\ &= s + M_{\pi^0}^2 - 2p_{\overline{p}}.p_{\pi^0} - 2M_p E_{\pi^0} , \qquad (4.2) \end{aligned}$$

where $p_{\overline{p}}.p_{\pi^0} = E_{\overline{p}}E_{\pi^0} - |\overrightarrow{p}_{\overline{p}}||\overrightarrow{p}_{\pi^0}|cos\theta_{\pi^0}$.

At a fixed beam kinetic energy $T_{\overline{p}}$ in lab, the total CM energy squared is:

$$s = 2M_p \left(T_{\overline{p}} + 2M_p\right) , \qquad (4.3)$$

which leads to a maximum q^2_{max} value (obtained when the π° is emitted at rest) of

$$q^2_{max} = \left(\sqrt{s} - M_{\pi^0}\right)^2 . \qquad (4.4)$$

In Fig. 4.1, the black curve shows q^2_{max} as a function of s. At a given s, the π° can be emitted up to 180° in the lab frame if q^2 is below the red curve, otherwise there is an angular limit for the π°. In a similar way, the γ^* can be emitted up to 180° in the lab frame if q^2 is below the blue curve, otherwise there is an angular limit for the γ^*. For $q^2 = q^2_{max}$, the π° and γ^* are produced at rest in the CM, they are both emitted at 0° in the laboratory. As an example, Fig. 4.2 displays at s= 5.4 GeV^2 ($T_{\overline{p}}$ = 1 GeV) the angular limit for both π° (red curve) and γ^* (blue curve).

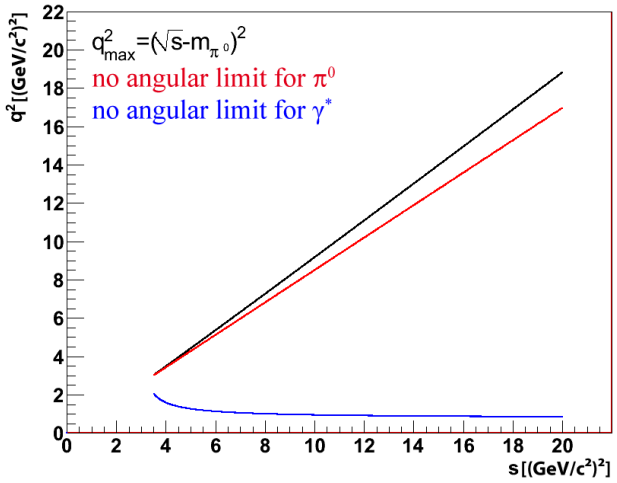

Figure 4.1: For the reaction $\overline{p}p \to \pi^\circ e^+ e^-$, at a fixed value of s, black curve shows the corresponding q^2_{max}. At a q^2 value below the blue (red) curve, there is no angular limit on the virtual photon (π°).

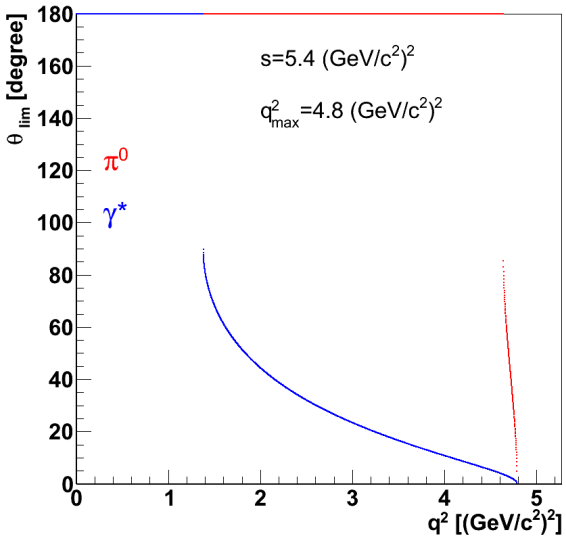

Figure 4.2: For the reaction $\overline{p}p \to \pi^\circ e^+ e^-$, at s= 5.4 GeV^2, the red (blue) curve shows the angular limit in the laboratory on the π° (γ^*).

Fixing q^2 and θ_{π^0} fully determine kinematics. Fig. 4.3 displays, for $\overline{p}p \to \pi^{\circ}e^{+}e^{-}$ at $E_{\overline{p}} = 2$ GeV ($T_{\overline{p}} \sim 1$ GeV) and two q^2 values, in the upper (lower) line the pion (electron) energy as a function of the pion (electron) θ angle in the laboratory. The effect of the q^2 value is clearly visible on both pion and electron energy ranges: increasing the q^2 value implies a lower energy for the pion but also a smaller energy range. It is also worth to note that there are no angular limits on the pion but a limit on the γ^* emission angle in the laboratory. In case of the electron, the available energy range is large from hundred MeV to few GeV. At low energy, the tracking system will have the higher precision, while at high energy, the electromagnetic calorimeter will give the best precision.

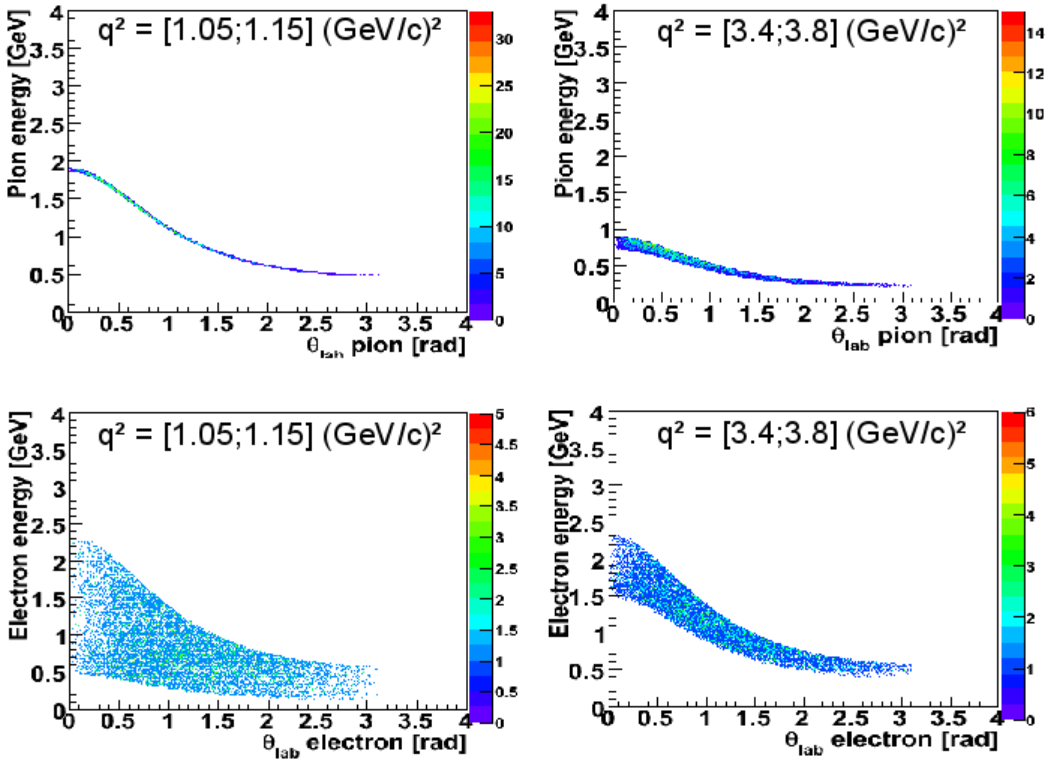

Figure 4.3: $\overline{p}p \to \pi^{\circ}e^{+}e^{-}$ kinematics at $E_{\overline{p}} = 2$ GeV ($T_{\overline{p}} \sim 1$ GeV) and for two q^2 values. Upper plots present the pion energy as a function of the pion θ angle in the laboratory. Lower plots present the electron energy as a function of the electron θ angle in the laboratory.

Since to reconstruct $\overline{p}p \to \pi^{\circ}e^{+}e^{-}$, the π° needs to be detected. Therefore, it is interesting to look at the π° decay into two photons. The minimum opening angle in the laboratory between the two photons (γ_1 and γ_2) is

$$\theta^{lim}_{\gamma_1\gamma_2} = acos\left(1 - 2\frac{M^2_{\pi^{\circ}}}{E^2_{\pi^{\circ}}}\right), \tag{4.5}$$

where $E_{\pi^{\circ}}$ is the pion energy in the laboratory. Fig. 4.4 shows the minimum opening angle in the laboratory between the two photons (γ_1 and γ_2) as a function of $\theta_{\pi^{\circ}}$ for $T_{\overline{p}} = 1$ GeV and different q^2 values. From this figure one can also see that increasing q^2 (at a fixed system energy) increases the minimum opening angle in the laboratory of the two

photons. At this energy, the two photons from the π° decay are clearly separated by at least 3 times the crystal opening angle which is of the order of 2.25°. So the identification of the π° in the electromagnetic calorimeter should be easy. It is worth to note that increasing the antiproton kinetic energy will lower the minimum opening angle.

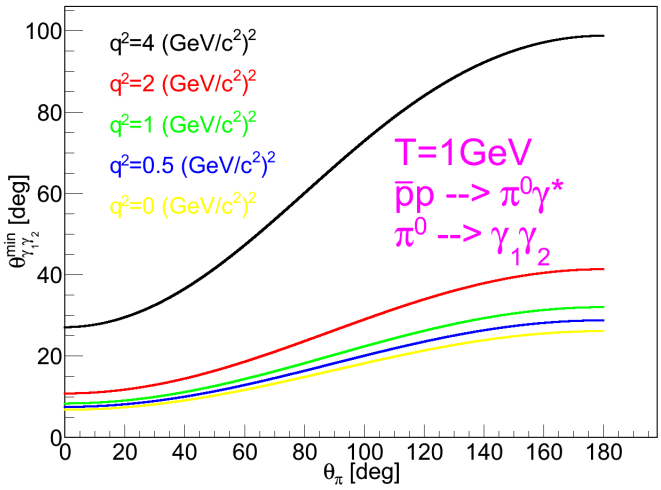

Figure 4.4: Minimum opening angle between the two photons from the π^0 decay in the reaction $\overline{p}p \to \pi^{\circ}\gamma^{*}$ as a function of θ_{π^0} for $T_{\overline{p}} = 1$ GeV and different virtual photon mass squared (q^2) values.

4.2 Different models for $\overline{p}p \to \pi^{\circ}e^{+}e^{-}$

4.2.1 Transition Distribution Amplitude approach

In Ref. [55], J. P. Lansberg, B. Pire and L. Szymanowski present the reaction $\overline{p}p \to \pi^{\circ}\gamma^{*}$ where $\gamma^{*} \to e^{+}e^{-}$ as a factorization of the antiproton Distribution Amplitudes (DA), the hard sub-process amplitude (M_h) and the proton to pion transition distribution amplitude so-called TDA (see Fig. 4.5). TDAs are non-perturbative objects describing the transition between two particles (here p to π).

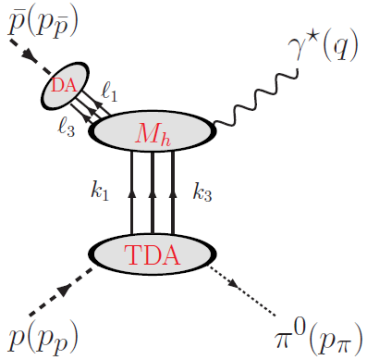

Figure 4.5: Factorization of $\overline{p}p \to \pi^{\circ}\gamma^{*}$ into antiproton distribution amplitudes (DA), hard sub-process amplitude (M_h) and $p \to \pi$ transition distribution amplitudes (TDA), from [55].

This factorization is valid for q^2 of the order of s and for small t region where $t = (p_\pi - p_p)^2$ implying that the virtual photon mass squared is close to the system energy. Defining the z axis along the colliding axis, this t small means π° emitted at 180° in the laboratory. The exchange graph, π° emitted by the antiproton, corresponds to π° close to 0°. In this paper, one can find a first evaluation of the differential cross section $d\sigma/dtdq^2$ at $\Delta_T = 0$ GeV (see Fig. 4.6) where Δ_T is the transverse component of $(p_\pi - p_p)$ for the backward production of the π. At $s = 10$ GeV^2, integrating over q^2 from 7 to 8 (GeV/c^2)^2 and dt corresponding to $\Delta_T < 0.5$ GeV leads to a cross section around 100 fb therefore 200 counts with the $\overline{\text{P}}$ANDA integrated luminosity of 2 fb^{-1} without neither efficiency nor acceptance factors. Due to charge symmetry an identical result will be obtained at small u= $(p_\pi - p_{\overline{p}})^2$ i.e.: when the pion goes at forward angle.

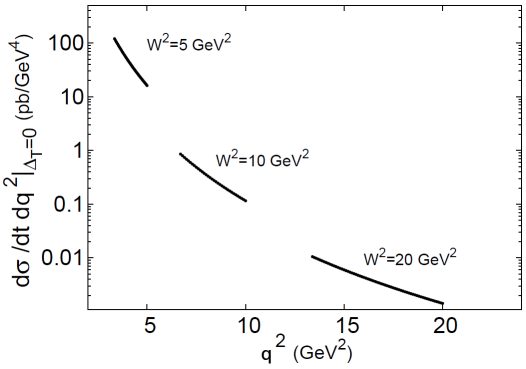

Figure 4.6: Evaluation of the $\overline{p}p \to \pi^\circ\gamma^*$ differential cross section for 3 values of the total system energy (s=W^2), from [55].

As a conclusion, this model is valid only in a very well defined and restricted π° angular range. Furthermore, it is not suited for the proton form factor far below threshold since it is valid for q^2 close to s.

4.2.2 One nucleon exchange model

The process $\overline{p}p \to \pi^\circ\gamma^*$ where $\gamma^* \to e^+e^-$ (see Fig. 4.7) is described in Ref. [38] within a phenomenological approach based on Compton-like Feynman amplitudes.

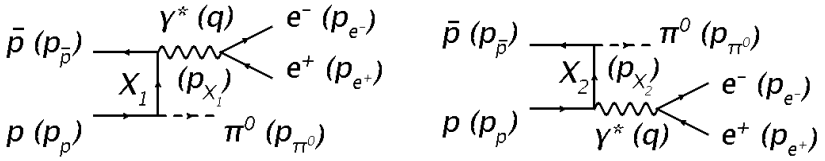

Figure 4.7: $\overline{p}p \to \pi^\circ e^+e^-$ diagrams. Value in parenthesis represent the corresponding 4-vectors.

4.2.2.1 Differential cross sections

The differential cross section for $\overline{p}p \to \pi^\circ\gamma^*$ is written as:

$$\begin{aligned} d^3\sigma &= \frac{\alpha_{em}^2}{6s\pi r}\frac{\beta(q^2+2M_e^2)}{(q^2)^2}D\frac{d^3\overrightarrow{p}_{\pi^0}}{2\pi E_{\pi^0}} \\ d^2\sigma &= \frac{\alpha^2}{6s\pi r}\frac{\beta(q^2+2M_e^2)}{(q^2)^2}D\frac{q^2M_p^2dq^2dcos\theta_{\pi^0}}{s^2(1-rcos\theta_{\pi^0})^2}, \end{aligned} \tag{4.6}$$

where,

$$s = 2M_p(M_p+E_{\overline{p}}), \tag{4.7}$$

$$r = \sqrt{1-4M_p^2/s}, \tag{4.8}$$

$$\beta = \sqrt{1-4M_e^2/q^2}, \tag{4.9}$$

and D is the hadronic matrix element.

The hadronic matrix element is related to the nucleon form factors by

$$D = |f_{2p}|^2\left[\frac{E_{\overline{p}}-M_p}{M_p} - \frac{1}{2}(1-\frac{q^2}{4M_p^2})\frac{(1-X)^2}{X}\right] + |f_{1p}-f_{2p}|^2\frac{(X+1)^2}{X}, \tag{4.10}$$

where

$$X = \frac{s-q^2}{2M_pE_{\pi^0}} - 1, \tag{4.11}$$

$$f_{iN}(q^2) = g(M_{\pi^0}^2)F_i^N(q^2). \tag{4.12}$$

Here, $F_i^N(q^2)$ are the Pauli and Dirac form factors.

Unfortunately, no angular distribution for the reaction $\gamma^* \to e^+e^-$ is given in this article.

4.2.2.2 Counting rate

To determine the counting rate, the first step is the study of the differential cross section. Fig. 4.8 presents as an example $\frac{d\sigma}{dq^2}$ for an antiproton beam total energy $E_{\overline{p}} = 2$ GeV and for both form factor parametrizations previously described (section 3.5). Black line corresponds to VMD parametrization and blue dashed line to the "pQCD inspired" one. Mesonic resonances are clearly visible in case of VMD parametrization.

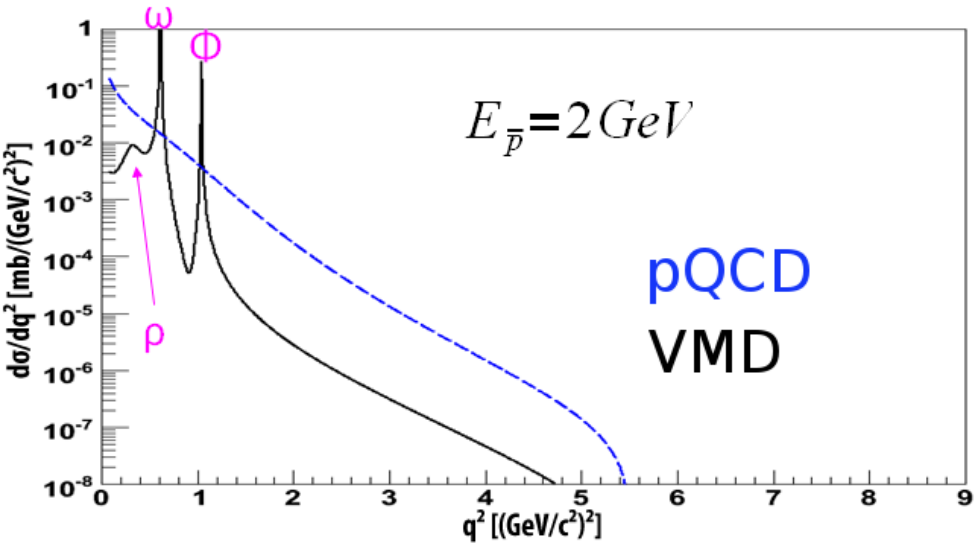

Figure 4.8: $\frac{d\sigma}{dq^2}$ for $\overline{p}p \to \pi^\circ\gamma^*$ for both form factor parametrizations at $E_{\overline{p}} = 2$ GeV. Black line corresponds to VMD inspired parametrization and blue dashed line to pQCD one.

Then integrating over q^2 from $\Lambda^2 = 0.3^2$ (GeV/c^2)^2 (see [38]) up to $(\sqrt{s} - M_\pi)^2$ (GeV/c^2)^2, the cross section has been determined and assuming a luminosity of 2 10^{32} cm^{-2}s^{-1} with a 10^7s long data taking (corresponding to 2 fb^{-1}), the number of counts is calculated. Table 4.1 shows the results for three different energies of the antiproton. A phenomenological fit of $\overline{p}p \to n\pi$ data (n=0,1,2,...) for $T_{\overline{p}} = 6$ GeV ($E_{\overline{p}} = 7$ GeV) predicts a $\overline{p}p \to \pi^\circ\pi^+\pi^-$ cross section of the order of 75 μb [57, 58] which has to be compared with the 10 μb (8 μb) obtained for $\overline{p}p \to \pi^\circ e^+e^-$ within pQCD (VMD) parametrization. This leads to a cross section ratio $\frac{\sigma(\overline{p}p\to\pi^\circ\pi^+\pi^-)}{\sigma(\overline{p}p\to\pi^\circ e^+e^-)} \simeq 8$. It has been shown that $\frac{\sigma(\overline{p}p\to\pi^+\pi^-)}{\sigma(\overline{p}p\to e^+e^-)} \simeq 10^6$ (from s=5 up to s=16 GeV^2) [8, 59]. From this, we concluded that the cross section value obtained by the phenomenological approach are overestimated. J. Van de Wiele [56] then proposed to calculate the five fold differential cross section of $\overline{p}p \to \pi^\circ e^+e^-$ using the same one nucleon exchange model but constraining it to the $\overline{p}p \to \pi^\circ\gamma$ data since there are no available data for $\overline{p}p \to \pi^\circ\gamma^*$. For this study a formalism based on hadronic tensors was developed.

$E_{\overline{p}}$ (GeV)	σ_{pQCD} (mb)	Counts$_{pQCD}$	σ_{VMD} (mb)	Counts$_{VMD}$
2	0.027	5.4 10^{10}	0.020	4.0 10^{10}
7	0.010	2.0 10^{10}	0.008	1.6 10^{10}
15	0.005	1.0 10^{10}	0.004	0.8 10^{10}

Table 4.1: Counts integrating over the full q^2 range the differential cross section $d\sigma/dq^2$ of Fig. 4.8 assuming an integrated luminosity of 2 fb^{-1}.

4.2.3 New calculation of one nucleon exchange model

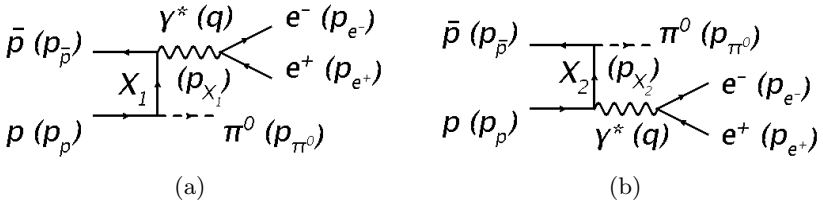

Figure 4.9: $\overline{p}p \to \pi^\circ e^+ e^-$ diagrams.

Before calculating the differential cross section (J. Van de Wiele, [56]) of $\overline{p}p \to \pi^\circ e^+ e^-$ in a specific frame, it is necessary to determine the amplitude $\mathcal{M} = \mathcal{M}_a + \mathcal{M}_b$ of the corresponding diagrams Fig. 4.9(a) and 4.9(b).

4.2.3.1 $\overline{p}p \to \pi^\circ e^+ e^-$ amplitude

For both diagrams, the leptonic current is:

$$J_l^\nu \left(m_{e^+}, m_{e^-}\right) = -ie\overline{u}\left(m_{e^-}\right)\gamma^\nu v\left(m_{e^+}\right), \tag{4.13}$$

where e is the electron charge, m_i stands for the spin of the particle i, γ^i $(i = 0, .., 3)$ are the 4X4 Dirac matrices, $\overline{u}$ and v are spinors.

Then, starting from the Fig. 4.9(a), the exchanged nucleon four momentum p_{X_1} is:

$$p_{X_1} = p_p - p_{\pi^\circ}, \tag{4.14}$$

and the amplitude $\mathcal{M}_a$ is given by:

$$\begin{aligned} \mathcal{M}_a\left(m_{e^+}, m_{e^-}, m_{\overline{p}}, m_p\right) &= \overline{v}\left(m_{\overline{p}}\right)\Gamma_a^\mu u\left(m_p\right) i\left(-\frac{g_{\mu\nu}}{q^2}\right) J_l^\nu\left(m_{e^+}, m_{e^-}\right), & (4.15)\\ \Gamma_a^\mu &= V_{NN\gamma}^\mu i P_F\left(N, p_{X_1}\right) V_{NN\pi}. & (4.16) \end{aligned}$$

Here, $\overline{v}$ and u are spinors, $i\left(-\frac{g_{\mu\nu}}{q^2}\right)$ is the photon propagator, P_F is the nucleon propagator, $V_{NN\pi}$ is the pseudo-vector nucleon-nucleon-pion coupling and $V_{NN\gamma}^\mu$ is nucleon-nucleon-photon coupling which contains the form factor dependence:

$$V_{NN\gamma}^\mu = -ie\left(F_1^p\gamma^\mu - i\frac{F_2^p}{2M_p}\sigma^{\mu\nu}q_\nu\right), \tag{4.17}$$

where $e = \sqrt{4\pi\alpha_{em}}$, F_1^p and F_2^p are the Pauli and Dirac form factors. Since $V_{NN\gamma}^\mu$ is linear in F_1^p and F_2^p, it is also linear in G_E^p and G_M^p.

In a similar way, using the second diagram (Fig. 4.9(b)), the exchanged nucleon four momentum p_{X_2} is:

$$p_{X_2} = p_{\pi^\circ} - p_{\overline{p}}, \tag{4.18}$$

and the amplitude $\mathcal{M}_b$ is given by:

$$\mathcal{M}_b\left(m_{e^+}, m_{e^-}, m_{\overline{p}}, m_p\right) = \overline{v}\left(m_{\overline{p}}\right)\Gamma_b^\mu u\left(m_p\right) i\left(-\frac{g_{\mu\nu}}{q^2}\right) J_l^\nu\left(m_{e^+}, m_{e^-}\right), \quad (4.19)$$

$$\Gamma_b^\mu = V_{NN\pi} i P_F\left(N, p_{X_2}\right) V_{NN\gamma}^\mu. \quad (4.20)$$

The amplitude of $\overline{p}p \to \pi^\circ e^+e^-$ taking into account both diagrams is therefore:

$$\mathcal{M}\left(m_{e^+}, m_{e^-}, m_{\overline{p}}, m_p\right) = J_H^\mu\left(m_{\overline{p}}, m_p\right) i\left(-\frac{g_{\mu\nu}}{q^2}\right) J_l^\nu\left(m_{e^+}, m_{e^-}\right), \quad (4.21)$$

$$= -i J_H^\mu\left(m_{\overline{p}}, m_p\right)\left(\frac{1}{q^2}\right) J_{l\mu}\left(m_{e^+}, m_{e^-}\right), \quad (4.22)$$

where

$$J_H^\mu\left(m_{\overline{p}}, m_p\right) = \overline{v}\left(m_{\overline{p}}\right)\Gamma^\mu u\left(m_p\right), \quad (4.23)$$

$$\Gamma^\mu = \Gamma_a^\mu + \Gamma_b^\mu. \quad (4.24)$$

4.2.3.2 Differential cross section

The differential cross section of $\overline{p}p \to \pi^\circ e^+e^-$ is proportional to the amplitude squared $|\mathcal{M}|^2$ previously defined which can be written in terms of hadronic and leptonic tensors:

$$|\mathcal{M}|^2 = \sum_{m_{e^+}, m_{e^-}, m_{\overline{p}}, m_p} |\mathcal{M}\left(m_{e^+}, m_{e^-}, m_{\overline{p}}, m_p\right)|^2, \quad (4.25)$$

$$= \frac{1}{q^4}\mathcal{H}^{\mu\nu}\mathcal{L}_{\mu\nu}, \quad (4.26)$$

where

$$\mathcal{H}^{\mu\nu} = \sum_{m_{\overline{p}}, m_p} J_H^\mu\left(m_{\overline{p}}, m_p\right) J_H^{\nu\,*}\left(m_{\overline{p}}, m_p\right) \quad (4.27)$$

and

$$\mathcal{L}_{\mu\nu} = \sum_{m_{e^+}, m_{e^-}} J_{l\mu}\left(m_{e^+}, m_{e^-}\right) J_{l\nu}{}^*\left(m_{e^+}, m_{e^-}\right), \quad (4.28)$$

$$= 4e^2\left(p_{e^-\mu}p_{e^+\nu} + p_{e^-\nu}p_{e^+\mu} - \frac{q^2}{2}g_{\mu\nu}\right), \quad (4.29)$$

where $p_{i\mu}$ is the μ component of the 4-momenta of the particle i and q_μ is the μ component of the 4-momenta of the virtual photon.

To remove the p_{e^-} dependence, one uses the relation $q = p_{e^+} + p_{e^-}$. The leptonic tensor can be expressed as:

$$\mathcal{L}_{\mu\nu} = 4e^2\left(-p_{e^+\mu}p_{e^+\nu} - p_{e^+\nu}p_{e^+\mu} - \frac{q^2}{2}g_{\mu\nu} + q_\mu p_{e^+\nu} + q_\nu p_{e^+\mu}\right). \quad (4.30)$$

Since there is no polarization, the leptonic tensor is symmetric. The Gauge invariance can be expressed by

$$q_\mu \mathcal{H}^{\mu\nu} = \mathcal{H}^{\mu\nu} q_\nu = 0, \tag{4.31}$$
$$q^\mu \mathcal{L}_{\mu\nu} = \mathcal{L}_{\mu\nu} q^\nu = 0, \tag{4.32}$$

one can deduce:

$$\mathcal{H}^{\mu\nu} \mathcal{L}_{\mu\nu} = \mathcal{H}^{\mu\nu} \mathcal{L}^{red}_{\mu\nu}, \tag{4.33}$$

where $\mathcal{L}^{red}_{\mu\nu}$ is the reduced leptonic tensor:

$$\mathcal{L}^{red}_{\mu\nu} = -4e^2 \left(2p_{e^+\mu} p_{e^+\nu} + \frac{q^2}{2} g_{\mu\nu} \right). \tag{4.34}$$

Considering the three body final state and the 4 conservation laws, there are five independent variables. Since $\frac{d^3\overrightarrow{p}}{E}$ is Lorentz invariant, it is possible to express the π° part of the differential cross section in the laboratory and the positron one in the virtual photon rest frame (noted *) where the Oz axis is defined by the virtual photon momentum in the laboratory. The five fold differential cross section is then:

$$\frac{d^5\sigma}{(dE_{\pi^\circ} d\Omega_{\pi^\circ})_{lab}\, d\Omega^*_{e^+}} = \frac{(\hbar c)^2}{32\,(2\pi)^5\, M_p} \left(\frac{|\overrightarrow{p}_{\pi^\circ}|}{|\overrightarrow{p}_{\overline{p}}|} \right)_{lab} \frac{|\overrightarrow{p}^*_{e^+}|}{\sqrt{q^2}} \frac{|\mathcal{M}|^2}{4}, \tag{4.35}$$

where

$$|\overrightarrow{p}^*_{e^+}| = \frac{\sqrt{q^2}}{2} \sqrt{1 - \frac{4M_e^2}{q^2}}. \tag{4.36}$$

Here, E_{π° (Ω_{π°) stands for the pion energy (solid angle) in the laboratory and $\Omega^*_{e^+}$ is the positron solid angle in the virtual photon rest frame.

As the electromagnetic form factors depend on q^2, it is more convenient to derive the five fold differential cross section as follows:

$$\begin{aligned} \frac{d^5\sigma}{dq^2\,(d\Omega_{\pi^\circ})_{lab}\, d\Omega^*_{e^+}} &= \frac{(\hbar c)^2}{32\,(2\pi)^5\, M_p} \left(\frac{|\overrightarrow{p}_{\pi^\circ}|}{|\overrightarrow{p}_{\overline{p}}|} \right)_{lab} \\ &\times \frac{|\overrightarrow{p}^*_{e^+}|}{\sqrt{q^2}} \frac{1}{2|E_{\overline{p}} + M_p - |\overrightarrow{p}_{\overline{p}}| \frac{E_{\pi^\circ}}{|\overrightarrow{p}_{\pi^\circ}|} cos\theta_{\pi^\circ}|_{lab}} \frac{|\mathcal{M}|^2}{4}. \end{aligned} \tag{4.37}$$

In this specific γ^* rest frame, the gauge invariance leads to:

$$q_\mu \mathcal{H}^{\mu\nu} = 0 \to q_0 \mathcal{H}^{0\nu} + q_i \mathcal{H}^{i\nu} = 0. \tag{4.38}$$

Here $q_i = 0$ $(i = 1, 2, 3)$, so $\mathcal{H}^{0\nu} = 0$. Therefore,

$$\mathcal{H}^{\mu\nu} \mathcal{L}_{\mu\nu} = \mathcal{H}^{ij} \mathcal{L}^{red}_{ij}. \tag{4.39}$$

For convenience, the kinematical factors with the q^2 and π° dependences are included in the effective hadronic tensor $\mathcal{H}^{\mu\nu}_{eff}$ such as:

$$\mathcal{H}^{\mu\nu}_{eff} = \frac{(\hbar c)^2}{32\,(2\pi)^5\, M_p} \left(\frac{|\overrightarrow{p}_{\pi^\circ}|}{|\overrightarrow{p}_{\overline{p}}|} \right)_{lab} \frac{|\overrightarrow{p}^*_{e^+}|}{\sqrt{q^2}} \frac{1}{2|E_{\overline{p}} + M_p - |\overrightarrow{p}_{\overline{p}}| \frac{E_{\pi^\circ}}{|\overrightarrow{p}_{\pi^\circ}|} cos\theta_{\pi^\circ}|_{lab}} \frac{\mathcal{H}^{\mu\nu}}{4q^4}. \tag{4.40}$$

So,

$$\frac{d^5\sigma}{dq^2\,(d\Omega_{\pi^\circ})_{lab}\,d\Omega^*_{e^+}} = \mathcal{H}^{ij}_{eff}\mathcal{L}^{red}_{ij}. \tag{4.41}$$

Developing $\mathcal{H}^{ij}_{eff}\mathcal{L}^{red}_{ij}$:

$$\begin{aligned}\mathcal{H}^{ij}_{eff}\mathcal{L}^{red}_{ij} &= \mathcal{H}^{11}_{eff}\mathcal{L}^{red}_{11} + \left(\mathcal{H}^{12}_{eff} + \mathcal{H}^{21}_{eff}\right)\mathcal{L}^{red}_{12} + \left(\mathcal{H}^{13}_{eff} + \mathcal{H}^{31}_{eff}\right)\mathcal{L}^{red}_{13} \\ &\quad + \mathcal{H}^{22}_{eff}\mathcal{L}^{red}_{22} + \left(\mathcal{H}^{23}_{eff} + \mathcal{H}^{32}_{eff}\right)\mathcal{L}^{red}_{23} + \mathcal{H}^{33}_{eff}\mathcal{L}^{red}_{33}. \end{aligned}\tag{4.42}$$

Then, the real part of hadronic tensor is symmetric whereas its imaginary part is anti-symmetric. Since the leptonic tensor is also symmetric. This leads to $\left(\mathcal{H}^{\mu\nu} + \mathcal{H}^{\nu\mu}\right)\mathcal{L}_{\mu\nu} = 2\mathfrak{Re}\mathcal{H}^{\mu\nu}\mathcal{L}_{\mu\nu}$ and consequently to:

$$\begin{aligned}\mathcal{H}^{ij}_{eff}\mathcal{L}^{red}_{ij} &= \mathcal{H}^{11}_{eff}\mathcal{L}^{red}_{11} + 2\mathfrak{Re}\mathcal{H}^{12}_{eff}\mathcal{L}^{red}_{12} + 2\mathfrak{Re}\mathcal{H}^{13}_{eff}\mathcal{L}^{red}_{13} \\ &\quad + \mathcal{H}^{22}_{eff}\mathcal{L}^{red}_{22} + 2\mathfrak{Re}\mathcal{H}^{23}_{eff}\mathcal{L}^{red}_{23} + \mathcal{H}^{33}_{eff}\mathcal{L}^{red}_{33}. \end{aligned}\tag{4.43}$$

Using the Eq. 4.34 and contracting, one obtains:

$$\frac{d^5\sigma}{dq^2\,(d\Omega_{\pi^\circ})_{lab}\,d\Omega^*_{e^+}} = \mathcal{H}^{ij}_{eff}\mathcal{L}^{red}_{ij} \tag{4.44}$$

$$\begin{aligned} &= 2e^2q^2 \left(\mathcal{H}^{11}_{eff} + \mathcal{H}^{22}_{eff} + \mathcal{H}^{33}_{eff}\right) \\ &\quad -8e^2|\overrightarrow{p}^*_{e^+}|^2 \left(\mathcal{H}^{11}_{eff} sin^2\theta^*_e cos^2\varphi^*_e + 2\mathfrak{Re}\mathcal{H}^{12}_{eff} sin^2\theta^*_e sin\varphi^*_e cos\varphi^*_e \right. \\ &\quad + 2\mathfrak{Re}\mathcal{H}^{13}_{eff} sin\theta^*_e cos\theta^*_e cos\varphi^*_e + \mathcal{H}^{22}_{eff} sin^2\theta^*_e sin^2\varphi^*_e \\ &\quad \left. + 2\mathfrak{Re}\mathcal{H}^{23}_{eff} sin\theta^*_e cos\theta^*_e sin\varphi^*_e + \mathcal{H}^{33}_{eff} cos^2\theta^*_e\right), \end{aligned}\tag{4.45}$$

where: $|\overrightarrow{p}^*_{e^+}|^2 = \frac{q^2}{4} - M_e^2$ and $e = -\sqrt{4\pi\alpha_{em}}$.

Replacing $cos^2\varphi = \frac{1+cos2\varphi}{2}$, $\sin^2\varphi = \frac{1-cos2\varphi}{2}$ and $sin\varphi cos\varphi = \frac{1}{2}sin2\varphi$:

$$\frac{d^5\sigma}{dq^2\,(d\Omega_{\pi^\circ})_{lab}\,d\Omega^*_{e^+}} = \mathcal{H}^{ij}_{eff}\mathcal{L}^{red}_{ij} \tag{4.46}$$

$$\begin{aligned} &= 2e^2q^2 \left(\mathcal{H}^{11}_{eff} + \mathcal{H}^{22}_{eff} + \mathcal{H}^{33}_{eff}\right) \\ &\quad -8e^2|\overrightarrow{p}^*_{e^+}|^2 \left(\frac{\mathcal{H}^{11}_{eff} + \mathcal{H}^{22}_{eff}}{2} sin^2\theta^*_e + \frac{\mathcal{H}^{11}_{eff} - \mathcal{H}^{22}_{eff}}{2} sin^2\theta^*_e cos2\varphi^*_e \right. \\ &\quad + \mathfrak{Re}\mathcal{H}^{12}_{eff} sin^2\theta^*_e sin2\varphi^*_e + 2\mathfrak{Re}\mathcal{H}^{13}_{eff} sin\theta^*_e cos\theta^*_e cos\varphi^*_e \\ &\quad \left. + 2\mathfrak{Re}\mathcal{H}^{23}_{eff} sin\theta^*_e cos\theta^*_e sin\varphi^*_e + \mathcal{H}^{33}_{eff} cos^2\theta^*_e\right). \end{aligned}\tag{4.47}$$

This expression is general and results on the particular exchange of the γ^* (spin 1) to electron-positron pair.

Numerical evaluation within this model and no polarization of the hadronic tensor values indicates that $\mathcal{H}^{12}_{eff}$ and $\mathcal{H}^{23}_{eff}$ are zero independently of the values of s, q^2 and θ_{π^0}. In conclusion, the five fold differential cross section depends on five kinematical variables (q^2, θ_{π^0}, φ_{π^0}, θ^*_e, φ^*_e) and four quantities ($\mathcal{H}^{11}_{eff}$, $\mathcal{H}^{22}_{eff}$, $\mathcal{H}^{33}_{eff}$, $\mathcal{H}^{13}_{eff}$).

4.2.3.3 Hadronic tensor extraction

The interest of extracting the hadronic tensors relies on the fact that they contain information on the proton structure. Starting from the 5-fold differential cross section (Eq. 4.44), one can see that fixing q^2 and Ω_{π^0}, the measurement of the positron or the electron distribution in the virtual photon rest frame would allow to access the hadronic tensors. Such a model as the advantage to be model independent.

Then in a model dependent way, one can go from this hadronic tensors to the form factors as shown in the following section.

4.2.3.4 Form factor extraction

From hadronic tensor to form factors

Assuming that the exchanged particles X_1 and X_2 are protons (Fig. 4.9(a) and 4.9(b)), the hadronic tensor can be expressed as follows:

$$\begin{aligned} \mathcal{H}^{\mu\nu} = & \quad \alpha^{\mu\nu} \quad |G_E|^2 + \beta^{\mu\nu}|G_M|^2 \\ & + \quad \gamma^{\mu\nu} \quad |G_E||G_M| cos\left(\varphi_E - \varphi_M\right) + \delta^{\mu\nu}|G_E||G_M| sin\left(\varphi_E - \varphi_M\right), \end{aligned} \tag{4.48}$$

or:

$$\mathcal{H}^{\mu\nu} = |G_M|^2 \left[\alpha^{\mu\nu} R^2 + \beta^{\mu\nu} + \gamma^{\mu\nu} R cos\left(\varphi_E - \varphi_M\right) + \delta^{\mu\nu} R sin\left(\varphi_E - \varphi_M\right)\right], \tag{4.49}$$

where $\alpha^{\mu\nu}$, $\beta^{\mu\nu}$, $\gamma^{\mu\nu}$ and $\delta^{\mu\nu}$ depend on q^2 and Ω_{π^0}. The form factors here only depend on q^2. In our model, studies based on numerical evaluations only showed that $\delta^{\mu\nu}$ factors are equal to zero implying that only the cosine of the phase difference $cos\left(\varphi_E - \varphi_M\right)$ can be accessed.

Observables

The main idea is to find observables leading to the extraction of information which is as much as possible unbiased . For that reason, we will only count on the shape and not on the normalization (no analytical expression has been derived) . In the real experiment, we will have counts distributed in a spectrum as $d^2N/d\Omega^*_{e^+}$ (with $d\Omega^*_{e^+} = dcos\theta^*_{e^+} d\varphi^*_{e^+}$) as a function of $\varphi^*_{e^+}$ and $\cos\theta^*_{e^+}$ (for Δq^2 and $\Delta\Omega_{\pi^0}$ intervals fixed).

One possibility is to extract the proton form factors directly from this 2D distribution. To avoid problems related to low or very low, one can also integrate over one more variable and obtain $dN/d\varphi^*_{e^+}$ or $dN/dcos\theta^*_{e^+}$.

Three cases are studied:

$$\begin{aligned} \frac{dN_1}{dcos\theta^*_{e^+}} &= L_{int} \int_{\Delta q^2} \int_{\Delta\Omega_{\pi^0}} \int_0^{2\pi} \frac{d^5\sigma}{dq^2 d\Omega_{\pi^0} dcos\theta^*_{e^+} d\varphi^*_{e^+}} d\varphi^*_{e^+} dq^2 d\Omega_{\pi^0}, \\ &= A\left[1 + Bcos^2\theta^*_{e^+}\right], \end{aligned} \tag{4.50}$$

$$\begin{aligned} \frac{dN_2}{d\varphi^*_{e^+}} &= L_{int} \int_{\Delta q^2} \int_{\Delta\Omega_{\pi^0}} \int_{-1}^{+1} \frac{d^5\sigma}{dq^2 d\Omega_{\pi^0} dcos\theta^*_{e^+} d\varphi^*_{e^+}} dcos\theta^*_{e^+} dq^2 d\Omega_{\pi^0}, \\ &= C\left[1 + Dcos2\varphi^*_{e^+}\right], \end{aligned} \tag{4.51}$$

$$\begin{aligned}\frac{dN_3}{d\varphi^*_{e^+}} &= L_{int}\int_{\Delta q^2}\int_{\Delta\Omega_{\pi^0}}\int_0^{+1}\frac{d^5\sigma}{dq^2 d\Omega_{\pi^0} dcos\theta^*_{e^+} d\varphi^*_{e^+}} dcos\theta^*_{e^+} dq^2 d\Omega_{\pi^0},\\ &= E\left[1 + F cos2\varphi^*_{e^+} + G cos\varphi^*_{e^+}\right], \end{aligned} \tag{4.52}$$

where

$$A = \int_{\Delta q^2}\int_{\Delta\Omega_{\pi^0}} 4\pi e^2 q^2 \left(\mathcal{H}^{11}_{eff} + \mathcal{H}^{22}_{eff} + \mathcal{H}^{33}_{eff}\right) - 8\pi e^2 |\overrightarrow{p}^*_{e^+}|^2 \left(\mathcal{H}^{11}_{eff} + \mathcal{H}^{22}_{eff}\right) dq^2 d\Omega_{\pi^0}, \tag{4.53}$$

$$B = \frac{\int_{\Delta q^2}\int_{\Delta\Omega_{\pi^0}} 8\pi e^2 |\overrightarrow{p}^*_{e^+}|^2 \left(\mathcal{H}^{11}_{eff} + \mathcal{H}^{22}_{eff} - 2\mathcal{H}^{33}_{eff}\right) dq^2 d\Omega_{\pi^0}}{\int_{\Delta q^2}\int_{\Delta\Omega_{\pi^0}} 4\pi e^2 q^2 \left(\mathcal{H}^{11}_{eff} + \mathcal{H}^{22}_{eff} + \mathcal{H}^{33}_{eff}\right) - 8\pi e^2 |\overrightarrow{p}^*_{e^+}|^2 \left(\mathcal{H}^{11}_{eff} + \mathcal{H}^{22}_{eff}\right) dq^2 d\Omega_{\pi^0}}, \tag{4.54}$$

$$C = \int_{\Delta q^2}\int_{\Delta\Omega_{\pi^0}} \left(4e^2 q^2 - \frac{16}{3} e^2 |\overrightarrow{p}^*_{e^+}|^2\right) \left(\mathcal{H}^{11}_{eff} + \mathcal{H}^{22}_{eff} + \mathcal{H}^{33}_{eff}\right) dq^2 d\Omega_{\pi^0}, \tag{4.55}$$

$$D = \frac{\int_{\Delta q^2}\int_{\Delta\Omega_{\pi^0}} \frac{16}{3} e^2 |\overrightarrow{p}^*_{e^+}|^2 \left(\mathcal{H}^{22}_{eff} - \mathcal{H}^{11}_{eff}\right) dq^2 d\Omega_{\pi^0}}{\int_{\Delta q^2}\int_{\Delta\Omega_{\pi^0}} \left(4e^2 q^2 - \frac{16}{3} e^2 |\overrightarrow{p}^*_{e^+}|^2\right) \left(\mathcal{H}^{11}_{eff} + \mathcal{H}^{22}_{eff} + \mathcal{H}^{33}_{eff}\right) dq^2 d\Omega_{\pi^0}}, \tag{4.56}$$

$$E = \int_{\Delta q^2}\int_{\Delta\Omega_{\pi^0}} \left(2e^2 q^2 - \frac{8}{3} e^2 |\overrightarrow{p}^*_{e^+}|^2\right) \left(\mathcal{H}^{11}_{eff} + \mathcal{H}^{22}_{eff} + \mathcal{H}^{33}_{eff}\right) dq^2 d\Omega_{\pi^0}, \tag{4.57}$$

$$F = \frac{\int_{\Delta q^2}\int_{\Delta\Omega_{\pi^0}} \frac{8}{3} e^2 |\overrightarrow{p}^*_{e^+}|^2 \left(\mathcal{H}^{22}_{eff} - H^{11}_{eff}\right) dq^2 d\Omega_{\pi^0}}{\int_{\Delta q^2}\int_{\Delta\Omega_{\pi^0}} \left(2e^2 q^2 - \frac{8}{3} e^2 |\overrightarrow{p}^*_{e^+}|^2\right) \left(\mathcal{H}^{11}_{eff} + \mathcal{H}^{22}_{eff} + \mathcal{H}^{33}_{eff}\right) dq^2 d\Omega_{\pi^0}} = D, \tag{4.58}$$

$$G = \frac{\int_{\Delta q^2}\int_{\Delta\Omega_{\pi^0}} -\frac{8}{3} e^2 |\overrightarrow{p}^*_{e^+}|^2 2\mathfrak{Re}\mathcal{H}^{13}_{eff} dq^2 d\Omega_{\pi^0}}{\int_{\Delta q^2}\int_{\Delta\Omega_{\pi^0}} \left(2e^2 q^2 - \frac{8}{3} e^2 |\overrightarrow{p}^*_{e^+}|^2\right) \left(\mathcal{H}^{11}_{eff} + \mathcal{H}^{22}_{eff} + \mathcal{H}^{33}_{eff}\right) dq^2 d\Omega_{\pi^0}}, \tag{4.59}$$

and $L_{int} = 2$ fb^{-1} is the integrated nominal luminosity of $\overline{\mathrm{P}}$ANDA . It is also worth noting that $N_1 = N_2$. $\frac{dN_2}{d\varphi^*_{e^+}}$ is obtained by integrating $cos\theta^*_{e^+}$ from -1 to 1 whereas $\frac{dN_3}{d\varphi^*_{e^+}}$ is obtained by integrating $cos\theta^*_{e^+}$ from 0 to 1. In the latter case, a $cos\varphi^*_{e^+}$ dependence appears.

From Eq. 4.50, 4.51 and 4.52 it is clear that the important observables for the proton form factor extraction will be B, D, F and G since they weight up the shape of the distributions in $cos\theta^*_{e^+}$, $cos2\varphi^*_{e^+}$ and $cos\varphi^*_{e^+}$. So, by measuring the shape of the angular distribution in $cos\theta^*_{e^+}$, and $\varphi^*_{e^+}$, the 4 observables will be determined and then related to the form factors. As these 4 quantities are simply related to $|G^p_E|$ and $|G^p_M|$ (Eq. 4.48 and since we have shown that in the case of unpolarized beam and target we are not sensitive to the sign of the phase difference and only 3 quantities are independent ($F = D$). Then, without knowing the normalization it is not possible to extract separately $|G^p_E|$ $|G^p_M|$ and the cosine of the phase difference $cos\left(\varphi_E - \varphi_M\right)$ but only the form factor ratio $R = |G^p_E|/|G^p_M|$ and $cos\left(\varphi_E - \varphi_M\right)$.

Since the proton form factors only depend on q^2, by fixing the q^2 interval, it is possible to determine the form factors using different Ω_{π^0} intervals. In this case, the extraction corresponding to each Ω_{π^0} interval must give the same result.

4.2.4 Constraint on the new calculation for $\overline{p}p \to \pi^\circ e^+e^-$

The main goal of the present model is to be as much as possible realistic. To do this, one needs to compare and constrain model with data. There are no available data for $\overline{p}p \to \pi^\circ\gamma^*$ but $\overline{p}p \to \pi^\circ\gamma$ was measured at Fermilab.

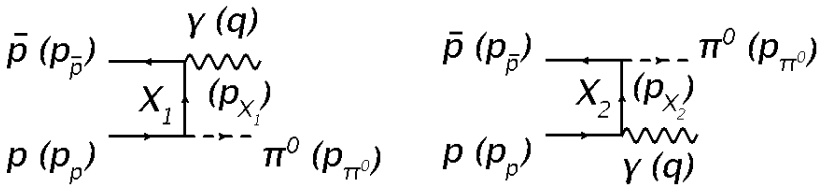

(a) (b)

Figure 4.10: $\overline{p}p \to \pi^\circ\gamma$ diagrams.

4.2.4.1 Calculation

This model is a direct extension of the $\overline{p}p \to \pi^\circ e^+e^-$ model. The amplitude $\mathcal{M} = \mathcal{M}_a + \mathcal{M}_b$ of the diagrams Fig. 4.10(a) and 4.10(b) and then the differential cross section were calculated in a similar way (J. Van de Wiele, [56]).

Amplitude

Starting from the Fig. 4.10(a), the exchanged nucleon four momentum p_{X_1} is:

$$p_{X_1} = p_p - p_{\pi^\circ}, \tag{4.60}$$

and the amplitude $\mathcal{M}_a$ is given by:

$$\mathcal{M}_a(\lambda, m_{\overline{p}}, m_p) = \overline{v}(m_{\overline{p}})\,\Gamma_a^\mu u(m_p)\,\varepsilon_\mu^*(\lambda), \tag{4.61}$$

$$\Gamma_a^\mu = V_{NN\gamma}^\mu i P_F\left(N, p_{X_1}\right) V_{NN\pi}. \tag{4.62}$$

Using the second diagram (Fig. 4.10(b)), the exchanged nucleon four momentum p_{X_2} is:

$$p_{X_2} = p_{\pi^\circ} - p_{\overline{p}}, \tag{4.63}$$

and the amplitude $\mathcal{M}_b$ is given by:

$$\mathcal{M}_b(\lambda, m_{\overline{p}}, m_p) = \overline{v}(m_{\overline{p}})\,\Gamma_b^\mu u(m_p)\,\varepsilon_\mu^*(\lambda), \tag{4.64}$$

$$\Gamma_b^\mu = V_{NN\pi} i P_F\left(N, p_{X_2}\right) V_{NN\gamma}^\mu. \tag{4.65}$$

Here, $\overline{v}$ and u are spinors, P_F is the nucleon propagator, $V_{NN\pi}$ is the pseudo-vector nucleon-nucleon-pion coupling and $V_{NN\gamma}^\mu$ is the nucleon-nucleon-photon coupling which contains the form factor dependence:

$$V_{NN\gamma}^\mu = -ie_p\left(F_1^p\gamma^\mu - i\frac{F_2^p}{2M_p}\sigma^{\mu\nu}q_\nu\right), \tag{4.66}$$

where $e_p = \sqrt{4\pi\alpha}$ is the proton charge, F_1^p and F_2^p are the Pauli and Dirac form factors. Also, for real photon $q^2 = 0$ therefore $F_1^p = F_1^p(0) = 1$ and $F_2^p = F_2^p(0) = \kappa^p$.

The amplitude of $\overline{p}p \to \pi^\circ\gamma$ taking into account both diagrams is then:

$$\mathcal{M}(\lambda, m_{\overline{p}}, m_p) = J_H^\mu(m_{\overline{p}}, m_p)\,\varepsilon_\mu^*(\lambda), \tag{4.67}$$

where

$$J_H^\mu(m_{\overline{p}}, m_p) = \overline{v}(m_{\overline{p}})\,\Gamma^\mu u(m_p), \tag{4.68}$$
$$\Gamma^\mu = \Gamma_a^\mu + \Gamma_b^\mu. \tag{4.69}$$

Differential cross section

The differential cross section of $\overline{p}p \to \pi^\circ\gamma$ is proportional to the amplitude squared $|\mathcal{M}|^2$:

$$|\mathcal{M}|^2 = \sum_{\lambda, m_{\overline{p}}, m_p} |\mathcal{M}(\lambda, m_{\overline{p}}, m_p)|^2, \tag{4.70}$$
$$= \mathcal{H}^{\mu\nu} \sum_\lambda \varepsilon_\mu^*(\lambda)\,\varepsilon_\nu(\lambda), \tag{4.71}$$
$$= -\mathcal{H}^{\mu\nu} g_{\mu\nu}, \tag{4.72}$$

where

$$\mathcal{H}^{\mu\nu} = \sum_{m_{\overline{p}}, m_p} J_H^\mu(m_{\overline{p}}, m_p)\, J_H^{\nu\,*}(m_{\overline{p}}, m_p), \tag{4.73}$$

and the Gauge invariance of the hadronic tensor gives

$$q_\mu \mathcal{H}^{\mu\nu} = \mathcal{H}^{\mu\nu} q_\nu = 0. \tag{4.74}$$

Going to the antiproton-proton center of mass with the Oz axis along the beam axis, the two fold differential cross section is:

$$\frac{d^2\sigma}{d\Omega_{\pi^\circ}} = \frac{(\hbar c)^2}{16\,(2\pi)^2\, s} \frac{|\overrightarrow{p}_{\pi^\circ}|}{|\overrightarrow{p}_{\overline{p}}|} \frac{|\mathcal{M}|^2}{4}. \tag{4.75}$$

At this point, one needs to compare the results for the $\overline{p}p \to \pi^\circ\gamma$ differential cross section to the data.

4.2.4.2 $\overline{p}p \to \pi^\circ\gamma$ data

In Ref. [44] are presented several differential cross sections of two-body neutral final states produced in antiproton-proton annihilation at Fermilab in the center of mass for the energy range $2.911 \leq \sqrt{s} \leq 3.686$ GeV.

The following data come from the E760 experiment at Fermilab and correspond to the annihilation channel $\overline{p}p \to \pi^\circ\gamma$. The differential cross sections $d\sigma/dcos\theta_\pi^*$ were determined at several energies with different luminosities and angular coverages. Table 4.2 presents the energies which were used in this part. One can see from this table that the angular coverage is very limited but also that the available energies are separated into two groups:

one where $2.911 \leq \sqrt{s} \leq 3.097$ GeV and another one where $3.527 \leq \sqrt{s} \leq 3.686$ GeV and nothing in between.

$\sqrt{s}$ (GeV)	$\int Ldt$ (nb^{-1})	$(cos\theta^*_\pi)_{min}$	$(cos\theta^*_\pi)_{max}$	$\sqrt{s}$ (GeV)	$\int Ldt$ (nb^{-1})	$(cos\theta^*_\pi)_{min}$	$(cos\theta^*_\pi)_{max}$
2.911	53.1	-0.475	+0.475	3.527	1016.4	-0.625	+0.625
2.950	197.5	-0.475	+0.475	3.556	1377.4	-0.625	+0.625
2.975	423.9	-0.475	+0.475	3.591	923.8	-0.625	+0.625
2.979	165.3	-0.475	+0.475	3.595	826.8	-0.625	+0.625
2.981	392.6	-0.475	+0.475	3.613	1167.2	-0.625	+0.625
2.985	200.2	-0.475	+0.475	3.616	1048.0	-0.625	+0.625
2.990	513.0	-0.475	+0.475	3.619	575.0	-0.625	+0.625
2.994	308.9	-0.475	+0.475	3.621	1216.4	-0.625	+0.625
3.005	171.0	-0.475	+0.475	3.686	994.6	-0.625	+0.625
3.050	53.6	-0.475	+0.475				
3.097	384.4	-0.525	+0.575				

Table 4.2: Summary of the energies, integrated luminosities and angular coverage for the $\overline{p}p \to \pi^\circ\gamma$ reaction.

Due to the small angular coverage of the data, to compare the model to the data, each set of data has been fitted with the polynomial function $a + bx^2 + cx^4$ where $x = cos\theta^*_{\pi^0}$ (going to the 6^{th} order was not helpful). These fits were then compared to the cross section calculations and it appeared that both model and data disagree by 3-4 orders of magnitude. Therefore, a form factor on the propagator F was introduced to take into account the off-shellness of the proton.

4.2.4.3 Form factor on the propagator

The form factor on the propagator squared F^2 was obtained dividing the fit by the calculation (see Eq. 4.75). Fig. 4.11 displays as an example the results for $\sqrt{s} = 3.005$ GeV and it shows a $cos\theta^*_{\pi^0}$ dependence. Then, looking to other $\sqrt{s}$ values, it appears that F^2 also depends on $\sqrt{s}$.

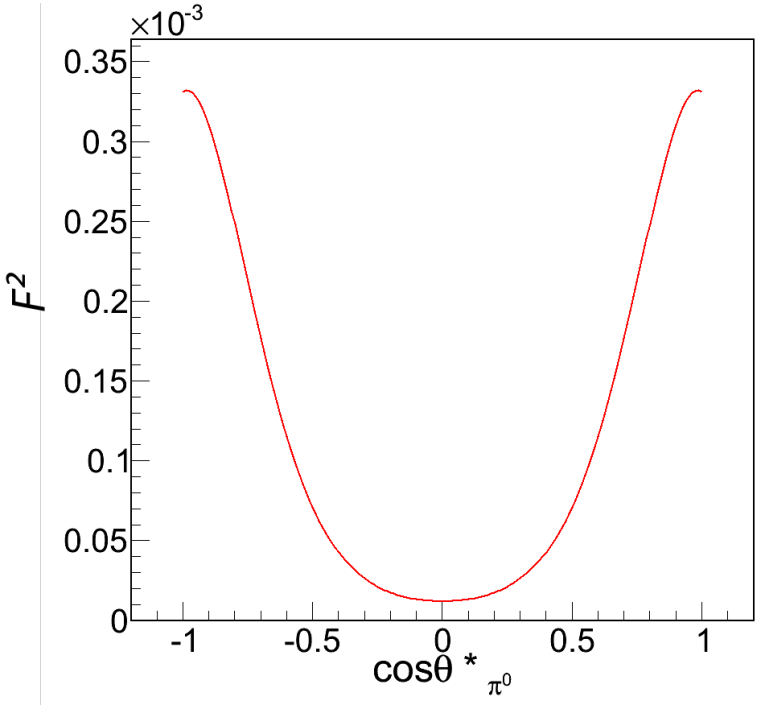

Figure 4.11: Form factor on propagator squared obtained by dividing the fit ($a + bx^2 + cx^4$ where $x = cos\theta^*_{\pi^0}$) of the data by the calculation. Picture shows F^2 as a function of $cos\theta^*_{\pi^0}$ at $\sqrt{s} = 3.005$ GeV.

The following form of the form factor on the propagator squared F^2 is assumed. This form respects Gauge invariance and is symmetric with respect to the proton and antiproton vertex.

$$F^2\left(\sqrt{s}, p_{X_1}.p_{X_2}\right) = \left[\frac{\lambda^2\left(\sqrt{s}, p_{X_1}.p_{X_2}\right) - M_p^2}{\lambda^2\left(\sqrt{s}, p_{X_1}.p_{X_2}\right) - p_{X_1}^2}\right]^2 \left[\frac{\lambda^2\left(\sqrt{s}, p_{X_1}.p_{X_2}\right) - M_p^2}{\lambda^2\left(\sqrt{s}, p_{X_1}.p_{X_2}\right) - p_{X_2}^2}\right]^2 \quad (4.76)$$

where p_{X_i} are the four-momentum transfers (see Fig. 4.10) and $\lambda\left(\sqrt{s}, p_{X_1}.p_{X_2}\right)$ is a parameter in GeV/c^2. For $p_{X_i}^2 \gg \lambda^2\left(\sqrt{s}, p_{X_1}.p_{X_2}\right)$, the amplitude is highly suppressed. Furthermore when q^2 is close to s i.e.: when the proton is almost on-shell, F^2 tends to 1 while when q^2 tends to 0, $F^2 \gg 1$.

We want to have a simple parametrization of $\lambda\left(\sqrt{s}, p_{X_1}.p_{X_2}\right)$ depending on the system energy $\sqrt{s}$ and on the $p_{X_1}.p_{X_2}$ (containing $\theta^*_{\pi^0}$ dependence) to be able to extrapolate λ at other energies. $\lambda\left(\sqrt{s}, p_{X_1}.p_{X_2}\right)$ is expressed as follows:

$$\lambda(\sqrt{s}, p_{X_1}.p_{X_2}) = P_1(\sqrt{s}) \; + \; P_2(\sqrt{s})\; p_{X_1}.p_{X_2}\; 10^{-2} \; + \; P_3(\sqrt{s})\; (p_{X_1}.p_{X_2})^2\; 10^{-4} \quad (4.77)$$

where P_i are linear function of $\sqrt{s}$. The Fig. 4.12 shows the results obtained for the P_i.

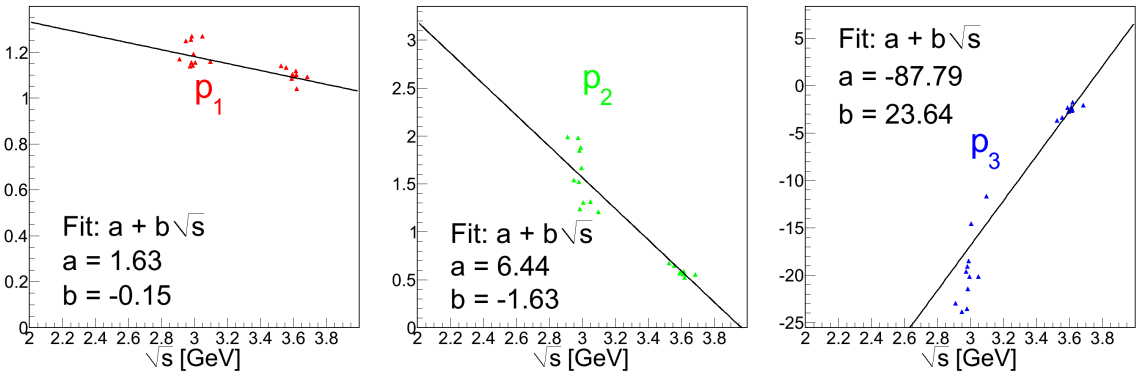

(a) P_1 (b) P_2 (c) P_3

Figure 4.12: λ parameters: results for P_1, P_2 and P_3.

λ was extrapolated at several kinetic energies including at $T = 1$ GeV ($\sqrt{s} = 2.32$ GeV). A small $cos\theta^{*}_{\pi^0}$ dependence (lower than 3%) was observed. Therefore λ was considered only as a function of $\sqrt{s}$ leading to $\lambda(\sqrt{s} = 2.323) = P_1(\sqrt{s} = 2.323) = 1.25$ GeV/c^2 at $T = 1$ GeV ($\sqrt{s} = 2.323$ GeV).

4.2.4.4 Results

The Fig. 4.13 shows the calculation including the form factor on the propagator of the $\overline{p}p \to \pi^{\circ}\gamma$ differential cross section at 4 different center of mass energies. The calculation now reproduces the Fermilab data.

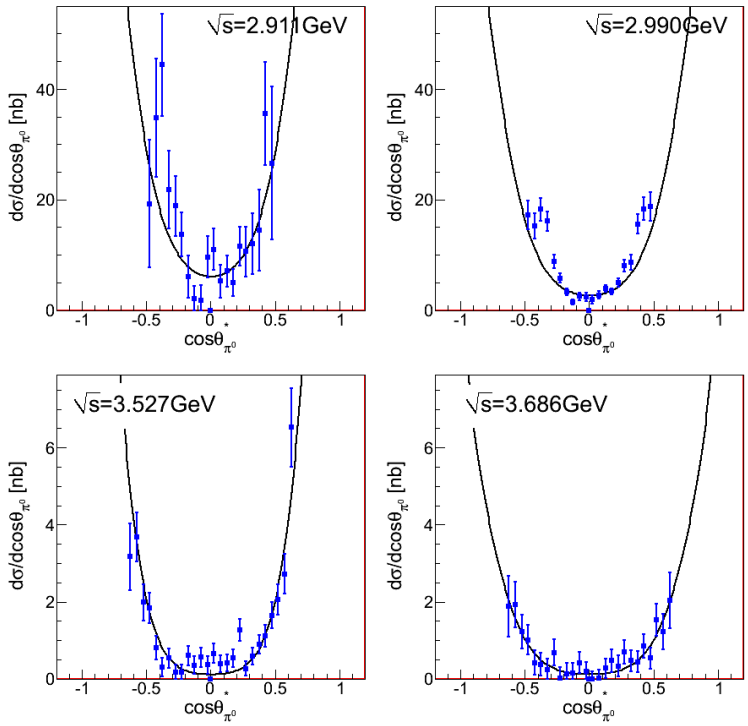

Figure 4.13: Differential cross section $\mathrm{d}\sigma/\mathrm{dcos}\theta^*_{\pi^0}$ in nb for $\overline{p}p \to \pi^\circ\gamma$ at different center of mass system energies calculated with the model including the form factor on propagator and compared to the data.

Fig. 4.14 displays the $\overline{p}p \to \pi^\circ e^+ e^-$ differential cross section $\frac{d\sigma}{dq^2}$ at $T_{\overline{p}} = 1$ GeV. This differential cross section includes the form factor on the propagator. The differential cross section still present the ρ, ω and ϕ meson resonances. Comparing Fig. 4.14 to Fig. 4.8, one notes that the new calculation gives a differential cross section 2-3 orders of magnitude lower than the previous one-nucleon exchange model.

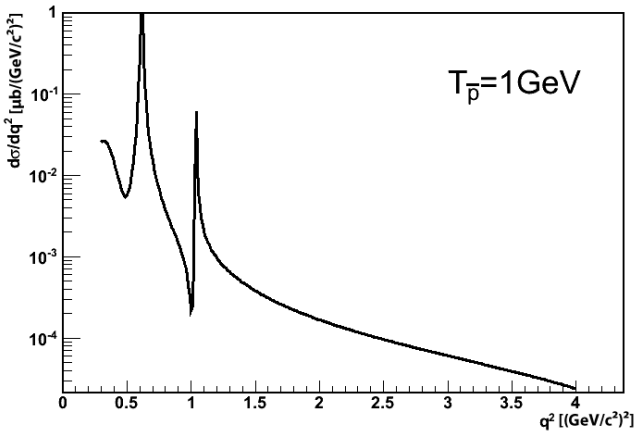

Figure 4.14: $\overline{p}p \to \pi^\circ e^+ e^-$ differential cross section $\frac{d\sigma}{dq^2}$ from the new calculation at $T_{\overline{p}} = 1$ GeV.

Chapter 5

Feasibility study of $\overline{p}p \to \pi^{\circ}e^{+}e^{-}$

In this chapter, I show the feasibility studies for the proton electromagnetic form factor measurements in the unphysical region using the reaction $\overline{p}p \to \pi^{\circ}e^{+}e^{-}$. I start by presenting our regions of interest and the detector resolution. Then, to estimate the background rejection, an over simplified model for the dominant hadronic background channel was used and the corresponding rejection factors determined for several q^2. The signal contamination is obtained using realistic counting rates as well as the acceptance and efficiency. Finally, I will show the results for the extraction of the hadronic tensors and for the extraction of the electromagnetic proton form factors out of the $e^{+}e^{-}$ angular distribution.

5.1 Preliminary studies

5.1.1 Regions of interest

Since the main goal of studying the $\overline{p}p \to \pi^{\circ}e^{+}e^{-}$ is to determine the form factor below threshold, it would be interesting to have one case close to the threshold where the Iachello parametrization is smooth and structureless and one case in the mesonic region. As it was shown in the previous section 4.2.3.4, to extract the proton form factors it is necessary to define both q^2 and θ_{π^0} intervals.Therefore, $\overline{p}p \to \pi^{\circ}e^{+}e^{-}$ cross section dependences on the beam kinetic energy, on q^2 and on θ_{π^0} were studied and are presented in the following.

5.1.1.1 Beam kinetic energy and q^2 dependence

To have a more precise idea about the beam kinetic energy dependence of the differential cross section, the $\overline{p}p \to \pi^{\circ}e^{+}e^{-}$ differential cross section $d\sigma/dq^2$ is plotted as a function of q^2 for a broad range of antiproton beam kinetic energies (from 1 to 13 GeV) in Fig. 5.1.

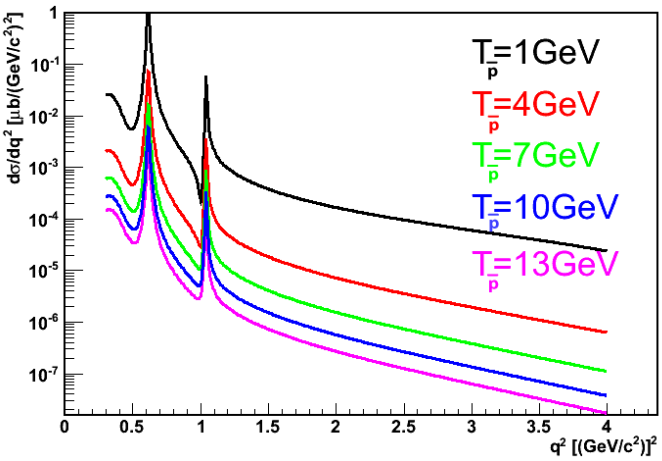

Figure 5.1: $\overline{p}p \to \pi^\circ e^+ e^-$ differential cross section $d\sigma/dq^2$ as a function of q^2 for several beam kinetic energies.

The figure shows a decrease of the differential cross section when the beam kinetic energy increases. Therefore, the lowest kinetic energy ($T_{\overline{p}} = 1$ GeV) is selected.

According to Iachello parametrization, the differential cross section shows fast variations in the region of the vector meson poles and a smooth decrease for higher values. We therefore chose two q^2 intervals: $q^2 = 0.605 \pm 0.005$ $(\mathrm{GeV/c^2})^2$ and $q^2 = 2 \pm 0.125$ $(\mathrm{GeV/c^2})^2$. The width of the former interval is chosen as close as possible to the experimental resolution to have a chance to scan the ω resonance and the width of the latter is chosen to be large enough to avoid low counting rate. Both intervals were optimized to have the best precision on the form factors.

5.1.1.2 θ_{π^0} dependence

As example, Fig. 5.2 shows the number of counts as a function of θ_{π^0} in lab ($\Delta\theta_{\pi^0} = 1^\circ$) at $T_{\overline{p}} = 1$ GeV and both q^2 intervals assuming an integrated luminosity of 2 fb^{-1}. Distributions show a maximum at around 25°.

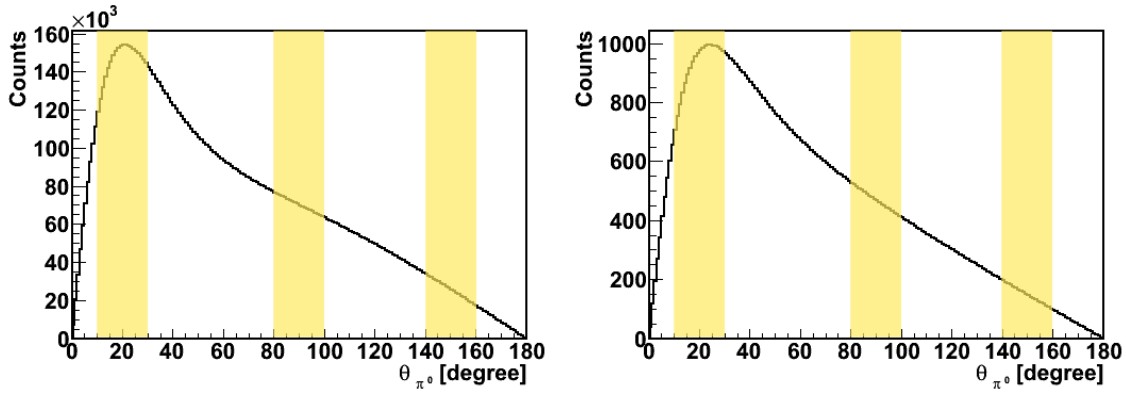

(a) $q^2 = 0.605 \pm 0.005$ (GeV/c^2)^2 (b) $q^2 = 2 \pm 0.125$ (GeV/c^2)^2

Figure 5.2: Counts as a function of θ_{π^0} ($\Delta\theta_{\pi^0} = 1°$) at $T_{\overline{p}} = 1$ GeV for $q^2 = 0.605 \pm 0.005$ (GeV/c^2)^2 (5.2(a)) and $q^2 = 2 \pm 0.125$ (GeV/c^2)^2 (5.2(b)). The integrated luminosity is 2 fb^{-1}. Yellow bands represent the selected angular regions.

As expected, at $q^2 = 0.605 \pm 0.005$ (GeV/c^2)^2 close to the ω resonance, see Fig. 5.2(a), the number of counts is relatively high. In Fig. 5.2(b) which corresponds to $q^2 = 2 \pm 0.125$ (GeV/c^2)^2, the number of counts is quite low, especially at backward θ_{π^0} angles. It is important to remember that this number of counts is theoretical and that later on one has to take into account the acceptance and the detector efficiency which will further decrease it. In case of low counting rate, this can be problematic for the proton form factor extraction.

Three angular regions (yellow bands in Fig. 5.2) were chosen large enough to avoid low counting rate: $10° < \theta_{\pi^0} < 30°$, $80° < \theta_{\pi^0} < 100°$ and $140° < \theta_{\pi^0} < 160°$ for both q^2 intervals.

5.1.1.3 Hadronic tensor dependences on q^2 and θ_{π^0}

As shown in Chapter 4.2.3.2, the effective hadronic tensors $\mathcal{H}^{11}_{eff}$, $\mathcal{H}^{22}_{eff}$, $\mathcal{H}^{33}_{eff}$, $\mathcal{H}^{13}_{eff}$ (see Eq. 4.40) are the relevant quantities. They are displayed at $T_{\overline{p}} = 1$ GeV for $q^2 = 0.605 \pm 0.005$ (GeV/c^2)^2 and $q^2 = 2 \pm 0.125$ (GeV/c^2)^2 in Fig. 5.3 and Fig. 5.4 respectively. The first observation is that for both figures all the hadronic tensors tend to zero while increasing the θ_{π° angle. This implies (see Eq. 4.44) that the sensitivity to the effective hadronic tensors becomes weaker and weaker and that the counting rate will be lower at backward π° angles. The second point is that for both q^2 intervals, only $\mathcal{H}^{13}_{eff}$ reaches negative values. Finally comparing both q^2 intervals, one can note that the hadronic tensors corresponding to $q^2 = 0.605 \pm 0.005$ (GeV/c^2)^2 are around 5-6 order of magnitude higher than for $q^2 = 2 \pm 0.125$ (GeV/c^2)^2.

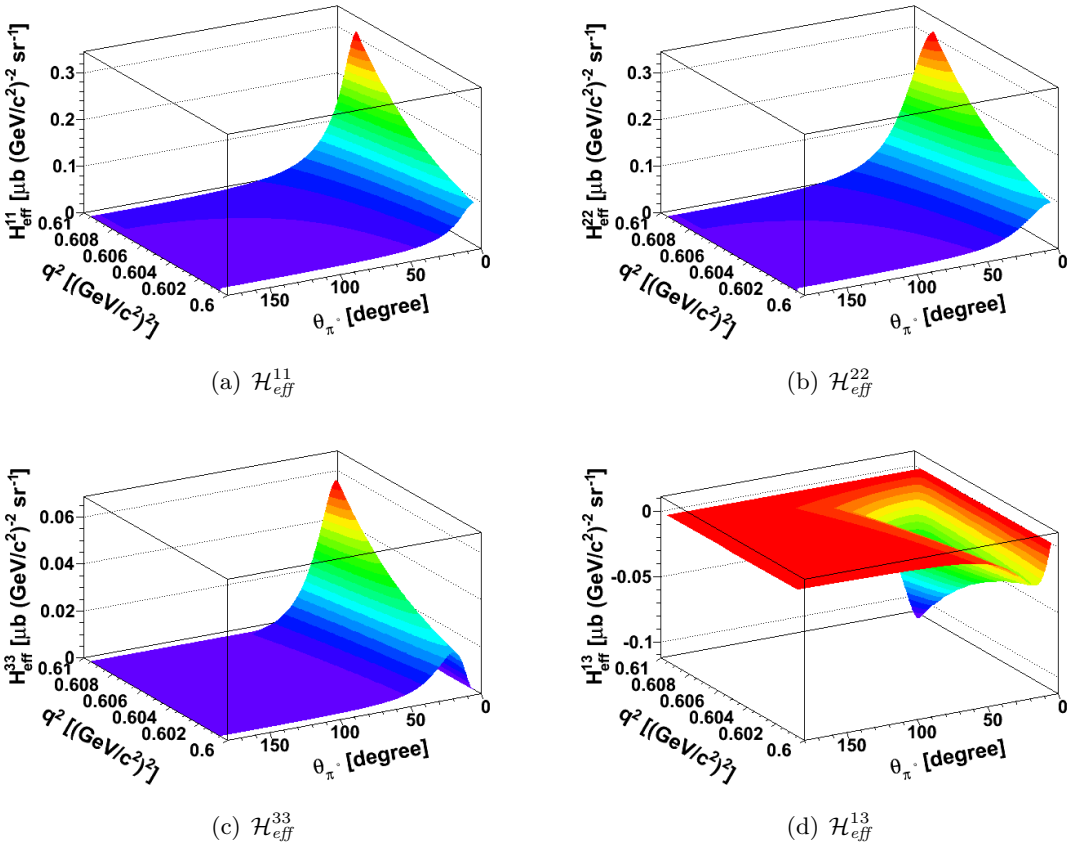

(a) $\mathcal{H}^{11}_{eff}$ (b) $\mathcal{H}^{22}_{eff}$

(c) $\mathcal{H}^{33}_{eff}$ (d) $\mathcal{H}^{13}_{eff}$

Figure 5.3: Effective hadronic tensor dependences on q^2 around 0.605 $(\mathrm{GeV/c^2})^2$ and θ_{π^0} at $T_{\overline{p}} = 1$ GeV.

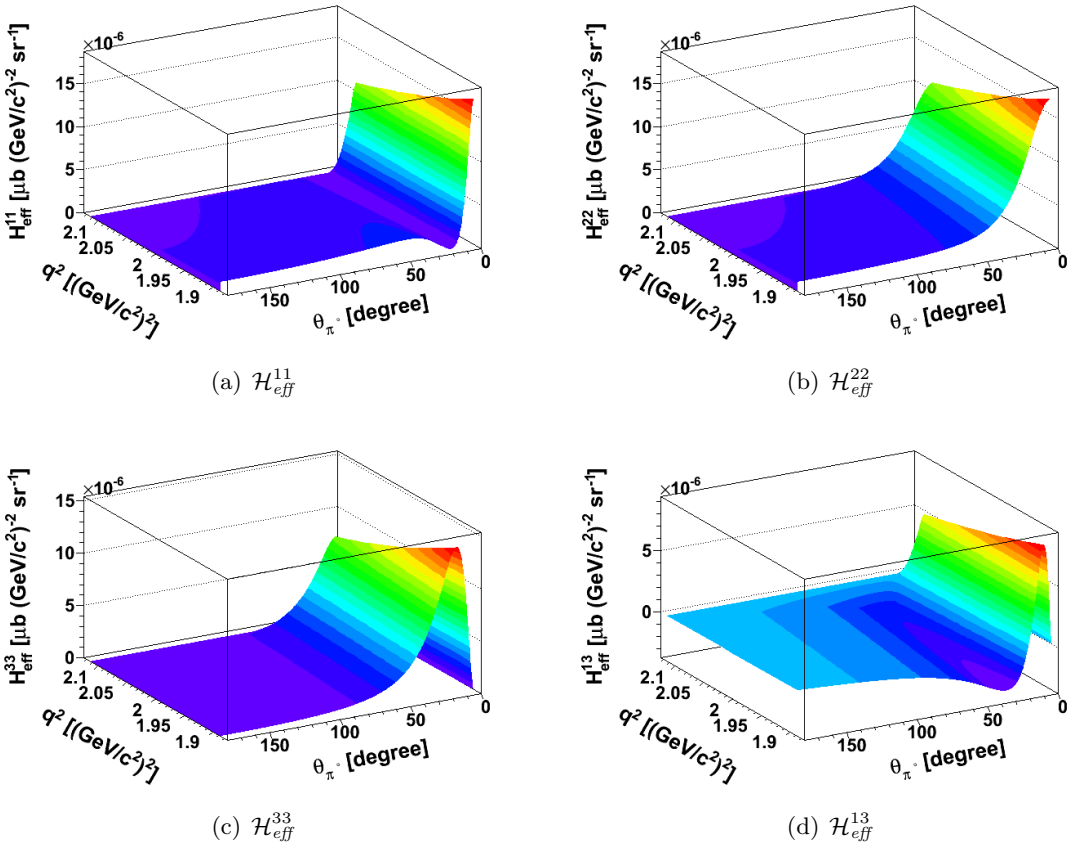

(a) $\mathcal{H}^{11}_{eff}$ (b) $\mathcal{H}^{22}_{eff}$

(c) $\mathcal{H}^{33}_{eff}$ (d) $\mathcal{H}^{13}_{eff}$

Figure 5.4: Effective hadronic tensor dependences on q^2 around 2 $(\mathrm{GeV/c^2})^2$ and θ_{π^0} at $T_{\overline{p}} = 1$ GeV.

5.1.2 Detector resolution

The resolution effect on q^2 value was studied within the BABAR framework by T. Liu [60]. The BABAR framework (detailled in [9]) contains the $\overline{\mathrm{P}}$ANDA geometry. Simulations are done as follows. First, the propagation of the particles through the detector is based on the GEANT4 code. Then, the information on hits and energy losses are digitalized into a response of the different detectors using a model for electronic noise. Finally, physical quantities such as momentum (tracking), energy deposit (electromagnetic calorimeter), energy loss to path length ratio (dE/dx) and Cherenkov angles (light cone in the DIRC) are reconstructed.

The reaction $\overline{p}p \to \pi^\circ e^+ e^-$ was simulated with a phase space model for $T_{\overline{p}} = 1$ GeV [61]. Two q^2 values were studied: $q^2 = 0.6 \pm 0.001$ $(\mathrm{GeV/c^2})^2$ and $q^2 = 2.0 \pm 0.003$ $(\mathrm{GeV/c^2})^2$. For the reconstruction, the detector acceptance, the tracking efficiency and the resolution effects were taken into account.

To be reconstructed, an event must fulfil the following requirements:

- at least one positively charged particle c^+,
- at least one negatively charged particle c^-,
- at least two photons detected in the calorimeter each of them having an energy greater than 0.03 GeV,
- at least one π° which is reconstructed from two of the above photons and must have a mass between 0.115 and 0.15 GeV/c^2,
- energy and momentum conservation for all triplet (π°, c^+, c^-) combinations (only the best one is kept).

If one of the previous conditions is not fulfilled the event is not reconstructed. Having $\overline{p}p \to \pi^\circ c^+ c^-$ reconstructed events, the particle identification (PID) for electrons and positrons is applied to obtain $\overline{p}p \to \pi^\circ e^+ e^-$ reconstructed events. The very tight (VT) cut was used. The VT cut means that one requires that the probability of the positively (negatively) charged particle to be a positron (electron) is at least 99.8%. This combined probability takes into account all the information from the MVD, the central tracker, the DIRC, the EMC and the muon detector.

Two methods were tested to calculate q^2: one is the invariant mass squared of the lepton pair and the other one is the missing mass squared of $\overline{p}p \to \pi^0 X$. Results showed that the reconstructed q^2 distributions are few times larger than the interval used for these studies and these distributions therefore show pure resolution effects. Also, the first method to calculate q^2 gave better results.

The effect of the kinematic fit method was studied in this context. The kinematical fit method is a constrained fit which takes into account energy and momentum conservation.

Results before (pink) and after (blue) kinematic fit are displayed in Fig. 5.5 ($T_{\overline{p}} = 1$ GeV and $q^2 = 0.6 \pm 0.001$ (GeV/c^2)^2) and Fig. 5.6 ($T_{\overline{p}} = 1$ GeV and $q^2 = 2.0 \pm 0.003$ (GeV/c^2)^2). From these figures, the resolution improvement due to the kinematic fit is clearly visible and brings the resolution below 0.8% at $q^2 = 0.6$ (GeV/c^2)^2 and below 0.5% at $q^2 = 2.0$ (GeV/c^2)^2. Hence this result validates a posteriori the choice $q^2 = 0.605 \pm 0.005$ (GeV/c^2)^2 previously presented. Furthermore, within the achieved resolution about 0.005 (GeV/c^2)^2, $\Delta M^2 = 2M\Delta M$ is $\sim$ 0.012 (GeV/c^2)^2 at $q^2 = 0.605 \pm 0.005$ (GeV/c^2)^2. Comparing this value to the $\Delta M^2 = 0.022$ (GeV/c^2)^2 obtained by the parametrization, it is possible to describe the ω resonance. Results also show that the resolution is almost independent of the π^0 angle in the laboratory.

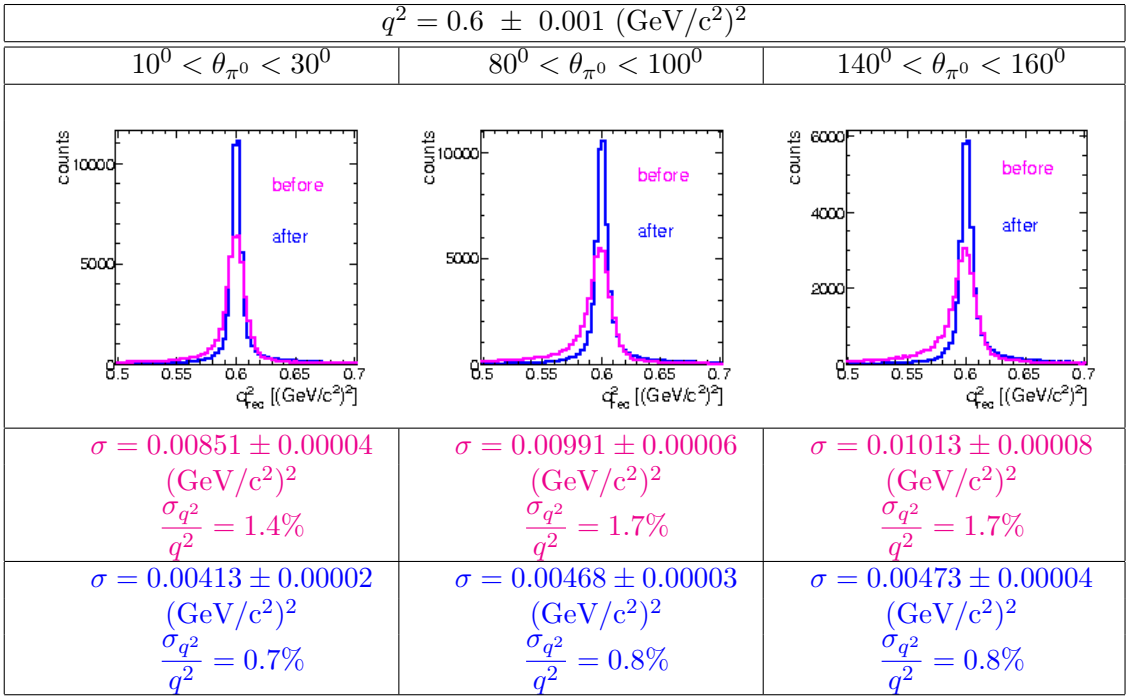

Figure 5.5: The q^2 distribution around $q^2 = 0.6$ (GeV/c^2)^2 as a function of the π^0 polar angle in Lab. obtained from reconstructed events, before kinematic fit (pink histograms) and after kinematic fit (blue histograms) from [60].

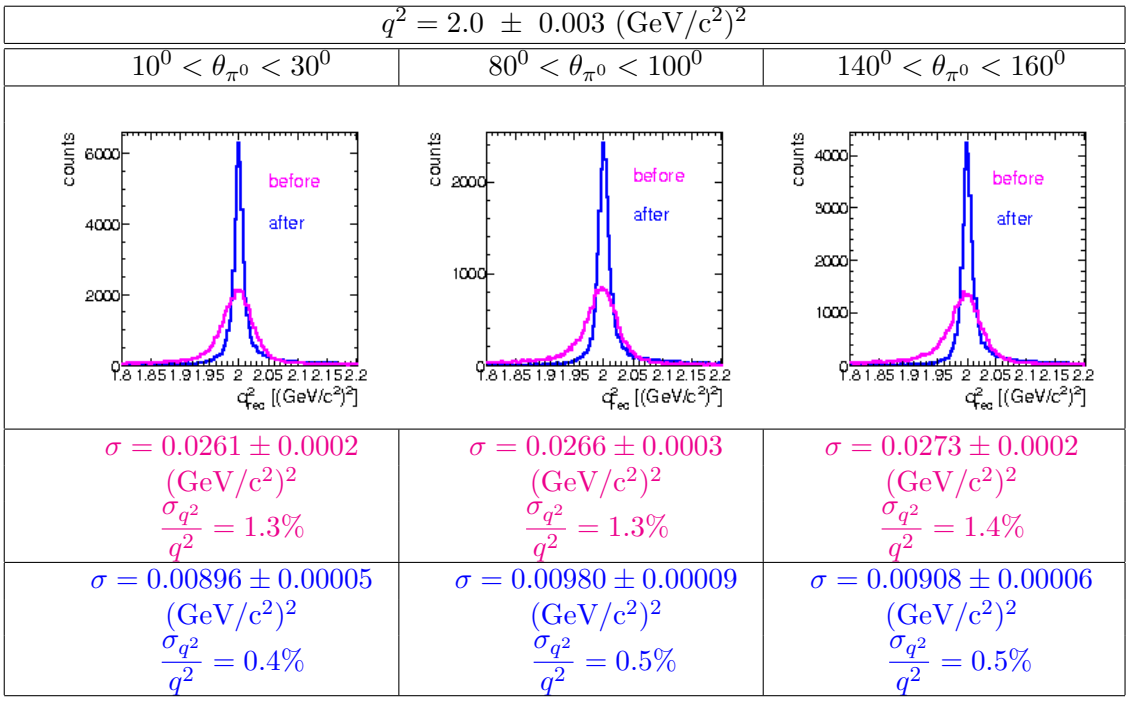

Figure 5.6: The q^2 distribution around $q^2 = 2.0$ (GeV/c^2)^2 as a function of the π^0 polar angle in Lab. obtained from reconstructed events, before kinematic fit (pink histograms) and after kinematic fit (blue histograms) from [60].

5.2 Background studies

Up to now, we have worked assuming that $\overline{p}p \to \pi^\circ e^+ e^-$ can be easily identified and is background free. In this paragraph we will investigate the role of hadronic reactions which might lead to a pollution of the signal and try to see if additional cuts are needed. An over simplified model for the dominant hadronic background channel was used and the corresponding rejection factors determined for several q^2 and θ_{π^0}.

5.2.1 Possible background channels

Reactions involving two or more hadrons in the final channel constitute an important background for the measurement of channels with creation of lepton pair. The background channels with the highest cross section are listed below:

- $\overline{p}p \to n\pi^+ n\pi^- m\pi^\circ$ where $n \geq 2$ and $m \geq 0$
- $\overline{p}p \to \pi^+\pi^-\omega$
- $\overline{p}p \to \pi^+\pi^-\rho^\circ$
- $\overline{p}p \to \pi^\circ\pi^\circ$
- $\overline{p}p \to \pi^+\pi^-\pi^\circ$
- $\overline{p}p \to K^+K^-\pi^\circ$

$\overline{\text{P}}$ANDA detector being almost a 4π detector, $\overline{p}p \to n\pi^+ n\pi^- m\pi^\circ$ where $n \geq 2$ and $m \geq 0$ will be easily removed counting the charged particles which are detected. ω and ρ° decay into pions at 100%, $\overline{p}p \to \pi^+\pi^-\omega$ and $\overline{p}p \to \pi^+\pi^-\rho^\circ$ can be removed using the same technique. One can also calculate the missing mass squared $M_X^2 = (p_{\overline{p}} + p_p - p_{\pi^+} - p_{\pi^-})^2$.

For the $\overline{p}p \to \pi^0\pi^0$ channel, e^+e^- pairs are produced after the conversion of the photons from the π° or from the Dalitz decay of one (or both) π° with probability 10^{-2} (10^{-4}). In this case, the final state of the background channel is the same as for the signal. Using the invariant mass of the lepton pair and the missing mass, this background channel can suppressed efficiently.

The main backgrounds are expected to be $\overline{p}p \to \pi^0\pi^0$, $\overline{p}p \to \pi^\circ\pi^+\pi^-$ and $\overline{p}p \to K^+K^-\pi^\circ$. For the channel $\overline{p}p \to K^+K^-\pi^\circ$, the probability of misidentification of a kaon as an electron is lower than the misidentification of a pion as an electron and the kinematical constraints are more efficient due to their larger mass. Therefore, the most difficult channel to suppress is expected to be $\overline{p}p \to \pi^\circ\pi^+\pi^-$.

5.2.2 The $\overline{p}p \to \pi^\circ\pi^+\pi^-$ channel

5.2.2.1 $\overline{p}p \to \pi^\circ\pi^+\pi^-$ description

S. Ong and J. Van de Wiele built a model for $\overline{p}p \to \pi^\circ\pi^+\pi^-$ based on effective lagragian calculation. As there is only one existing measurement of $M_{\pi^+\pi^-}$ invariant mass spectrum decomposed in different channels (NR 3π, $\pi\rho \to 3\pi$, $\pi f_2 \to 3\pi$) at 1.43 GeV/c [62].The model involves only one nucleon exchange. The included diagrams are displayed in Fig.

5.7. It is valid at low antiproton beam kinetic energy ($1 < T_{\overline{p}} < 2$ GeV). In case of higher transfer, one needs to add the N^* exchange and the Δ exchange (not done here due to the lack of data). To summary, a first approximation model has been developed and tuned to reproduce the data (total cross section, resonances). Once the $\overline{\mathrm{P}}$ANDA experiment running, one must measure the $\overline{p}p \rightarrow \pi^{\circ}\pi^{+}\pi^{-}$ reaction and improve or develop new model.

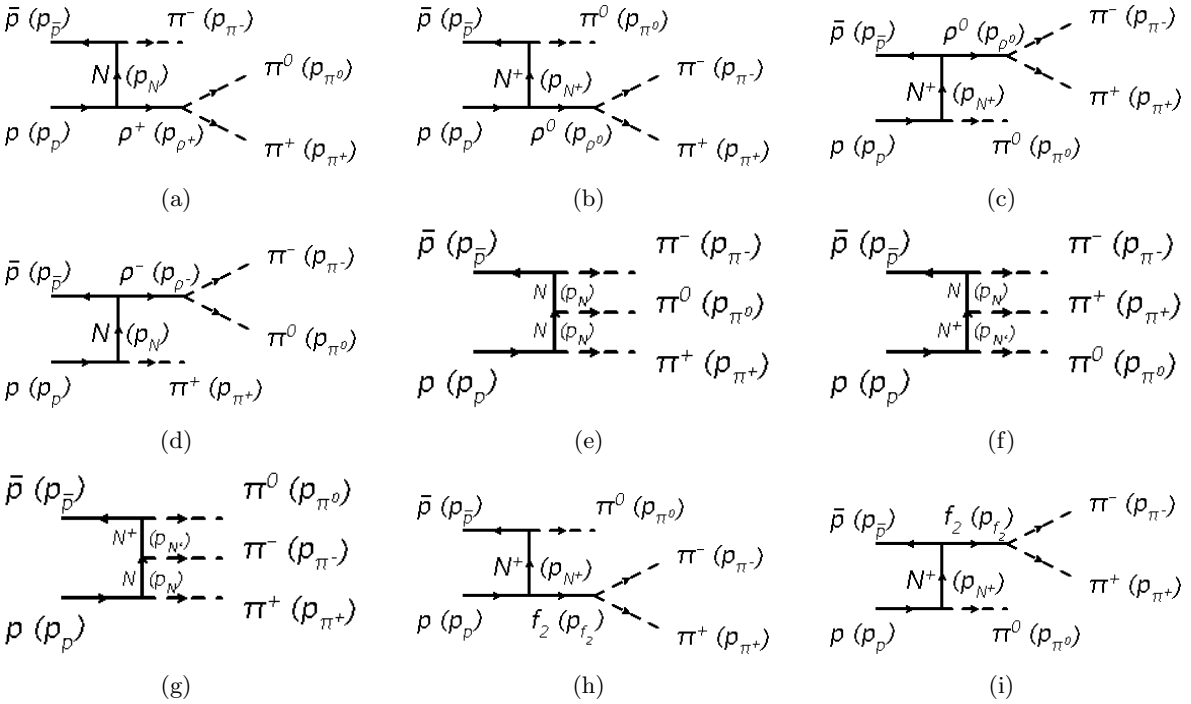

Figure 5.7: Included diagrams for the $\overline{p}p \rightarrow \pi^{\circ}\pi^{+}\pi^{-}$ calculation. N stands for neutron and N^{+} for proton.

Fig. 5.8 shows the comparison of the calculation with data for 1.43 GeV/c antiproton momentum ($T_{\overline{p}} = 0.772$ GeV). The contributions of the dominant channels are well reproduced. Furthermore, one can clearly observed the ρ and f_2 resonances.

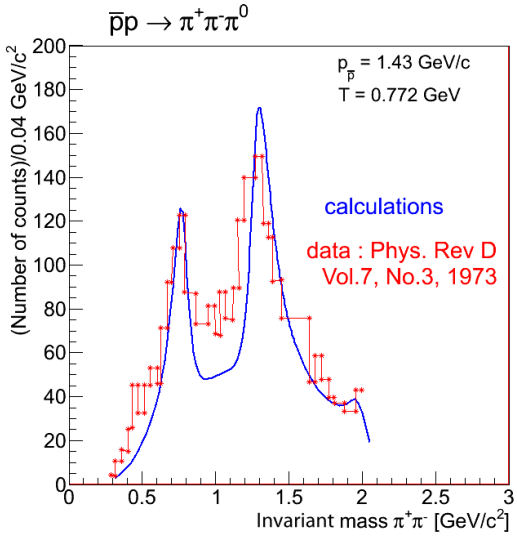

Figure 5.8: $\overline{p}p \to \pi^\circ\pi^+\pi^-$ calculation compared to CERN data from [62] for 1.43 GeV/c antiproton momentum. The different structures of this invariant mass spectrum are well reproduced. The ρ and f_2 resonances are visible.

5.2.2.2 $\overline{p}p \to \pi^\circ\pi^+\pi^-$ suppression

The $\overline{p}p \to \pi^\circ\pi^+\pi^-$ suppression was studied within the BABAR framework in collaboration with M. Sudoł [61].

The reaction $\overline{p}p \to \pi^\circ\pi^+\pi^-$ was simulated with a phase space model at $T_{\overline{p}} = 1$ GeV, two q^2 values ($q^2 = 0.605\pm0.005$ (GeV/c^2)^2 and $q^2 = 2.0\pm0.125$ (GeV/c^2)^2) and three angular ranges ($10^\circ < \theta_{\pi^0} < 30^\circ$, $80^\circ < \theta_{\pi^0} < 100^\circ$ and $140^\circ < \theta_{\pi^0} < 160^\circ$) as for the signal. Here q^2 is defined as the invariant mass squared of the two charged pions: $q^2 = (p_{\pi^+} + p_{\pi^-})^2$. Being five fold differential, the background suppression factor matrices will therefore be model independent. For each case, 10^8 events were generated.

To be reconstructed, an event must fulfil the following requirements:

- at least one positively charged particle c^+,
- at least one negatively charged particle c^-,
- at least two photons detected in the calorimeter each of them having an energy greater than 0.03 GeV,
- at least one π° which is reconstructed from two of the above photons and must have a mass between 0.115 and 0.15 GeV/c^2,
- energy and momentum conservation for all triplet (π°, c^+, c^-) combinations (only the best one is kept).

From these reconstructed events, we need to know how much will be misidentified as $\overline{p}p \to \pi^\circ e^+ e^-$. For this we used the very tight cut as for the signal (see 5.1.2).

Similarly to the $\overline{p}p \rightarrow e^+e^-$ study, one can also use the confidence level associated to the kinematical fit to suppress the background. The confidence level is based on the reaction vertex and on the kinematical fit which includes 4-momentum constraint. The confidence level (CL), directly derived from the $\mathcal{X}^2$ value obtained after the kinematical fit, is calculated for both $\pi^0e^+e^-$ and $\pi^0\pi^+\pi^-$ hypothesis.

Assuming that the PID and the CL cuts are not correlated [8], the total background supression factor can be calculated as the PID supression factor multiplied by the CL supression factor. Four cuts have been considered:

1. Cut1 = $CL_{\pi^\circ e^+e^-} > CL_{\pi^\circ\pi^+\pi^-}$,
2. Cut2 = $CL_{\pi^\circ e^+e^-} > 10CL_{\pi^\circ\pi^+\pi^-}$,
3. Cut3 = $CL_{\pi^\circ e^+e^-} > 10CL_{\pi^\circ\pi^+\pi^-}$ && $CL_{\pi^\circ e^+e^-} > 0.001$,
4. Cut4 = $CL_{\pi^\circ e^+e^-} > 10CL_{\pi^\circ\pi^+\pi^-}$ && $CL_{\pi^\circ e^+e^-} > 0.1$.

Tab. 5.1 and Tab. 5.2 present the background suppression factors for the PID and the four cuts at $T_{\overline{p}} = 1$ GeV, $q^2 = 0.605 \pm 0.005$ (GeV/c^2)^2 and $q^2 = 2 \pm 0.125$ (GeV/c^2)^2 respectively. To get a meaningful estimate of the suppression factor, which is not biased by the low statistics, values were averaged and calculated for two angular bins: $80° < \theta^*_{e^+} < 90°$ and $140° < \theta^*_{e^+} < 150°$.

		$q^2 = 0.605 \pm 0.005$ (GeV/c^2)^2		
		$10° < \theta_{\pi^0} < 30°$	$80° < \theta_{\pi^0} < 100°$	$140° < \theta_{\pi^0} < 160°$
PID cut	$80° < \theta^*_{e^+} < 90°$	$4.1\ 10^{-5}$	$9.6\ 10^{-6}$	$1.2\ 10^{-6}$
	$140° < \theta^*_{e^+} < 150°$	$4.9\ 10^{-6}$	$2.7\ 10^{-7}$	$2.3\ 10^{-7}$
Cut1	$80° < \theta^*_{e^+} < 90°$	$1.5\ 10^{-2}$	$1.6\ 10^{-1}$	$1.5\ 10^{-1}$
	$140° < \theta^*_{e^+} < 150°$	$2.1\ 10^{-3}$	$4.4\ 10^{-2}$	$7.3\ 10^{-2}$
Cut2	$80° < \theta^*_{e^+} < 90°$	$4.0\ 10^{-3}$	$1.5\ 10^{-2}$	$1.1\ 10^{-2}$
	$140° < \theta^*_{e^+} < 150°$	$1.5\ 10^{-3}$	$9.3\ 10^{-3}$	$3.3\ 10^{-2}$
Cut3	$80° < \theta^*_{e^+} < 90°$	$1.8\ 10^{-3}$	$9.0\ 10^{-3}$	$3.5\ 10^{-3}$
	$140° < \theta^*_{e^+} < 150°$	$2.2\ 10^{-4}$	$2.5\ 10^{-3}$	$1.5\ 10^{-2}$
Cut4	$80° < \theta^*_{e^+} < 90°$	$9.1\ 10^{-4}$	$4.5\ 10^{-3}$	$3.7\ 10^{-4}$
	$140° < \theta^*_{e^+} < 150°$	$7.3\ 10^{-5}$	$5.9\ 10^{-4}$	$5.3\ 10^{-3}$
PID cut + Cut1	$80° < \theta^*_{e^+} < 90°$	$6.1\ 10^{-7}$	$1.5\ 10^{-6}$	$1.8\ 10^{-7}$
	$140° < \theta^*_{e^+} < 150°$	$1.0\ 10^{-8}$	$1.2\ 10^{-8}$	$1.7\ 10^{-8}$
PID cut + Cut4	$80° < \theta^*_{e^+} < 90°$	$3.7\ 10^{-8}$	$4.3\ 10^{-8}$	$4.4\ 10^{-10}$
	$140° < \theta^*_{e^+} < 150°$	$3.6\ 10^{-10}$	$1.6\ 10^{-10}$	$1.9\ 10^{-9}$

Table 5.1: PID and CL suppression factors at $q^2 = 0.605 \pm 0.005$ (GeV/c^2)^2 are summarized in this table for two $\theta^*_{e^+}$ intervals. As explained in the text, the different lines correspond to different cuts.

		$q^2 = 2 \pm 0.125$ (GeV/c^2)^2		
		$10^\circ < \theta_{\pi^0} < 30^\circ$	$80^\circ < \theta_{\pi^0} < 100^\circ$	$140^\circ < \theta_{\pi^0} < 160^\circ$
PID cut	$80^\circ < \theta^*_{e^+} < 90^\circ$	$3.2\ 10^{-6}$	$7.0\ 10^{-7}$	$3.7\ 10^{-7}$
	$140^\circ < \theta^*_{e^+} < 150^\circ$	$2.6\ 10^{-7}$	$2.0\ 10^{-7}$	$2.1\ 10^{-7}$
Cut1	$80^\circ < \theta^*_{e^+} < 90^\circ$	$2.2\ 10^{-2}$	$1.4\ 10^{-1}$	$1.9\ 10^{-1}$
	$140^\circ < \theta^*_{e^+} < 150^\circ$	$2.8\ 10^{-2}$	$1.3\ 10^{-2}$	$9.2\ 10^{-2}$
Cut2	$80^\circ < \theta^*_{e^+} < 90^\circ$	$9.2\ 10^{-3}$	$1.2\ 10^{-2}$	$9.2\ 10^{-3}$
	$140^\circ < \theta^*_{e^+} < 150^\circ$	$7.5\ 10^{-3}$	$1.1\ 10^{-2}$	$1.7\ 10^{-2}$
Cut3	$80^\circ < \theta^*_{e^+} < 90^\circ$	$4.6\ 10^{-3}$	$6.7\ 10^{-3}$	$3.2\ 10^{-3}$
	$140^\circ < \theta^*_{e^+} < 150^\circ$	$3.6\ 10^{-3}$	$5.8\ 10^{-3}$	$7.6\ 10^{-3}$
Cut4	$80^\circ < \theta^*_{e^+} < 90^\circ$	$1.9\ 10^{-3}$	$3.1\ 10^{-3}$	$3.3\ 10^{-4}$
	$140^\circ < \theta^*_{e^+} < 150^\circ$	$1.8\ 10^{-3}$	$2.9\ 10^{-3}$	$2.7\ 10^{-3}$
PID cut + Cut1	$80^\circ < \theta^*_{e^+} < 90^\circ$	$7.0\ 10^{-8}$	$9.8\ 10^{-8}$	$7.0\ 10^{-8}$
	$140^\circ < \theta^*_{e^+} < 150^\circ$	$7.3\ 10^{-9}$	$2.6\ 10^{-9}$	$1.9\ 10^{-8}$
PID cut + Cut4	$80^\circ < \theta^*_{e^+} < 90^\circ$	$6.1\ 10^{-9}$	$2.2\ 10^{-9}$	$1.2\ 10^{-10}$
	$140^\circ < \theta^*_{e^+} < 150^\circ$	$4.7\ 10^{-10}$	$5.8\ 10^{-10}$	$5.7\ 10^{-10}$

Table 5.2: PID and CL suppression factors at $q^2 = 2 \pm 0.125$ (GeV/c^2)^2 are summarized in this table for two $\theta^*_{e^+}$ intervals. As explained in the text, the different lines correspond to different cuts.

Combining the PID cut with the Cut4, a 10^{-8} to 10^{-10} background suppression factor is reached at $q^2 = 0.605 \pm 0.005$ (GeV/c^2)^2 while at $q^2 = 2 \pm 0.125$ (GeV/c^2)^2 a 10^{-9} to 10^{-10} background suppression factor is obtained. It still remain to determine the effects of these cuts on the signal and on the proton electromagnetic form factor extraction.

5.3 Signal studies

Since the background cross section as well as the rejection factors are known, it is possible knowing the signal efficiency to determine the signal contamination corresponding to each of the previous cuts in order to choose the best one. Then the hadronic tensors and the proton electromagnetic form factors are extracted. Finally results are presented.

5.3.1 Signal contamination

The signal contamination S_C is the ratio of the number of background events after cuts to the number of signal events after the same cuts

$$S_C = \frac{\sigma_B}{\sigma_S}\frac{\epsilon_B}{\epsilon_S}, \tag{5.1}$$

where σ_B and σ_S are the background and signal cross section respectively, ϵ_B is the background suppression factor and ϵ_S the signal acceptance and efficiency. Cross section ratios at $T_{\overline{p}} = 1$ GeV and both q^2 are first presented. Then signal acceptance and efficiencies are determined. Finally signal contaminations are shown.

5.3.1.1 Background to signal differential cross section ratio

The $\overline{p}p \to \pi^\circ\pi^+\pi^-$ five fold differential cross section was extrapolated at $T_{\overline{p}} = 1$ GeV. It was integrated for the same intervals as for the signal. The background to signal cross

section ratio (σ_B/σ_S) is defined by

$$\frac{\sigma_B}{\sigma_S} = \frac{\int_{\Delta q^2}\int_{\Delta\Omega_{\pi^\circ}}\int_{\Delta\Omega_{\pi^+}{}^*} \frac{d^5\sigma}{dq^2 d\Omega_{\pi^\circ} d\Omega_{\pi^+}{}^*} dq^2 d\Omega_{\pi^\circ} d\Omega_{\pi^+}{}^*}{\int_{\Delta q^2}\int_{\Delta\Omega_{\pi^\circ}}\int_{\Delta\Omega_{e^+}{}^*} \frac{d^5\sigma}{dq^2 d\Omega_{\pi^\circ} d\Omega_{e^+}{}^*} dq^2 d\Omega_{\pi^\circ} d\Omega_{e^+}{}^*}. \tag{5.2}$$

Fig. 5.9 and 5.10 display the background to signal ratio (σ_B/σ_S). Here we used 10° bins for θ^* and φ^*.

In Fig. 5.9 (corresponding to $q^2 = 0.605 \pm 0.005$ (GeV/c^2)^2), the ratio goes from 10^3 up to 2 10^4. With the exception of the first and last θ^* bins, the ratio stays however below a few 10^3.

In Fig. 5.10 (corresponding to $q^2 = 2 \pm 0.125$ (GeV/c^2)^2),the ratio goes from 10^6 up to few 10^7. With the exception of the first and last θ^* bins, the ratio stays however below 2 10^7.

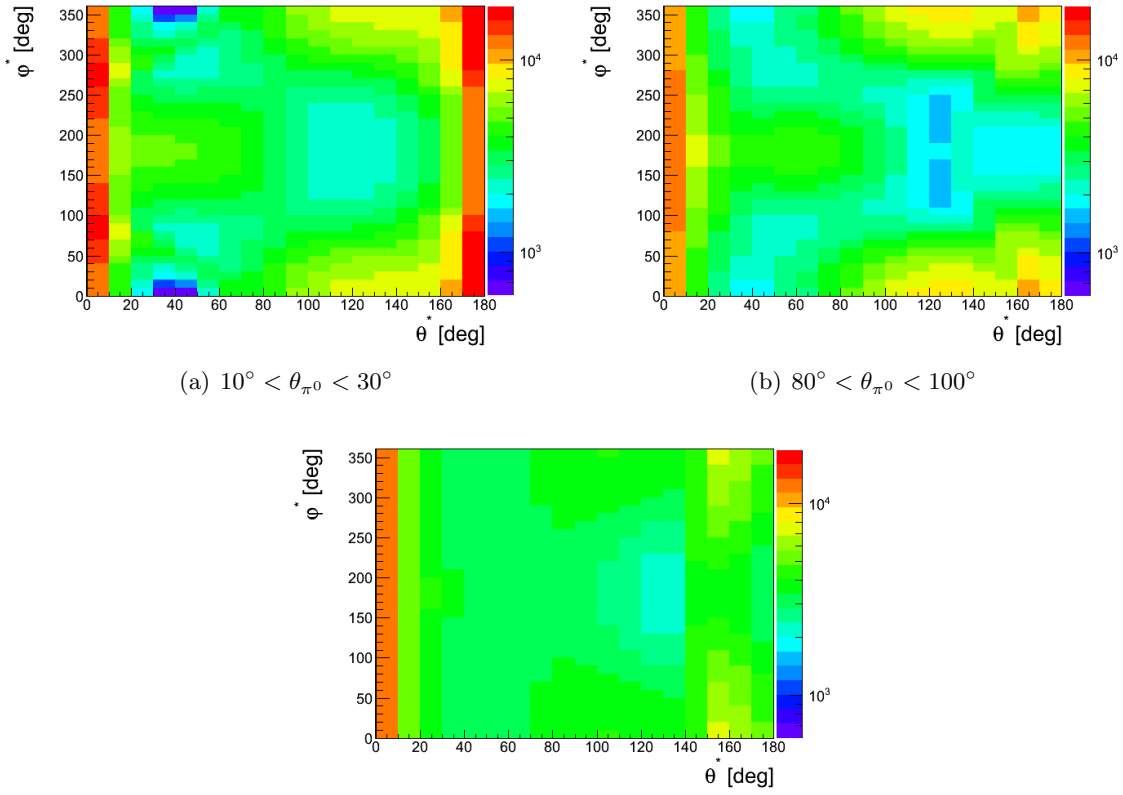

(a) $10^\circ < \theta_{\pi^0} < 30^\circ$

(b) $80^\circ < \theta_{\pi^0} < 100^\circ$

(c) $140^\circ < \theta_{\pi^0} < 160^\circ$

Figure 5.9: Background to signal ratio at $q^2 = 0.605 \pm 0.005$ (GeV/c^2)^2 (10° bins for θ^* and φ^*). For most of the angular range the ratio stays below a few 10^3.

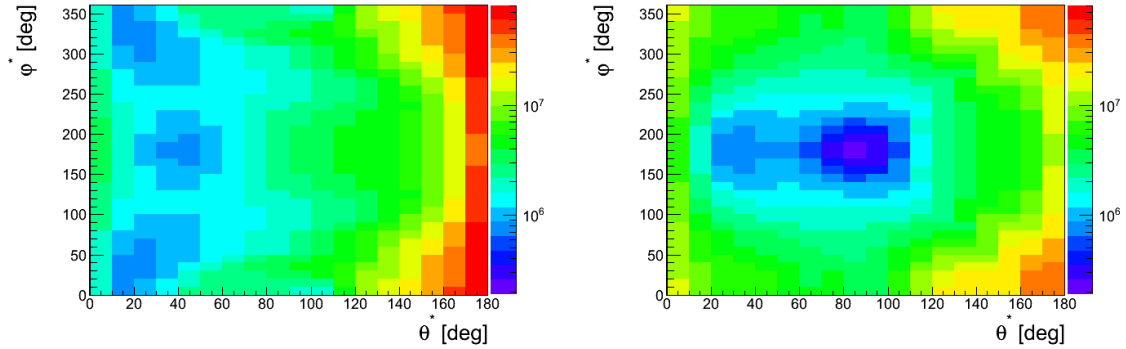

(a) $10^\circ < \theta_{\pi^0} < 30^\circ$

(b) $80^\circ < \theta_{\pi^0} < 100^\circ$

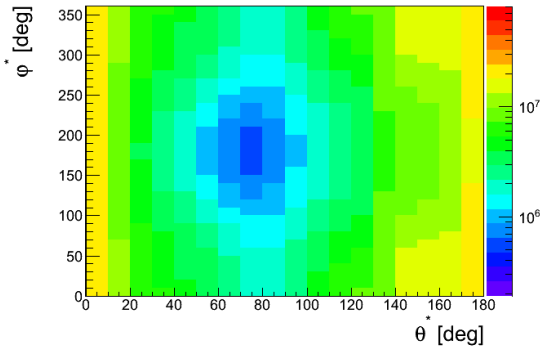

(c) $140^\circ < \theta_{\pi^0} < 160^\circ$

Figure 5.10: Background to signal ratio at $q^2 = 2 \pm 0.125$ $(\mathrm{GeV/c^2})^2$ (10° bins for θ^* and φ^*). For most of the angular range the ratio stays below 2 10^7.

Tables 5.3 and 5.4 summarize the averaged background to signal cross section ratio values at $T_{\bar{p}} = 1$ GeV, $q^2 = 0.605 \pm 0.005$ $(\mathrm{GeV/c^2})^2$ and $q^2 = 2 \pm 0.125$ $(\mathrm{GeV/c^2})^2$ respectively for two selected $\theta^*_{e^+}$ intervals.

		$q^2 = 0.605 \pm 0.005$ $(\mathrm{GeV/c^2})^2$		
		$10^\circ < \theta_{\pi^0} < 30^\circ$	$80^\circ < \theta_{\pi^0} < 100^\circ$	$140^\circ < \theta_{\pi^0} < 160^\circ$
σ_B/σ_S	$80^\circ < \theta^*_{e^+} < 90^\circ$	5 10^3	5 10^3	4 10^3
	$140^\circ < \theta^*_{e^+} < 150^\circ$	8 10^3	8 10^3	5 10^3

Table 5.3: Background to signal cross section ratio at $q^2 = 0.605 \pm 0.005$ $(\mathrm{GeV/c^2})^2$ for two $\theta^*_{e^+}$ intervals.

		$q^2 = 2 \pm 0.125$ $(\mathrm{GeV/c^2})^2$		
		$10^\circ < \theta_{\pi^0} < 30^\circ$	$80^\circ < \theta_{\pi^0} < 100^\circ$	$140^\circ < \theta_{\pi^0} < 160^\circ$
σ_B/σ_S	$80^\circ < \theta^*_{e^+} < 90^\circ$	3 10^6	4 10^6	2 10^6
	$140^\circ < \theta^*_{e^+} < 150^\circ$	2 10^7	2 10^7	2 10^7

Table 5.4: Background to signal cross section ratio at $q^2 = 2 \pm 0.125$ $(\mathrm{GeV/c^2})^2$ for two $\theta^*_{e^+}$ intervals.

5.3.1.2 Signal acceptance and efficiency

Behind the term acceptance and efficiency, three main effects are included: the detector acceptance which corresponds to the detector geometry, the reconstruction efficiency which depends on the detector capability to reconstruct an event $\overline{p}p \to \pi^{\circ}c^{+}c^{-}$ and the identification efficiency of positrons and electrons.

Like in the detector resolution part, the acceptance and the efficiency were determined within the BABAR framework. The reaction $\overline{p}p \to \pi^{\circ}e^{+}e^{-}$ was generated in phase space [61] for ${\theta_{e^+}}^*$ and ${\varphi_{e^+}}^*$ at fixed q^2 and $\Omega_{\pi^{\circ}}$ intervals. Being five fold differential, the acceptance and efficiency matrices will therefore be model independent. The events are then reconstructed using the very tight (VT) cut for the particle identification. The VT cut means that one requires that the probability of the positively (negatively) charged particle to be an positron (electron) is 99.8%. 10^6 events were generated at $T_{\overline{p}} = 1$ GeV for each of the following cases (where θ_{π^0} is in the laboratory):

- $q^2 = 2 \pm 0.125$ $(\mathrm{GeV/c^2})^2$
  - $10^{\circ} < \theta_{\pi^0} < 30^{\circ}$
  - $80^{\circ} < \theta_{\pi^0} < 100^{\circ}$
  - $140^{\circ} < \theta_{\pi^0} < 160^{\circ}$
- $q^2 = 0.605 \pm 0.005$ $(\mathrm{GeV/c^2})^2$
  - $10^{\circ} < \theta_{\pi^0} < 30^{\circ}$
  - $80^{\circ} < \theta_{\pi^0} < 100^{\circ}$
  - $140^{\circ} < \theta_{\pi^0} < 160^{\circ}$

The matrices of acceptance and efficiency were determined at $T_{\overline{p}} = 1$ GeV, $q^2 = 0.605 \pm 0.005$ $(\mathrm{GeV/c^2})^2$ and $q^2 = 2 \pm 0.125$ $(\mathrm{GeV/c^2})^2$ respectively for 5 cases:

1. PID
2. PID + Cut1 = PID && $CL_{\pi^{\circ}e^+e^-} > CL_{\pi^{\circ}\pi^+\pi^-}$
3. PID + Cut2 = PID && $CL_{\pi^{\circ}e^+e^-} > 10CL_{\pi^{\circ}\pi^+\pi^-}$
4. PID + Cut3 = PID && $CL_{\pi^{\circ}e^+e^-} > 10CL_{\pi^{\circ}\pi^+\pi^-}$ && $CL_{\pi^{\circ}e^+e^-} > 0.001$
5. PID + Cut4 = PID && $CL_{\pi^{\circ}e^+e^-} > 10CL_{\pi^{\circ}\pi^+\pi^-}$ && $CL_{\pi^{\circ}e^+e^-} > 0.1$

The acceptance and efficiency matrices were determined for all 5 cases previously defined in the virtual photon rest frame (with 10° bins for ${\theta_{e^+}}^*$ and ${\varphi_{e^+}}^*$) since the model gives the differential cross section in this specific frame. The acceptance and efficiency is the ratio of the reconstructed to generated events. The Fig. 5.11(a) and 5.11(b) display using the PID cut only the case $q^2 = 2 \pm 0.125$ $(\mathrm{GeV/c^2})^2$ and $10^{\circ} < \theta_{\pi^0} < 30^{\circ}$ in the virtual photon rest frame and also in the laboratory frame to have a better understanding of the shape of the acceptance and efficiency. Fig. 5.11(b) clearly shows the effect of the target pipe, see green color at ($\theta_{e^+} = 90^{\circ}$, $\varphi_{e^+} = 90^{\circ}$) and ($\theta_{e^+} = 90^{\circ}$, $\varphi_{e^+} = 270^{\circ}$). The purple color for $160^{\circ} < \theta_{e^+} < 180^{\circ}$ is due to the loss of positron since there are no detectors in this

region. All matrices using the PID only are available in the appendix A for both frames. The main point is that for the case $q^2 = 0.605 \pm 0.005$ $(\mathrm{GeV/c^2})^2$, the acceptance and efficiency goes roughly from 0.40 to 0.20 over the whole $\theta_{\pi^{\circ}}$ range $[0°; 180°]$. For the case $q^2 = 2 \pm 0.125$ $(\mathrm{GeV/c^2})^2$ the acceptance and efficiency goes roughly from 0.55 to 0.30. These matrices are used later on for the hadronic tensor and the form factor extractions.

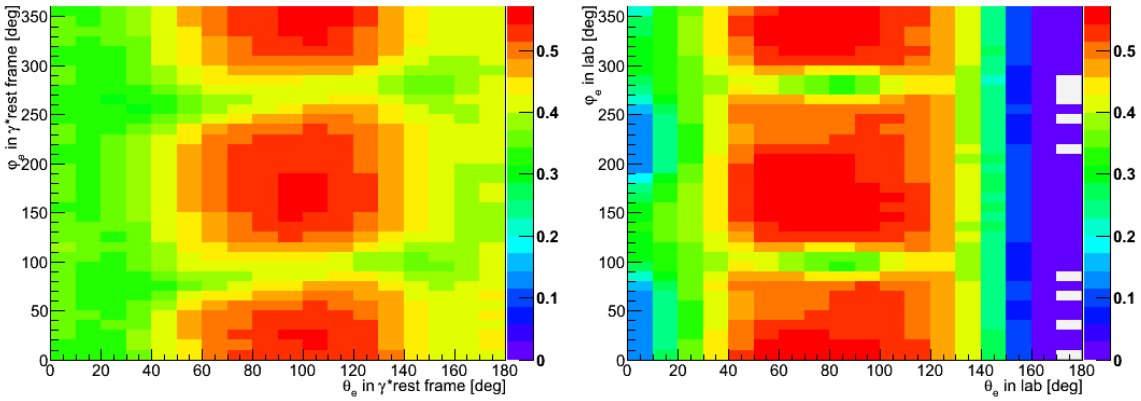

(a) $\gamma*$ rest frame (b) laboratory frame

Figure 5.11: Signal acceptance and efficiency matrices (PID only) for $q^2 = 2 \pm 0.125$ $(\mathrm{GeV/c^2})^2$ and $10° < \theta_{\pi^0} < 30°$ (with 10° bins for $\theta_{e^+}{}^*$ and $\varphi_{e^+}{}^*$).

The precision of the acceptance and efficiency matrices depends on the number of generated events in each finite volume element. With 10° bins for $\theta_{e^+}{}^*$ and $\varphi_{e^+}{}^*$ and 10^6 generated events, one has on average 1500 events per finite volume element leading to a fluctuation of 2.5%. To have smaller fluctuations, one simply needs to generate more events. The acceptance and efficiency matrices will at the end be however limited by the statistics. we assume no error on the acceptance and efficiency matrices. As an example, Tab. 5.5 presents the number of generated events in 4 finite volume elements at $q^2 = 2 \pm 0.125$ $(\mathrm{GeV/c^2})^2$ and $10° < \theta_{\pi^0} < 30°$.

		$\theta_{e^+}{}^*$ [deg]	
		$30 - 40$	$150 - 160$
$\varphi_{e^+}{}^*$ [deg]	$280 - 290$	N=1387 $\sqrt{N}/N$=2.7%	N=1028 $\sqrt{N}/N$=3.1%
	$80 - 90$	N=1346 $\sqrt{N}/N$=2.7%	N=995 $\sqrt{N}/N$=3.2%

Table 5.5: Number of generated events and associated precision for 4 finite volume elements at $q^2 = 2 \pm 0.125$ $(\mathrm{GeV/c^2})^2$ and $10° < \theta_{\pi^0} < 30°$ used to determine the acceptance and efficiency.

In a similar way as for the background, acceptance and efficiency values (see Tab. 5.6 and Tab. 5.7) are averaged and calculated for two $\theta^*_{e^+}$ bins: $80° < \theta^*_{e^+} < 90°$ and $140° < \theta^*_{e^+} < 150°$. From these two tables, one can see that by applying the particle identification (PID), the acceptance and efficiency is reduced at least by 50%. This

reduction is more severe for π° going backward. Cutting also with the confidence level, reduces again the acceptance and efficiency. Again, for π° going backward, the reduction is more severe.

		$q^2 = 0.605 \pm 0.005$ (GeV/c^2)^2		
		$10^\circ < \theta_{\pi^0} < 30^\circ$ Nth=2.91165 10^6	$80^\circ < \theta_{\pi^0} < 100^\circ$ Nth=1.40504 10^6	$140^\circ < \theta_{\pi^0} < 160^\circ$ Nth=517 612
PID	$80^\circ < \theta^*_{e^+} < 90^\circ$	42%	39%	23%
	$140^\circ < \theta^*_{e^+} < 150^\circ$	32%	37%	12%
PID + Cut1	$80^\circ < \theta^*_{e^+} < 90^\circ$	30%	24%	10%
	$140^\circ < \theta^*_{e^+} < 150^\circ$	24%	27%	7%
PID + Cut2	$80^\circ < \theta^*_{e^+} < 90^\circ$	29%	9%	1.8%
	$140^\circ < \theta^*_{e^+} < 150^\circ$	23%	21%	4.2%
PID + Cut3	$80^\circ < \theta^*_{e^+} < 90^\circ$	24%	9%	0.6%
	$140^\circ < \theta^*_{e^+} < 150^\circ$	19%	21%	2.5%
PID + Cut4	$80^\circ < \theta^*_{e^+} < 90^\circ$	17.8%	6.5%	0.1%
	$140^\circ < \theta^*_{e^+} < 150^\circ$	14.2%	15.5%	1.7%

Table 5.6: Signal acceptance and efficiency at $q^2 = 0.605 \pm 0.005$ (GeV/c^2)^2 are summarized in this table for two values of $\theta^*_{e^+}$.

		$q^2 = 2 \pm 0.125$ (GeV/c^2)^2		
		$10^\circ < \theta_{\pi^0} < 30^\circ$ Nth=18 486	$80^\circ < \theta_{\pi^0} < 100^\circ$ Nth=9 395	$140^\circ < \theta_{\pi^0} < 160^\circ$ Nth=2 967
PID	$80^\circ < \theta^*_{e^+} < 90^\circ$	46%	50%	34%
	$140^\circ < \theta^*_{e^+} < 150^\circ$	42%	45%	24%
PID + Cut1	$80^\circ < \theta^*_{e^+} < 90^\circ$	34%	30%	16%
	$140^\circ < \theta^*_{e^+} < 150^\circ$	24%	32%	14%
PID + Cut2	$80^\circ < \theta^*_{e^+} < 90^\circ$	26%	10%	0.6%
	$140^\circ < \theta^*_{e^+} < 150^\circ$	17%	24%	4.2%
PID + Cut3	$80^\circ < \theta^*_{e^+} < 90^\circ$	25%	10%	0.1%
	$140^\circ < \theta^*_{e^+} < 150^\circ$	16%	23%	4%
PID + Cut4	$80^\circ < \theta^*_{e^+} < 90^\circ$	18%	6.2%	0.1%
	$140^\circ < \theta^*_{e^+} < 150^\circ$	13%	17%	2%

Table 5.7: Signal acceptance and efficiency at $q^2 = 2 \pm 0.125$ (GeV/c^2)^2 are summarized in this table for two values of $\theta^*_{e^+}$.

5.3.1.3 Signal contamination

Knowing the background suppression factor, the background to signal cross section ratio as well as the signal acceptance and efficiency, the signal contamination can be calculated for each cuts. Tab. 5.8 and Tab. 5.9 show the contamination obtained. At $q^2 = 0.605 \pm 0.005$ (GeV/c^2)^2, a contamination at the percent level is reached using the condition PID+Cut1 and in principle extract the proton electromagnetic form factors for the three π° angular ranges. At $q^2 = 2 \pm 0.125$ (GeV/c^2)^2, even using a strong condition (PID+Cut4), the signal contamination remains between 7% and 14%.

		$q^2 = 0.605 \pm 0.005$ (GeV/c^2)^2		
		$10^\circ < \theta_{\pi^0} < 30^\circ$	$80^\circ < \theta_{\pi^0} < 100^\circ$	$140^\circ < \theta_{\pi^0} < 160^\circ$
PID	$80^\circ < \theta^*_{e^+} < 90^\circ$	48%	12%	20%
	$140^\circ < \theta^*_{e^+} < 150^\circ$	12%	$< 1\%$	1%
PID + Cut1	$80^\circ < \theta^*_{e^+} < 90^\circ$	1%	3.2%	$< 1\%$
	$140^\circ < \theta^*_{e^+} < 150^\circ$	$< 1\%$	$< 1\%$	$< 1\%$
PID + Cut2	$80^\circ < \theta^*_{e^+} < 90^\circ$	$< 1\%$	$< 1\%$	$< 1\%$
	$140^\circ < \theta^*_{e^+} < 150^\circ$	$< 1\%$	$< 1\%$	$< 1\%$
PID + Cut3	$80^\circ < \theta^*_{e^+} < 90^\circ$	$< 1\%$	$< 1\%$	$< 1\%$
	$140^\circ < \theta^*_{e^+} < 150^\circ$	$< 1\%$	$< 1\%$	$< 1\%$
PID + Cut4	$80^\circ < \theta^*_{e^+} < 90^\circ$	$< 1\%$	$< 1\%$	$< 1\%$
	$140^\circ < \theta^*_{e^+} < 150^\circ$	$< 1\%$	$< 1\%$	$< 1\%$

Table 5.8: The signal contamination at $q^2 = 0.605 \pm 0.005$ (GeV/c^2)^2 are summarized in this table for two values of $\theta^*_{e^+}$.

		$q^2 = 2 \pm 0.125$ (GeV/c^2)^2		
		$10^\circ < \theta_{\pi^0} < 30^\circ$	$80^\circ < \theta_{\pi^0} < 100^\circ$	$140^\circ < \theta_{\pi^0} < 160^\circ$
PID	$80^\circ < \theta^*_{e^+} < 90^\circ$	$> 100\%$	$> 100\%$	$> 100\%$
	$140^\circ < \theta^*_{e^+} < 150^\circ$	$> 100\%$	$> 100\%$	$> 100\%$
PID + Cut1	$80^\circ < \theta^*_{e^+} < 90^\circ$	62%	$> 100\%$	71%
	$140^\circ < \theta^*_{e^+} < 150^\circ$	60%	16%	$> 100\%$
PID + Cut2	$80^\circ < \theta^*_{e^+} < 90^\circ$	34%	34%	$> 100\%$
	$140^\circ < \theta^*_{e^+} < 150^\circ$	23%	18%	$> 100\%$
PID + Cut3	$80^\circ < \theta^*_{e^+} < 90^\circ$	17%	19%	$> 100\%$
	$140^\circ < \theta^*_{e^+} < 150^\circ$	12%	10%	79%
PID + Cut4	$80^\circ < \theta^*_{e^+} < 90^\circ$	10%	14%	24%
	$140^\circ < \theta^*_{e^+} < 150^\circ$	7%	7%	57%

Table 5.9: The signal contamination at $q^2 = 2 \pm 0.125$ (GeV/c^2)^2 are summarized in this table for two values of $\theta^*_{e^+}$.

5.3.2 Hadronic tensor extraction

The positron angular dependence in the virtual photon rest frame is strictly limited to L=2 spherical harmonics (spin of the virtual photon is 1) and is weighted by a linear combination of hadronic tensors. These hadronic tensors contain information on the exchanged particle.

The purpose of this section is to show that measuring the positron or the electron distribution in the virtual photon rest frame, one would access the hadronic tensors. We want here to validate the method, consequently, the acceptance and efficiency is assumed to be 100%. As previously defined, $T_{\overline{p}} = 1$ GeV, $q^2 = 0.605 \pm 0.005$ (GeV/c^2)^2 and $q^2 = 2 \pm 0.125$ (GeV/c^2)^2. To better describe the hadronic tensors over the θ_{π° polar angle, they are extracted per 1° bin. The theoretical number of counts for both q^2 intervals are displayed in Fig. 5.2 as a function of θ_{π° ($\Delta\theta_{\pi^\circ} = 1^\circ$) with an integrated luminosity of 2 fb^{-1}.

5.3.2.1 Simulation

The positron distribution in the virtual photon rest frame is generated using the theoretical five fold differential cross section (Eq. 4.44). It is possible, for well defined q^2 and Ω_{π° intervals, to calculate the theoretical number of counts N_{ij}^{th} corresponding to a finite volume element $\Delta\Omega_{e^+}^*$ (here 10° bins for $\theta_{e^+}^*$ and $\varphi_{e^+}^*$ which means 18 bins for θ and 36 for φ so 648 finite volume elements, i and j refer to the bin number):

$$N_{ij}^{th} = L_{int} \int_{\Delta q^2} \int_{\Delta\Omega_{\pi^\circ}} \int_{\Delta\Omega_{e^+}^*} \frac{d^5\sigma}{dq^2 d\Omega_{\pi^\circ} d\Omega_{e^+}^*} dq^2 d\Omega_{\pi^\circ} d\Omega_{e^+}^*, \tag{5.3}$$

where the integrated luminosity $L_{int} = 2$ fb^{-1}.

To take into account statistical effects and since this expected values might be small in some cases, one generates a random number N_{ij}^{stat} in a Poisson distribution with a mean value $\mu = N_{ij}^{th}$.

5.3.2.2 Hadronic tensor determination

This 2D distribution is then fitted by the following function $f\left(\theta_{e^+}^*, \varphi_{e^+}^*\right)$:

$$\begin{aligned} f\left(\theta_{e^+}^*, \varphi_{e^+}^*\right) = \quad & 2e^2q^2 \quad \left(\mathcal{H}_{fit}^{11} + \mathcal{H}_{fit}^{22} + \mathcal{H}_{fit}^{33}\right) \\ & -8e^2|\overrightarrow{p}_{e^+}^*|^2 \quad \left(\mathcal{H}_{fit}^{11} sin^2\theta_e^* cos^2\varphi_e^* + 2\mathfrak{Re}\mathcal{H}_{fit}^{12} sin^2\theta_e^* sin\varphi_e^* cos\varphi_e^*\right. \\ & + 2\mathfrak{Re}\mathcal{H}_{fit}^{13} sin\theta_e^* cos\theta_e^* cos\varphi_e^* + \mathcal{H}_{fit}^{22} sin^2\theta_e^* sin^2\varphi_e^* \\ & \left. + 2\mathfrak{Re}\mathcal{H}_{fit}^{23} sin\theta_e^* cos\theta_e^* sin\varphi_e^* + \mathcal{H}_{fit}^{33} cos^2\theta_e^*\right). \end{aligned} \tag{5.4}$$

Using the default fit method of root (based on the χ^2) which takes into account only non-zero bins, systematic deviations were observed. Since the fit function shape is very well constrained, it is important to take into account all bins even the empty ones. The error on a bin content (N_b) is usually defined as the $\sqrt{N_b}$. In case of a zero bin, one should have an error of zero which is not realistic. As a consequence, the fit was performed taking all bins (including non-zero bins), each bin weighted by 1. The errors were determined using Monte Carlo method by repeating the simulation and the extraction 1 000 times. The error is defined as the sigma of the gaussian fit over the distribution of the 1 000 results.

Extracted effective hadronic tensors and their corresponding errors at $T_{\overline{p}} = 1$ GeV for both $q^2 = 0.605 \pm 0.005$ (GeV/c^2)^2 and $q^2 = 2 \pm 0.125$ (GeV/c^2)^2 are displayed in Figs. 5.12 and 5.13. At $q^2 = 0.605 \pm 0.005$ (GeV/c^2)^2, extracted values at the extremum are slightly different from the theoretical due to strong and non-linear variations of one or more of the other hadronic tensors. At $q^2 = 2 \pm 0.125$ (GeV/c^2)^2, the low counting rate leads to larger error bars but the extracted values still nicely reproduce the theoretical ones within the error bars. As expected, $\mathcal{H}_{fit}^{12}$ and $\mathcal{H}_{fit}^{23}$ are found to be zero.

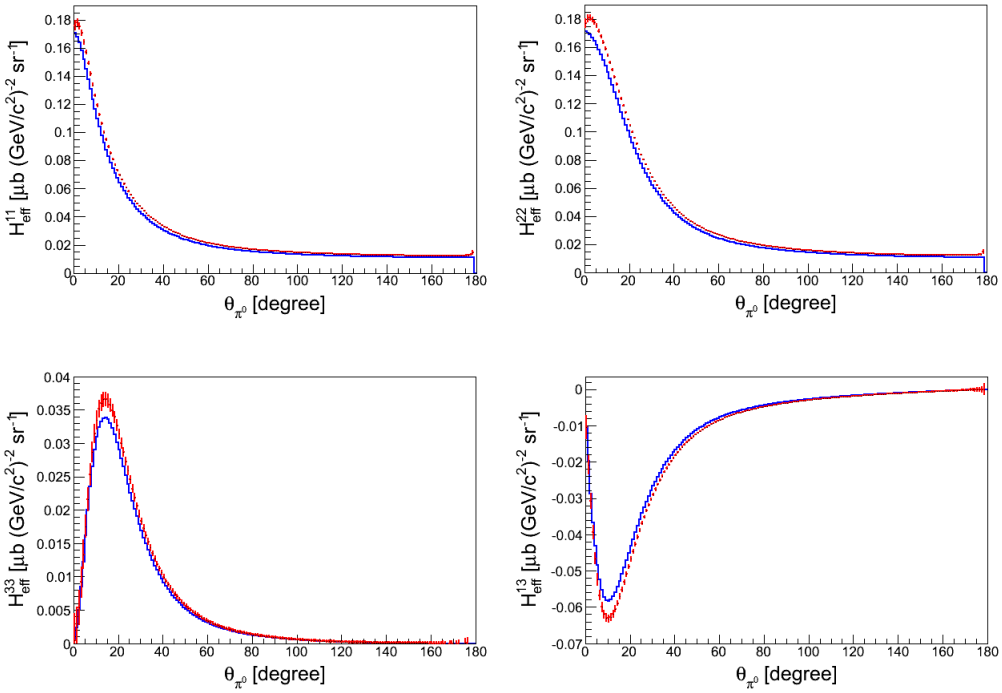

Figure 5.12: Effective hadronic tensors at $T_{\overline{p}} = 1$ GeV, $q^2 = 0.605 \pm 0.005$ $(\mathrm{GeV/c^2})^2$. Blue color stands for the theoretical values while the red color shows the extracted ones.

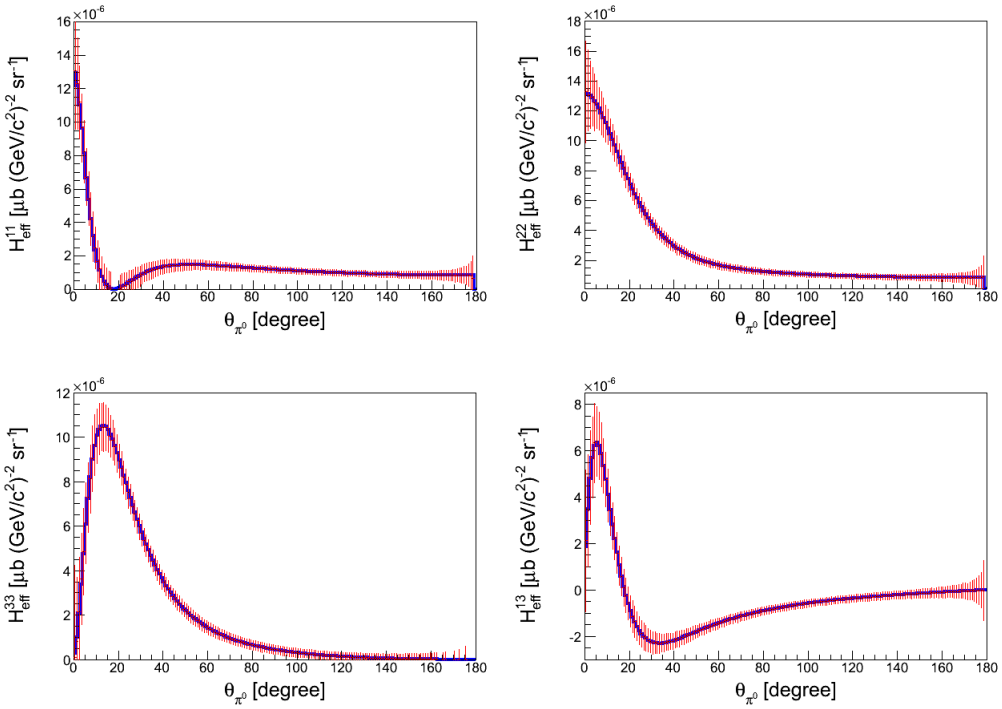

Figure 5.13: Effective hadronic tensors at $T_{\overline{p}} = 1$ GeV, $q^2 = 2 \pm 0.125$ $(\mathrm{GeV/c^2})^2$. Blue color stands for the theoretical values while the red color shows the extracted ones.

5.3.3 Form factor extraction

To demonstrate the feasibility of the proton electromagnetic form factor measurements, one needs to show that taking into account the detector resolution, the acceptance and the efficiency as well as the statistics given by the model it is still possible to extract the proton form factors.

5.3.3.1 Simulation

From the theoretical five fold differential cross section (Eq. 4.44), it is possible, for well defined q^2 and Ω_{π° intervals, to calculate the theoretical number of counts N_{ij}^{th} corresponding to a finite volume element $\Delta\Omega_{e^+}{}^*$ (here 10° bins for $\theta_{e^+}{}^*$ and $\varphi_{e^+}{}^*$ which means 18 bins for θ and 36 for φ so 648 finite volume elements, i and j refer to the bin number):

$$N_{ij}^{th} = L_{int} \int_{\Delta q^2} \int_{\Delta\Omega_{\pi^\circ}} \int_{\Delta\Omega_{e^+}{}^*} \frac{d^5\sigma}{dq^2 d\Omega_{\pi^\circ} d\Omega_{e^+}{}^*} dq^2 d\Omega_{\pi^\circ} d\Omega_{e^+}{}^*, \tag{5.5}$$

where the integrated luminosity $L_{int} = 2$ fb^{-1}.

Then to obtain the corresponding experimental number of count N^{exp} within the $\overline{\text{P}}$ANDA detector it is necessary to take into account the acceptance and efficiency leading to an expected value μ_{ij}^{th}. The acceptance and efficiency matrices previously determined are used. Furthermore, since this expected values might be small in some cases, one generates a random number N_{ij}^{exp} in a Poisson distribution with a mean value $\mu = \mu_{ij}^{th}$.

Afterwards, to be able to extract form factors, it is necessary to correct this experimental spectrum from the acceptance and the efficiency. Here, the corrected number of count in each finite volume element $\Delta\Omega_{e^+}{}^*$ is:

$$N_{ij}^{cor} \pm \delta N_{ij}^{cor} = N_{ij}^{exp}/AccEff \pm \sqrt{N_{ij}^{exp}}/AccEff. \tag{5.6}$$

All the previous steps are summarized in Fig. 5.14.

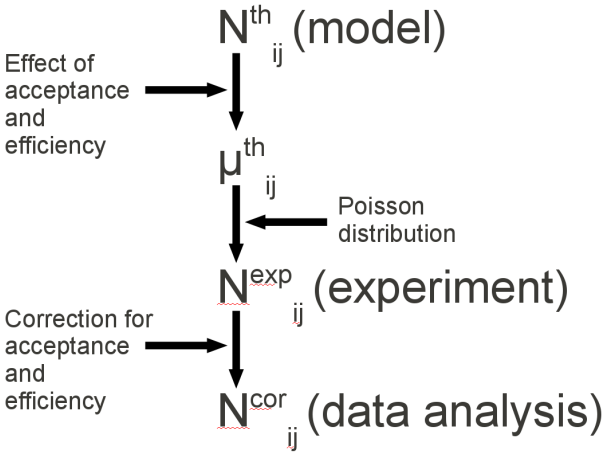

Figure 5.14: Scheme of the steps to go from N_{ij}^{th} to N_{ij}^{cor}.

Fig. 5.15 and 5.16 display N_{ij}^{th} and the corresponding N_{ij}^{cor} both in the virtual photon rest frame for $q^2 = 0.605 \pm 0.005$ $(\mathrm{GeV/c^2})^2$ and $q^2 = 2 \pm 0.125$ $(\mathrm{GeV/c^2})^2$ respectively assuming an integrated luminosity of 2 fb^{-1}. The total number of events calculated for each theoretical distribution is shown in Tab. 5.10. As first general remark, if the theoretical distribution and the simulated corrected distribution look similar, one notes the importance of the bin to bin fluctuation.

	$q^2 = 0.605 \pm 0.005$ $(\mathrm{GeV/c^2})^2$	$q^2 = 2 \pm 0.125$ $(\mathrm{GeV/c^2})^2$
$10^\circ < \theta_{\pi^0} < 30^\circ$	2.91165 10^6	18 486
$80^\circ < \theta_{\pi^0} < 100^\circ$	1.40504 10^6	9 395
$140^\circ < \theta_{\pi^0} < 160^\circ$	517 612	2 967

Table 5.10: Theoretical counting rates (100% acceptance and efficiency) assuming an integrated luminosity of 2 fb^{-1}

Starting from Fig. 5.15 ($q^2 = 0.605 \pm 0.005$ $(\mathrm{GeV/c^2})^2$), it is clear that, even with such a small interval, the statistics is not a problem. Looking at the shape of the distributions, one can still clearly see the 3 bumps in the $\theta_{e^+}{}^*$, $\varphi_{e^+}{}^*$ distributions which correspond to the theoretical distribution. At $140^\circ < \theta_{\pi^0} < 160^\circ$ the distribution is less structured: whereas the 3 bumps can still be seen in the theoretical distributions, they are hard to detect in the corrected distributions (right column of the figure).

For the case $q^2 = 2 \pm 0.125$ $(\mathrm{GeV/c^2})^2$ (Fig. 5.16), the counting rate is lower. At $10^\circ < \theta_{\pi^0} < 30^\circ$ the corrected distribution still shows the 3 bumps. At $80^\circ < \theta_{\pi^0} < 100^\circ$, despite the fluctuations, one can still guess the presence of the bumps. At $140^\circ < \theta_{\pi^0} < 160^\circ$ the case is critical, the distribution does not appear structured.

It is important to remind that the proton form factor extraction is based on the measurement of the shape of the ($\theta_{e^+}{}^*$, $\varphi_{e^+}{}^*$) distribution in the $\gamma*$ rest frame, if after correction the statistics is too low ($q^2 = 2 \pm 0.125$ $(\mathrm{GeV/c^2})^2$ and $140^\circ < \theta_{\pi^0} < 160^\circ$) either the sensitivity to the distribution shape is low ($q^2 = 0.605 \pm 0.005$ $(\mathrm{GeV/c^2})^2$ and $140^\circ < \theta_{\pi^0} < 160^\circ$), the extraction may be difficult or even not possible.

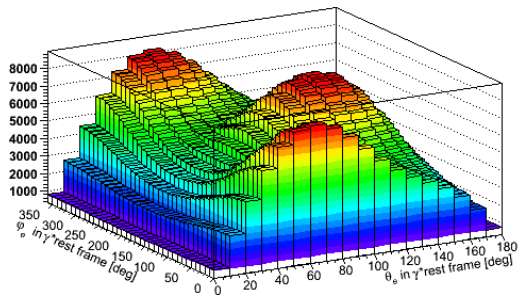

(a) N_{ij}^{th} for $10^\circ < \theta_{\pi^0} < 30^\circ$

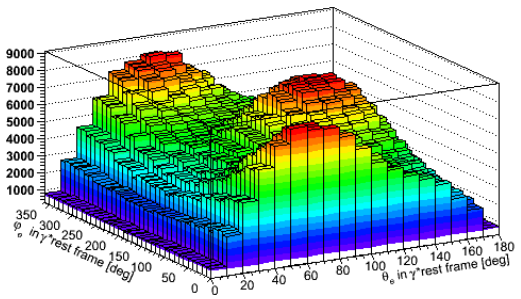

(b) N_{ij}^{cor} for $10^\circ < \theta_{\pi^0} < 30^\circ$

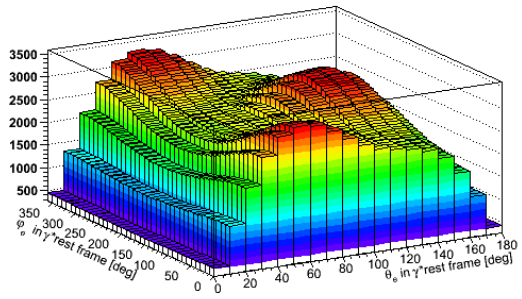

(c) N_{ij}^{th} for $80^\circ < \theta_{\pi^0} < 100^\circ$

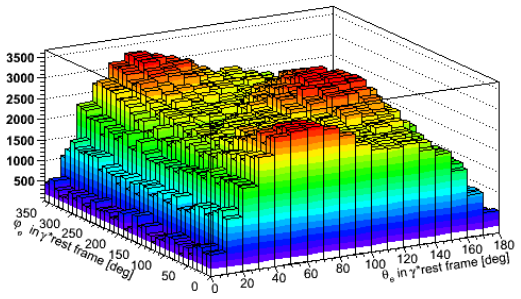

(d) N_{ij}^{cor} for $80^\circ < \theta_{\pi^0} < 100^\circ$

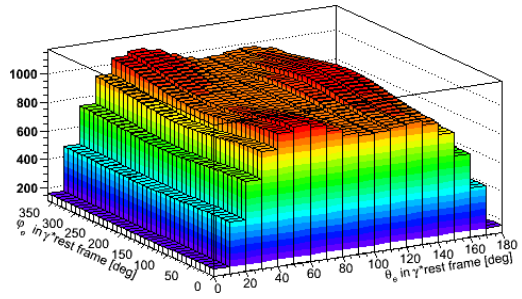

(e) N_{ij}^{th} for $140^\circ < \theta_{\pi^0} < 160^\circ$

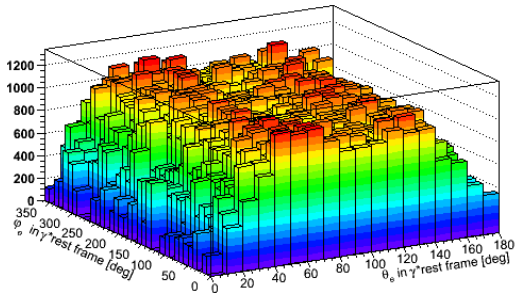

(f) N_{ij}^{cor} for $140^\circ < \theta_{\pi^0} < 160^\circ$

Figure 5.15: At $q^2 = 0.605 \pm 0.005$ $(\mathrm{GeV/c^2})^2$, on the left side, N_{ij}^{th} as a function of ${\varphi_{e^+}}^*$ and ${\theta_{e^+}}^*$, on the right side the corresponding N_{ij}^{cor} (PID+Cut1) as a function of ${\varphi_{e^+}}^*$ and ${\theta_{e^+}}^*$. For both side the integrated luminosity is 2 fb^{-1} with 10° bins for ${\varphi_{e^+}}^*$ and ${\theta_{e^+}}^*$.

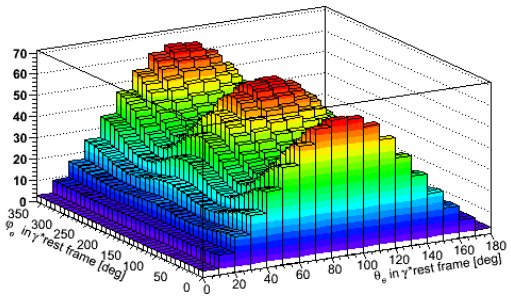

(a) N_{ij}^{th} for $10^\circ < \theta_{\pi^0} < 30^\circ$

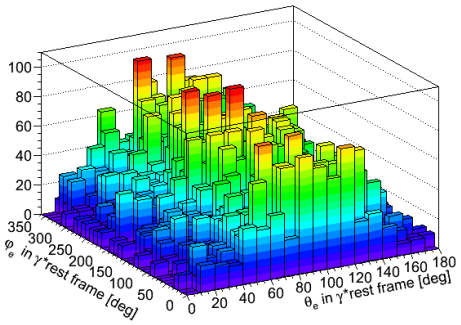

(b) N_{ij}^{cor} for $10^\circ < \theta_{\pi^0} < 30^\circ$

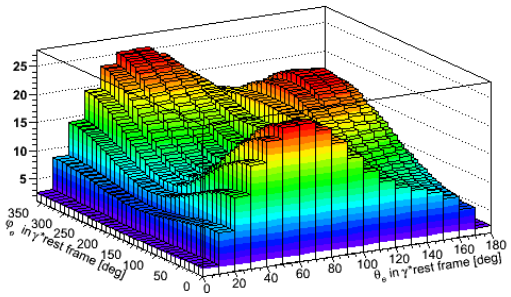

(c) N_{ij}^{th} for $80^\circ < \theta_{\pi^0} < 100^\circ$

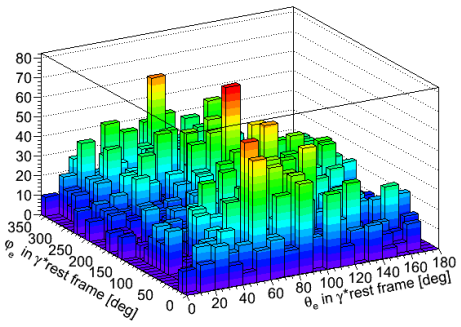

(d) N_{ij}^{cor} for $80^\circ < \theta_{\pi^0} < 100^\circ$

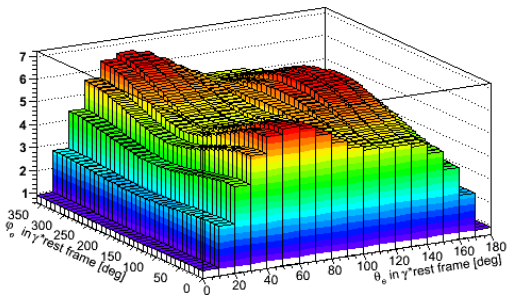

(e) N_{ij}^{th} for $140^\circ < \theta_{\pi^0} < 160^\circ$

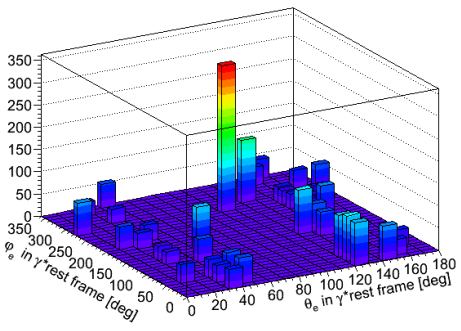

(f) N_{ij}^{cor} for $140^\circ < \theta_{\pi^0} < 160^\circ$

Figure 5.16: At $q^2 = 2 \pm 0.125$ $(\mathrm{GeV/c^2})^2$, on the left side, N_{ij}^{th} as a function of ${\varphi_{e^+}}^*$ and ${\theta_{e^+}}^*$, on the right side the corresponding N_{ij}^{cor} (PID+Cut4) as a function of ${\varphi_{e^+}}^*$ and ${\theta_{e^+}}^*$. For both side the integrated luminosity is 2 fb^{-1} with 10° bins for ${\varphi_{e^+}}^*$ and ${\theta_{e^+}}^*$.

5.3.3.2 Observables

With 10° bins for ${\theta_{e^+}}^*$ and ${\varphi_{e^+}}^*$, if a 2D histogram contains 1296 events this means that the mean bin content would be 2 with an error of 1.4. By projecting on ${\theta_{e^+}}^*$, the 1296 events are now distributed over only 18 bins which leads to a mean bin content of 36 with an error of 6. The main advantage of such projections is to reduce the error on the

extraction due to low statistics (especially at $q^2 = 2 \pm 0.125$ (GeV/c^2)^2). Therefore, the 3 projections suggested in section 4.2.3.4 were obtained. N_i^{cor}, $(N_j^{cor})'$ and $(N_j^{cor})''$ are the number of counts per 10° bin in each projection:

$$N_i^{cor} = \sum_{j=0}^{j<36} N_{ij}^{cor}, \quad (N_j^{cor})' = \sum_{i=0}^{i<18} N_{ij}^{cor}, \quad (N_j^{cor})'' = \sum_{i=9}^{i<18} N_{ij}^{cor}. \tag{5.7}$$

N_i^{cor} distribution was then fitted by $A^{cor}\,(1 + B^{cor} cos^2\theta_e^*)$, $(N_j^{cor})'$ by $C^{cor}\,(1 + D^{cor} cos2\varphi_e^*)$ and $(N_j^{cor})''$ by $E^{cor}\,(1 + F^{cor} cos2\varphi_e^* + G^{cor} cos\varphi_e^*)$ leading to a total of 7 parameters.

Then, using the following relations:

$$N^{cor} = \sum_{i=0}^{i<18} N_i^{cor} = 2A^{cor}\left(1 + \frac{B^{cor}}{3}\right), \tag{5.8}$$

$$N^{cor} = (N^{cor})' = \sum_{j=0}^{j<36} (N_j^{cor})' = 2\pi C^{cor}, \tag{5.9}$$

$$(N^{cor})'' = \sum_{j=0}^{j<36} (N_j^{cor})'' = 2\pi E^{cor}, \tag{5.10}$$

where N^{cor}, $(N^{cor})'$ and $(N^{cor})''$ correspond to the total number of counts in each projection, one reduces the parameter number to 4, namely B^{cor}, D^{cor}, F^{cor} and G^{cor} .

To have a more precise idea about these 3 projections and their corresponding fits, Figs. 5.17 and 5.18 displays as an example the cases $q^2 = 2 \pm 0.125$ (GeV/c^2)^2 for $10° < \theta_{\pi^0} < 30°$ and $80° < \theta_{\pi^0} < 100°$ in the $\gamma*$ rest frame. In Fig. 5.17(b) the $cos2\varphi_e^*$ dependence is visible with a maxima reached at 0°, 180° and 360° (blue dashed line) whereas the minima is obtained at 90° and 270° (blue dashed line). The $cos\varphi_e^*$ term can be identified in Fig. 5.17(c) since the maximum is not anymore reached at 180° (red dashed line). In Fig. 5.18, spectra exhibit larger error bars but fits can still be obtained.

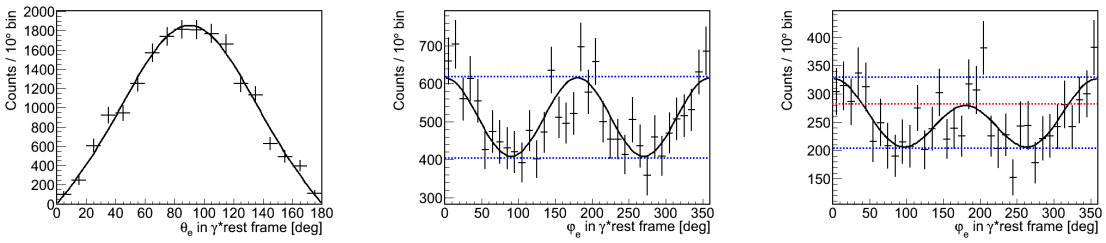

(a) N_i^{cor} (b) $(N_j^{cor})'$ (c) $(N_j^{cor})''$

Figure 5.17: N_i^{cor}, $(N_j^{cor})'$ and $(N_j^{cor})''$ corresponding to the case $q^2 = 2 \pm 0.125$ (GeV/c^2)^2 and $10° < \theta_{\pi^0} < 30°$ after corrections from acceptance and efficiency effects (PID+Cut4).

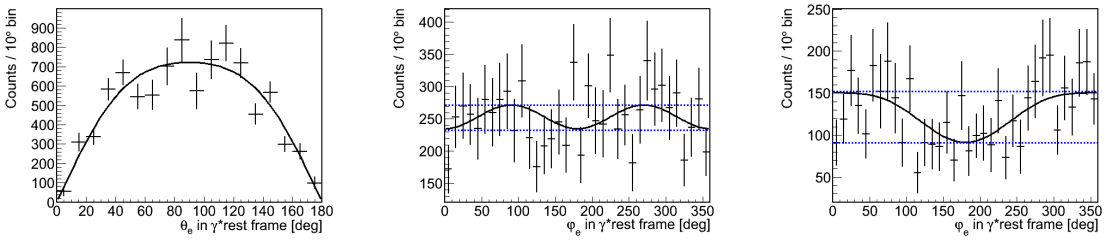

(a) N_i^{cor} (b) $(N_j^{cor})'$ (c) $(N_j^{cor})''$

Figure 5.18: N_i^{cor}, $(N_j^{cor})'$ and $(N_j^{cor})''$ corresponding to the case $q^2 = 2 \pm 0.125$ $(\mathrm{GeV/c^2})^2$ and $80^\circ < \theta_{\pi^0} < 100^\circ$ after corrections from acceptance and efficiency effects (PID+Cut4).

Before going further, it is important to have a look at the correlations between these observables. From section 4.2.3.4, it is already known that D^{cor} and F^{cor} have to be equal, so a 100% correlation should appear. For this study, the N^{cor} 2D histogram was generated 2000 times for all cases. Each histogram was then projected and fitted as previously described. The Fig. 5.19 displays as an example, for $q^2 = 2 \pm 0.125$ $(\mathrm{GeV/c^2})^2$ and $10^\circ < \theta_{\pi^0} < 30^\circ$, the correlations between the four fit parameters (similar results were obtained for the 6 cases). The dispersion is due to the statistics. The same case with 100% acceptance and efficiency gives similar correlation with smaller dispersion. As expected, D^{cor} and F^{cor} are 100% correlated parameters (Fig. 5.19(c)).

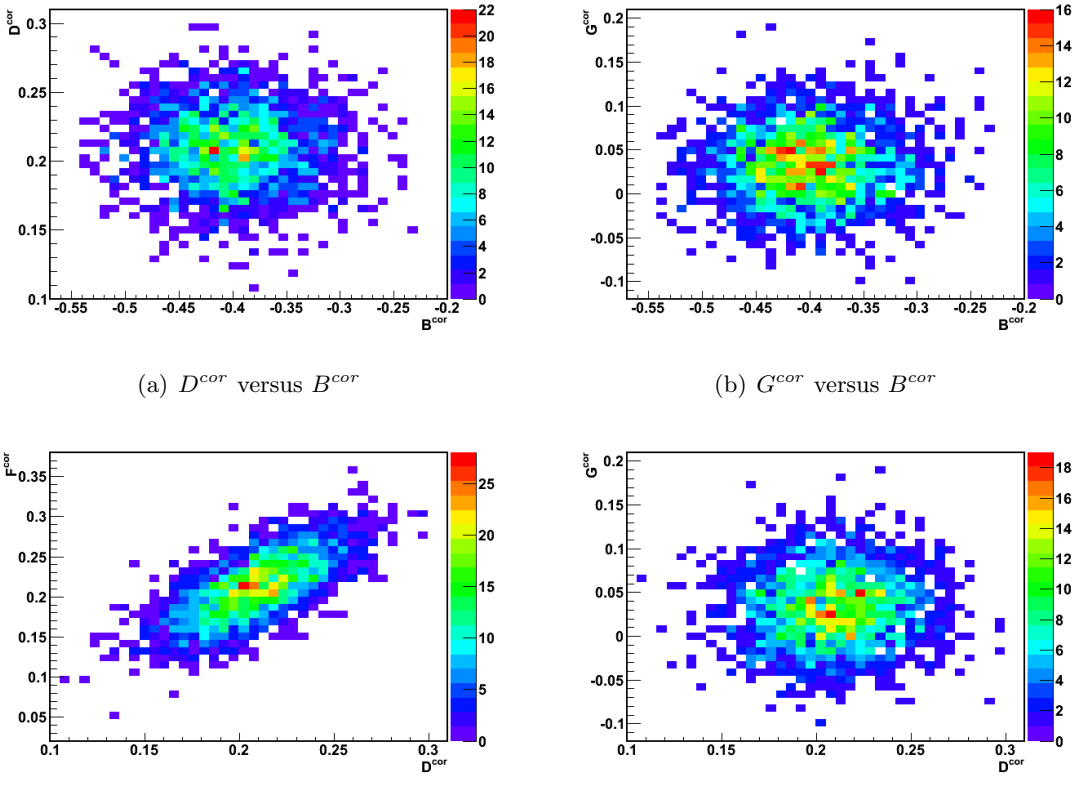

(a) D^{cor} versus B^{cor} (b) G^{cor} versus B^{cor}

(c) F^{cor} versus D^{cor} (d) G^{cor} versus D^{cor}

Figure 5.19: Correlations between the fit parameters. Example for $q^2 = 2 \pm 0.125$ $(\mathrm{GeV/c^2})^2$ and $10^\circ < \theta_{\pi^0} < 30^\circ$ (PID+Cut4).

5.3.3.3 Ratio and phase difference determination

The main use of the 3 projections is to allow the determination of the ratio $R = |G_E^p|/|G_M^p|$ and the cosine of the phase difference $cos(\delta\varphi) = cos(\varphi_E - \varphi_M)$, see Chapter 4.2.3.4. It is important to remember that R and $cos(\varphi_E - \varphi_M)$ do not depend on Ω_{π^0} which means that at a fixed q^2 value the results obtained for the three different θ_{π^0} angular range must give the same value for R and $cos(\varphi_E - \varphi_M)$. Integrating over $q^2 = 0.605 \pm 0.005$ $(\mathrm{GeV/c^2})^2$, $R = 1.065$ and $\delta\varphi \sim 4°$. For $q^2 = 2 \pm 0.125$ $(\mathrm{GeV/c^2})^2$, $R = 0.802$ and $\delta\varphi \sim 3°$. The expression of B, D, F and G are given in section 4.2.3.4. Consequently, they can be calculated for any $(R, cos(\varphi_E - \varphi_M))$ couple and be compared to B^{cor}, D^{cor}, F^{cor} and G^{cor}. Minimizing the difference between the theoretical value and the corrected one, the best couple is found. The following quantity was minimized:

$$\mathcal{F} = (B^{cor} - B)^2 + (D^{cor} - D)^2 + (F^{cor} - F)^2 + (G^{cor} - G)^2 , \tag{5.11}$$

where B, D, F and G are theroretical values recalculated for each $(R, cos(\varphi_E - \varphi_M))$ couple.

Fig. 5.20 and 5.21 present the result of the minimization function for all 6 cases. As expected, at a fixed q^2 value, the results corresponding to the three angular ranges point out the same $(R, \delta\varphi)$ interval although the sensitivity to the modulus of the phase difference $cos(\varphi_E - \varphi_M)$ appears to be low compared to the ratio R. In Fig. 5.20(c), one can see that the sensitivity to R is lower. For $q^2 = 2 \pm 0.125$ $(\mathrm{GeV/c^2})^2$ and $140° < \theta_{\pi^0} < 160°$, the theoretical number of counts is really low (around 2900 counts). After applying the PID+Cut4, the signal is too low even using the projections. Consequently the sensitivity to R and $cos(\varphi_E - \varphi_M)$ (Fig. 5.21(c)) is then completely lost.

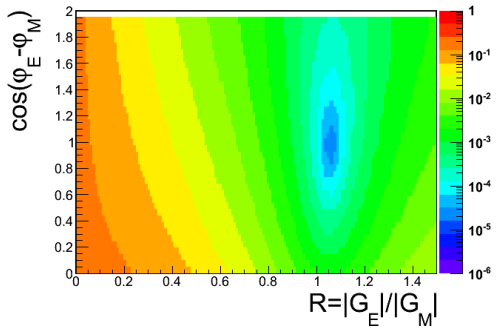

(a) $10^\circ < \theta_{\pi^0} < 30^\circ$

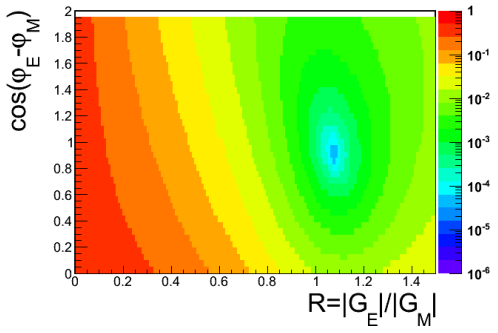

(b) $80^\circ < \theta_{\pi^0} < 100^\circ$

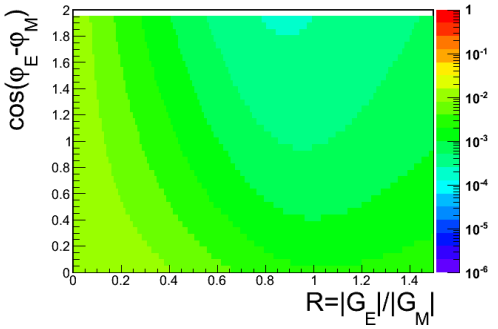

(c) $140^\circ < \theta_{\pi^0} < 160^\circ$

Figure 5.20: Display of $\mathcal{F}$ at $q^2 = 0.605 \pm 0.005$ $(\mathrm{GeV/c^2})^2$ (PID+Cut1).

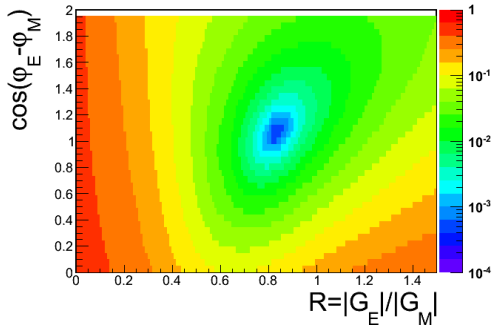

(a) $10^\circ < \theta_{\pi^0} < 30^\circ$

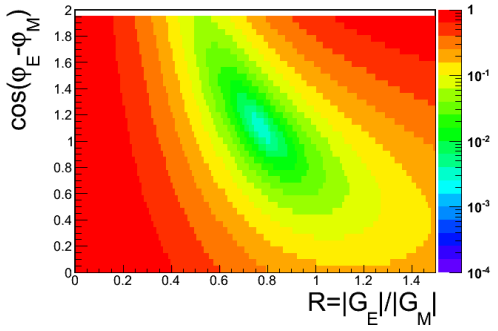

(b) $80^\circ < \theta_{\pi^0} < 100^\circ$

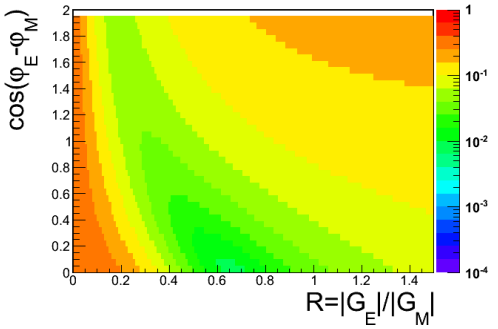

(c) $140^\circ < \theta_{\pi^0} < 160^\circ$

Figure 5.21: Display of $\mathcal{F}$ at $q^2 = 2 \pm 0.125$ $(\mathrm{GeV/c^2})^2$ (PID+Cut4).

5.3.3.4 Results and error estimations

Since D^{cor} and F^{cor} are correlated, the errors on the R and $cos(\varphi_E - \varphi_M)$ were estimated using Monte Carlo method. The N_{ij}^{cor} 2D histogram was generated 2000 times for all 6 cases. Each histogram was then projected, fitted and minimized for all 6 cases. The 2000 determination of R and $cos(\varphi_E - \varphi_M)$ are plotted. The error on R and $cos(\varphi_E - \varphi_M)$ is then equal to the σ of the gaussian fit on the R and $cos(\varphi_E - \varphi_M)$ distributions.

Fig. 5.22 and 5.23 display the results obtained for the extraction of the proton form factor ratio R. Corresponding values are summarized in Tab. 5.11 and 5.12. The magenta line point out the theoretical value of R integrated over the q^2 interval. Blue color shows the results obtained assuming 100% acceptance and efficiency (i.e.: only statistical effects are taken into account). Red color stands for the results taking into account only PID. Green color corresponds to PID+Cut1 and orange color to PID+Cut4. For most of the cases, the ratio of the proton form factor can be extracted with a reasonable error.

The effect of the acceptance and efficiency appears clearly when comparing the blue curve (100% acceptance and efficiency) and the red curve which is larger as a result of the loss of acceptance and efficiency. For $q^2 = 0.605 \pm 0.005$ $(\mathrm{GeV/c^2})^2$ and $140^\circ < \theta_{\pi^0} < 160^\circ$, Fig. 5.22(c), despite the very low acceptance and efficiency, the statistics is large enough and the ratio R can still is extracted but with a larger error. In Tab. 5.11, one can see that, even with 100% acceptance and efficiency (blue color), the σ_R of the distribution is 10 times larger at backward angles than at forward angles (7% compared to 0.7%). This factor is due to the loss of sensitivity to the effective hadronic tensors at backward angles (see Chapter 5.1.1.3).

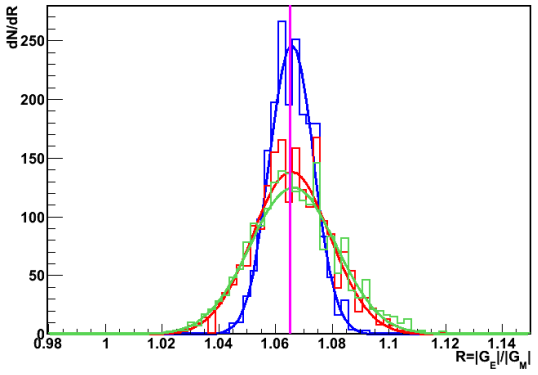

(a) $10^{\circ} < \theta_{\pi^0} < 30^{\circ}$

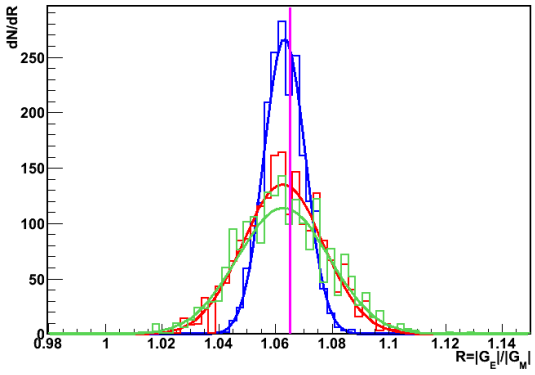

(b) $80^{\circ} < \theta_{\pi^0} < 100^{\circ}$

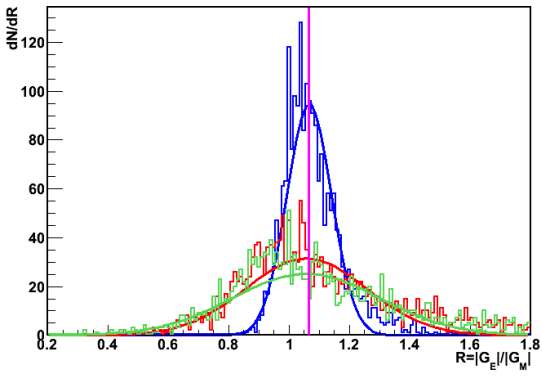

(c) $140^{\circ} < \theta_{\pi^0} < 160^{\circ}$

Figure 5.22: Distributions of the extracted proton form factor ratio at $q^2 = 0.605 \pm 0.005$ $(\mathrm{GeV/c^2})^2$. The magenta line shows the theoretical value whereas the blue line displays the results assuming 100% acceptance and efficiency. The red line presents the results after PID cut whereas the green one shows after PID+Cut1. In 5.22(c) x-scale is different.

$q^2 = 0.605 \pm 0.005$ $(\mathrm{GeV/c^2})^2$		
$10^{\circ} < \theta_{\pi^{\circ}} < 30^{\circ}$	$80^{\circ} < \theta_{\pi^{\circ}} < 100^{\circ}$	$140^{\circ} < \theta_{\pi^{\circ}} < 160^{\circ}$
$R = 1.0656$	$R = 1.0656$	$R = 1.0656$
1.0657 ± 0.0002	1.0632 ± 0.0002	1.0667 ± 0.0023
$\sigma = 0.0077 \pm 0.0001$	$\sigma = 0.0072 \pm 0.0001$	$\sigma = 0.0742 \pm 0.0016$
1.0655 ± 0.0003	1.0626 ± 0.0003	1.0564 ± 0.0062
$\sigma = 0.0137 \pm 0.0003$	$\sigma = 0.0143 \pm 0.0003$	$\sigma = 0.2010 \pm 0.0057$
1.0662 ± 0.0004	1.0628 ± 0.0004	1.0568 ± 0.0073
$\sigma = 0.0152 \pm 0.0003$	$\sigma = 0.0161 \pm 0.0003$	$\sigma = 0.2439 \pm 0.0069$

Table 5.11: Results for the proton form factor ratio in the $q^2 = 0.605 \pm 0.005$ $(\mathrm{GeV/c^2})^2$ interval. Blue color shows the results assuming 100% acceptance and efficiency whereas red color presents the results after PID cut. Green color includes PID+Cut1.

As expected, at $q^2 = 2 \pm 0.125$ $(\mathrm{GeV/c^2})^2$ and $140° < \theta_{\pi^\circ} < 160°$, the statistics is too low to extract the ratio, even assuming 100% acceptance and efficiency, .

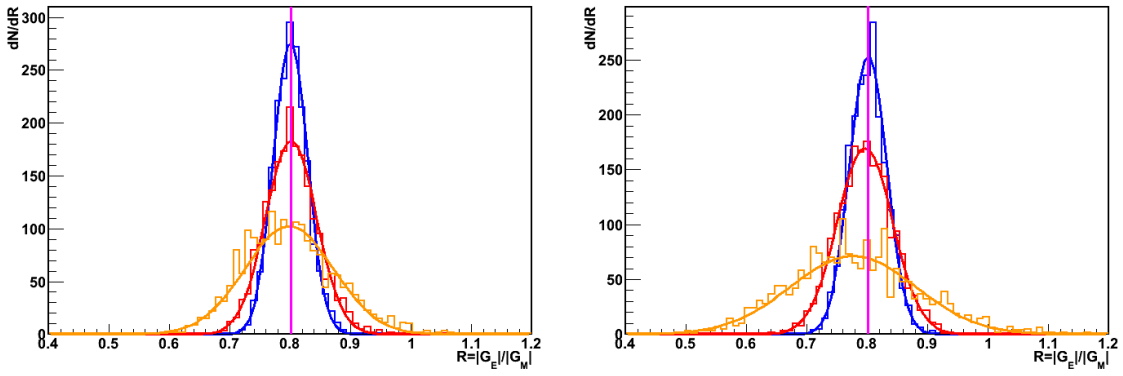

(a) $10° < \theta_{\pi^0} < 30°$ (b) $80° < \theta_{\pi^0} < 100°$

Figure 5.23: Distributions of the extracted proton form factor ratio at $q^2 = 2 \pm 0.125$ $(\mathrm{GeV/c^2})^2$. The magenta line shows the theoretical value whereas the blue line displays the results assuming 100% acceptance and efficiency. The red line presents the results after PID cut whereas the orange one shows after PID+Cut4.

$q^2 = 2. \pm 0.125$ $(\mathrm{GeV/c^2})^2$		
$10° < \theta_{\pi^\circ} < 30°$	$80° < \theta_{\pi^\circ} < 100°$	$140° < \theta_{\pi^\circ} < 160°$
$R = 0.8024$	$R = 0.8024$	$R = 0.8024$
0.8006 ± 0.0006	0.8016 ± 0.0007	X
$\sigma = 0.0282 \pm 0.0005$	$\sigma = 0.0307 \pm 0.0005$	X
0.8016 ± 0.0010	0.7965 ± 0.0010	X
$\sigma = 0.0421 \pm 0.0007$	$\sigma = 0.0458 \pm 0.0008$	X
0.7984 ± 0.0018	0.7765 ± 0.0025	X
$\sigma = 0.0735 \pm 0.0013$	$\sigma = 0.1039 \pm 0.0020$	X

Table 5.12: Results for the proton form factor ratio in the $q^2 = 2. \pm 0.125$ $(\mathrm{GeV/c^2})^2$ interval. Blue color shows the results assuming 100% acceptance and efficiency whereas red color presents the results after PID cut. Orange color includes PID+Cut4.

Fig. 5.24 presents the relative resolution on R as a function of θ_{π°. At $q^2 = 0.605 \pm 0.005$ $(\mathrm{GeV/c^2})^2$, the resolution on R is at the percent level for $10° < \theta_{\pi^\circ} < 30°$ and $80° < \theta_{\pi^\circ} < 100°$. For $140° < \theta_{\pi^\circ} < 160°$, it reaches 20%. At $q^2 = 2. \pm 0.125$ $(\mathrm{GeV/c^2})^2$, it is about 10%. Since the resolution does not seem to depend very much on the θ_{π° at least in the forward hemisphere, we expect to extract ratios with similar resolution over an extended angular range and provides means to better constraint the mechanism. Even with this moderate resolution, these results are extremely valuable since they will be the very first measurements in the unphysical region.

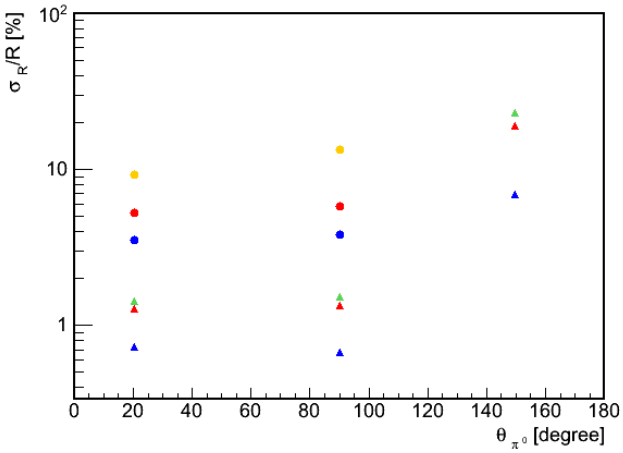

Figure 5.24: Relative resolution on R as a function of θ_{π°. Triangles correspond to $q^2 = 0.605 \pm 0.005$ $(\mathrm{GeV/c^2})^2$ and circles to $q^2 = 2. \pm 0.125$ $(\mathrm{GeV/c^2})^2$. Blue color shows the case 100% of acceptance and efficiency, red , green and orange colors includes only PID cuts, PID cut +Cut1 and PID cut + Cut4 respectively.

It has been shown previously that the sensitivity to $cos(\varphi_E - \varphi_M)$ was low at backward π° and at both q^2 values (see Fig. 5.20 and 5.21). As expected, for these two cases, $cos(\varphi_E - \varphi_M)$ could not be extracted. The results for $cos(\varphi_E - \varphi_M)$ are displayed in Fig. 5.25 and 5.26. Blue color shows the results obtained assuming 100% acceptance and efficiency, red color includes only PID cut, green one PID+Cut1 and orange color stands for PID+Cut4.

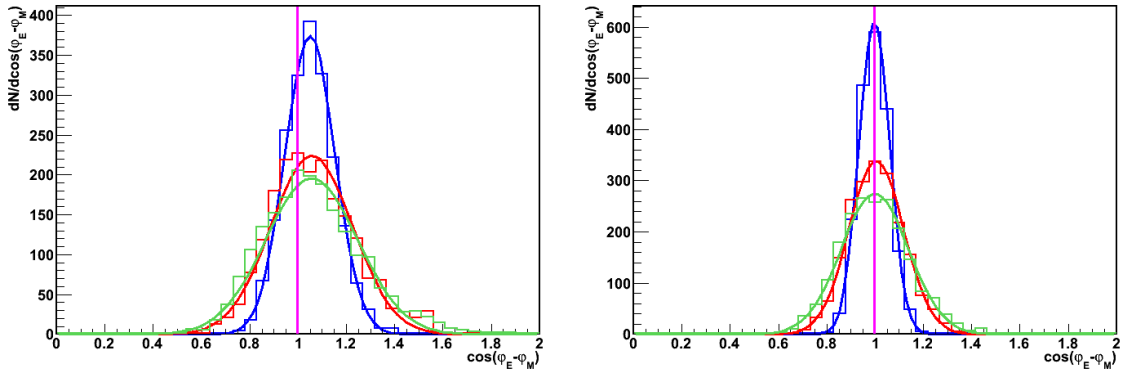

(a) $10^\circ < \theta_{\pi^0} < 30^\circ$ (b) $80^\circ < \theta_{\pi^0} < 100^\circ$

Figure 5.25: Distributions of the extracted $cos(\varphi_E - \varphi_M)$ at $q^2 = 0.605 \pm 0.005$ $(\mathrm{GeV/c^2})^2$. The magenta line shows the theoretical value whereas the blue line displays the results assuming 100% acceptance and efficiency. The red line presents the results after PID cut whereas the green one shows after PID+Cut1.

$q^2 = 0.605 \pm 0.005$ (GeV/c^2)^2		
$10^\circ < \theta_{\pi^\circ} < 30^\circ$	$80^\circ < \theta_{\pi^\circ} < 100^\circ$	$140^\circ < \theta_{\pi^\circ} < 160^\circ$
$cos(\varphi_E - \varphi_M) = 0.998$	$cos(\varphi_E - \varphi_M) = 0.998$	$cos(\varphi_E - \varphi_M) = 0.998$
1.049 ± 0.002	0.997 ± 0.001	X
$\sigma = 0.103 \pm 0.002$	$\sigma = 0.063 \pm 0.001$	X
1.057 ± 0.004	1.005 ± 0.003	X
$\sigma = 0.169 \pm 0.003$	$\sigma = 0.113 \pm 0.002$	X
1.056 ± 0.005	0.999 ± 0.003	X
$\sigma = 0.190 \pm 0.003$	$\sigma = 0.140 \pm 0.002$	X

Table 5.13: Results for the $cos(\varphi_E - \varphi_M)$ in the $q^2 = 0.605 \pm 0.005$ (GeV/c^2)^2 interval. Blue color shows the results assuming 100% acceptance and efficiency whereas red color presents the results after PID cut. Green color includes PID+Cut1.

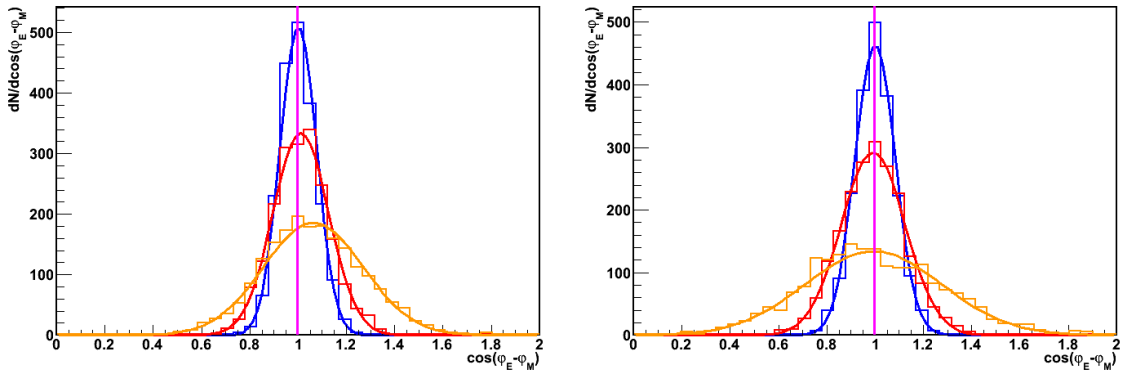

(a) $10^\circ < \theta_{\pi^0} < 30^\circ$ (b) $80^\circ < \theta_{\pi^0} < 100^\circ$

Figure 5.26: Distributions of the extracted $cos(\varphi_E - \varphi_M)$ at $q^2 = 2 \pm 0.125$ (GeV/c^2)^2. The magenta line shows the theoretical value whereas the blue line displays the results assuming 100% acceptance and efficiency. The red line presents the results after PID cut whereas the orange one shows after PID+Cut4.

$q^2 = 2. \pm 0.125$ (GeV/c^2)^2		
$10^\circ < \theta_{\pi^\circ} < 30^\circ$	$80^\circ < \theta_{\pi^\circ} < 100^\circ$	$140^\circ < \theta_{\pi^\circ} < 160^\circ$
$cos(\varphi_E - \varphi_M) = 0.999$	$cos(\varphi_E - \varphi_M) = 0.999$	$cos(\varphi_E - \varphi_M) = 0.999$
1.001 ± 0.002	0.999 ± 0.002	X
$\sigma = 0.076 \pm 0.001$	$\sigma = 0.084 \pm 0.001$	X
1.011 ± 0.003	0.992 ± 0.003	X
$\sigma = 0.116 \pm 0.002$	$\sigma = 0.132 \pm 0.002$	X
1.063 ± 0.005	0.993 ± 0.006	X
$\sigma = 0.207 \pm 0.003$	$\sigma = 0.283 \pm 0.005$	X

Table 5.14: Results for the $cos(\varphi_E - \varphi_M)$ in the $q^2 = 2. \pm 0.125$ (GeV/c^2)^2 interval. Blue color shows the results assuming 100% acceptance and efficiency whereas red color presents the results after PID cut. Orange color includes PID+Cut4.

Fig. 5.27 presents the relative resolution on $cos(\varphi_E - \varphi_M)$ as a function of $\theta_{\pi^{\circ}}$. At $q^2 = 0.605 \pm 0.005$ (GeV/c^2)^2, the resolution reaches 10-20%. At $q^2 = 2. \pm 0.125$ (GeV/c^2)^2, it is 20-30%. Again, other $\theta_{\pi^{\circ}}$ angular ranges can be used to further improved the model.

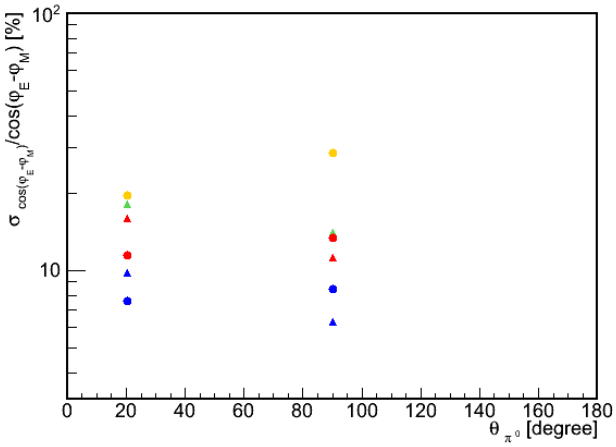

Figure 5.27: Relative resolution on $cos(\varphi_E - \varphi_M)$ as a function of $\theta_{\pi^{\circ}}$. Triangles correpond to $q^2 = 0.605 \pm 0.005$ (GeV/c^2)^2 and circles to $q^2 = 2. \pm 0.125$ (GeV/c^2)^2. Blue color shows the case 100% of acceptance and efficiency, red , green and orange colors includes only PID cuts, PID cut +Cut1 and PID+Cut4 respectively.

It is also interesting to see the variation of the relative resolution on $cos(\varphi_E - \varphi_M)$ as a function of $cos(\varphi_E - \varphi_M)$. For this purpose, $cos(\varphi_E - \varphi_M)$ was artificially fixed to 0.5 corresponding to a phase difference of 60°. Fig. 5.28 illustrates the results at $q^2 = 0.605 \pm 0.005$ (GeV/c^2)^2 and $10^{\circ} < \theta_{\pi^{\circ}} < 30^{\circ}$. Violet color corresponds to $cos(\varphi_E - \varphi_M) = 0.5$ with 23% resolution (corresponding to a resolution of approximately 8° on the phase difference) whereas the green color shows the previous result with $cos(\varphi_E - \varphi_M)$ close to 1 with 18%.

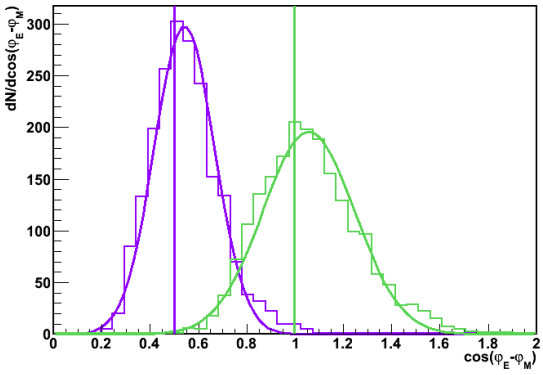

Figure 5.28: Relative resolution on $cos(\varphi_E - \varphi_M)$ as a function of θ_{π° at $q^2 = 0.605 \pm 0.005$ $(\mathrm{GeV/c^2})^2$ and $10^\circ < \theta_{\pi^\circ} < 30^\circ$. Both curves include PID cut +Cut1. Green curve corresponds to the previous result. Violet color corresponds to $cos(\varphi_E - \varphi_M) = 0.5$.

Chapter 6

EMC backward end cap studies

To determine the resolution and the efficiency of the backward end cap (described in Sec. 2.2.2), several simulations have been performed with the Pandaroot software. Pandaroot is an object oriented software currently under development for the $\overline{\text{P}}$ANDA experiment. Included geometry and settings for the simulations are first presented. Then the simulation results are discussed and finally the resolutions and efficiencies are shown.

6.1 Simulations

6.1.1 Geometry

The first thing to know before starting simulations is what is the included geometry in PandaRoot. Have been included: solenoid and dipole magnets, pipe, MVD, STT, TOF, DIRC, EMC, MDT and yoke. D.Khaneft [63] has implemented the backward end cap geometry designed by D.Rodriguez [64]. The Fig. 6.1 presents the geometry included in the full simulation. Fig. 6.2 details the detector part we are interested in.

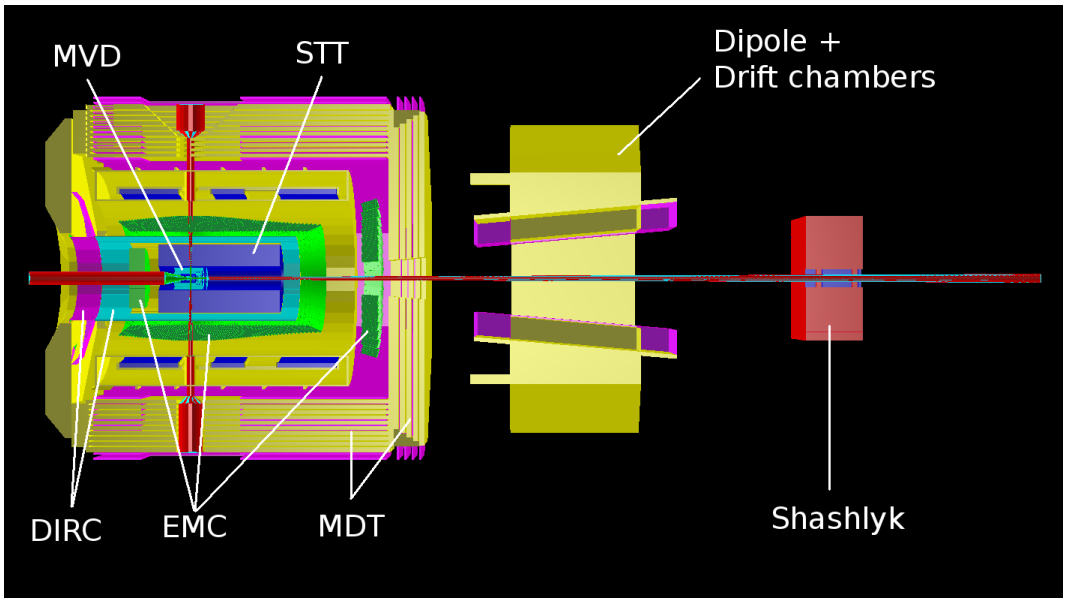

Figure 6.1: Geometry of $\overline{\text{P}}$ANDA detector included. The microvertex (MVD), straw tubes (STT), Cherenkov (DIRC), drift chambers (MDC) and muon (MDT) detectors are included. The electromagnetic (EMC) and the Shashlyk calorimeter are also in as well as the solenoid and the dipole magnets.

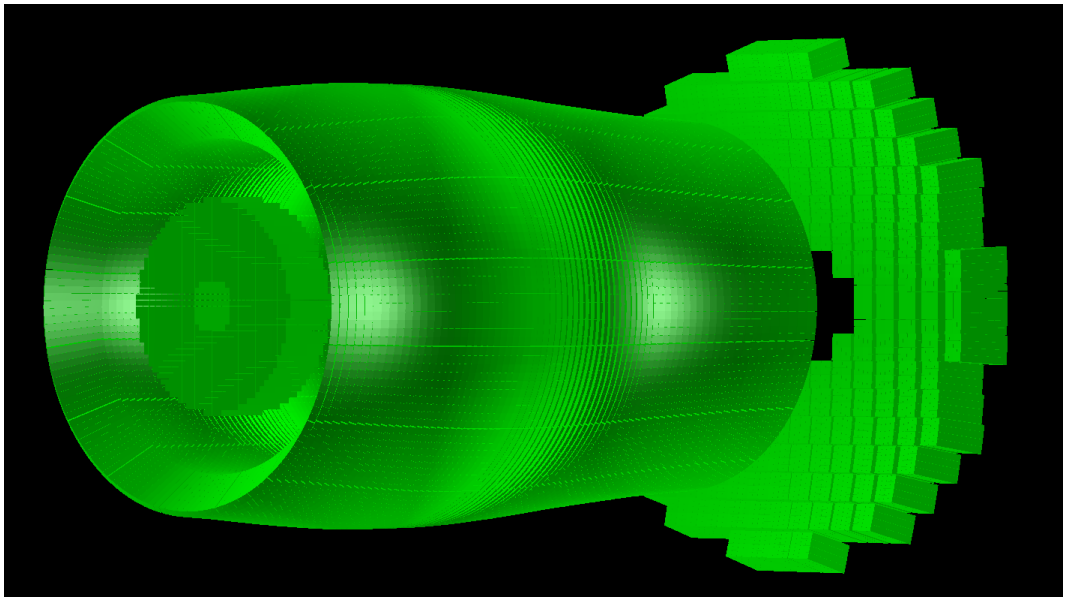

Figure 6.2: Geometry of the electromagnetic calorimeter included. The barrel and both forward and backward end caps are visible.

6.1.2 Settings

To characterize the backward end cap, the following simulations have been done on the Mainz cluster:

- one photon per event,
- number of events: 50000,
- energy: 0.1 GeV, 0.25 GeV and 0.5 GeV,
- ϕ: 1°, 22.5°, 45°,
- θ: 145°, 150°, 155°, 160°, 165°.

The Fig. 6.3 presents for the 3 values of ϕ the theoretical tracks of the photons for the 5 values of θ. One can see that for $\theta = 145°$ the backward end cap is not at all hit. There is neither hits for the case $\theta = 165°$ and $\phi = 45°$. Consequently, for those 4 cases, the backward endcap should not, in principle, give signals.

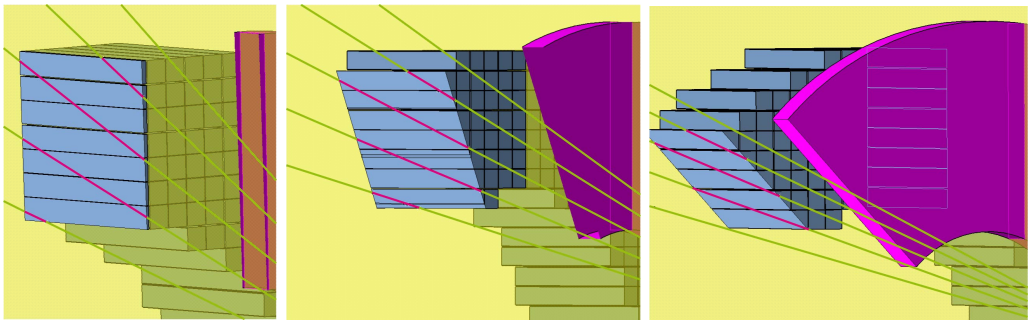

(a) $\phi = 1°$ (b) $\phi = 22.5°$ (c) $\phi = 45°$

Figure 6.3: Theoretical photon tracks depending on ϕ and θ for the new EMC design, from [64].

6.2 True Monte Carlo results

This results include the Monte Carlo and the GEANT4 transport with the energy loss and multiple scattering using the geometry previously described.

6.2.1 Spatial distribution of hits

The Fig. 6.4 shows the hit positions in the (x-y) plane for E=0.25 GeV, $\phi = 45°$ and four different θ angles. One can note that a "ring" is visible. It corresponds to the projection on the (x-y) plane of the barrel hits. Another important point is the number of entries up to few millions whereas only 50 000 events have been simulated in each cases. Actually, all secondary hits are also plotted.

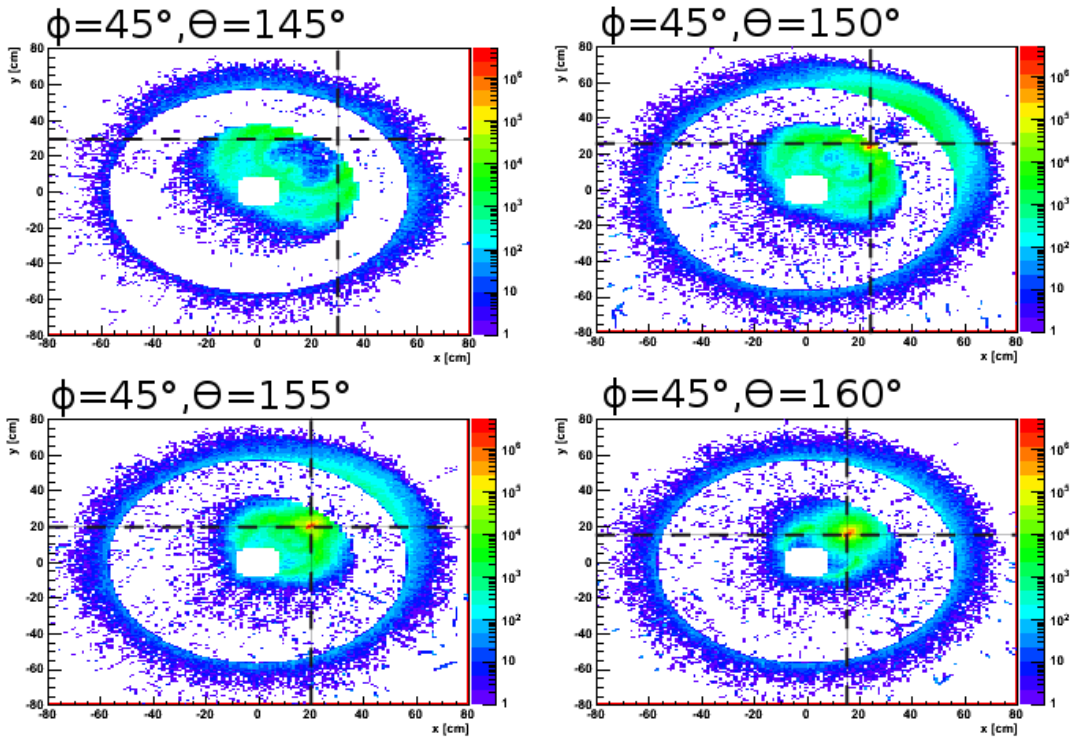

Figure 6.4: Hit positions in the (x-y) plane for E=0.25 GeV, $\phi = 45°$. The upper left picture stands for $\theta = 145°$, the upper right for $\theta = 150°$, the bottom left for $\theta = 155°$ and the bottom right for $\theta = 160°$. One bin per cm for both x and y axis.

Since for $\theta = 145°$ the backward is not at all hit, the results concerning the case $\phi = 45°$ and $\theta = 145°$ are displayed in Fig. 6.4 is quite surprising. Actually there is an important quantity of signals in the backward end cap. Looking more carefully to the event tracks by hand, it has been pointed out that bremsstrahlung and pair creation in the microvertex detector and in the straw tubes were responsible for those patterns. The Fig. 6.5 presents (for $\phi = 45°$, $\theta = 145°$, $E_\gamma = 0.1$ GeV) two examples of interaction points in the detectors (here the red squares). Pink tracks correspond to photons, yellow one to electron and green one to positron.

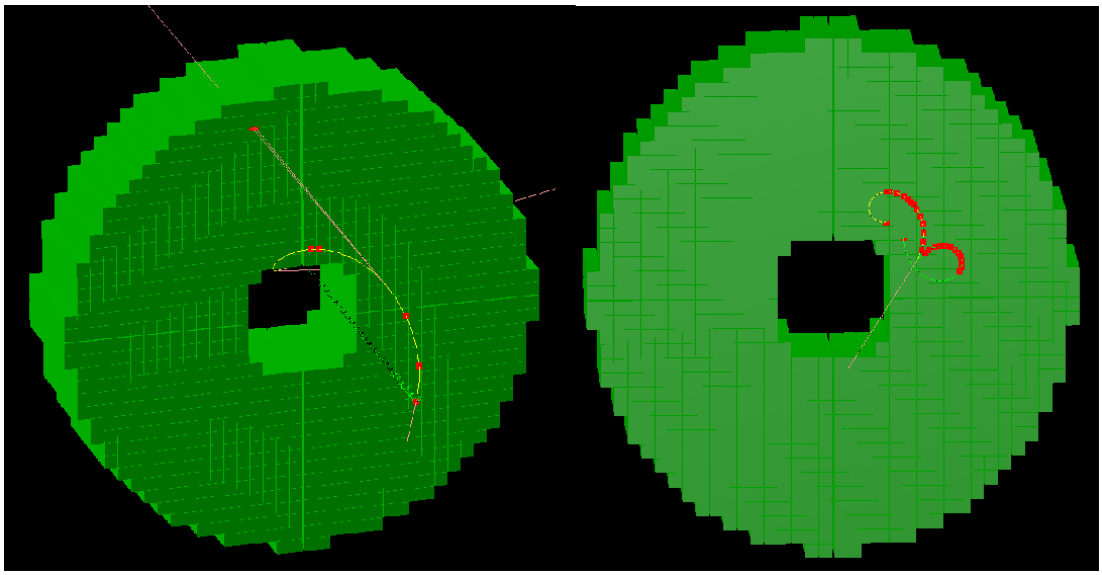

Figure 6.5: Bremsstrahlung and pair creation for $\phi = 45°$, $\theta = 145°$, $E_\gamma = 0.1$ GeV. Pink tracks correspond to photons, yellow one to electron and green one to positron. Red Squares are interaction points in the detectors.

6.3 Digitalization results

6.3.1 Spatial distribution of clusters

Digitalization starts from the True Monte Carlo results and returns the corresponding electronic signals. A cluster is connected area of crystals with an energy deposition above a predefined threshold. The Fig. 6.6 shows the cluster position for E=0.25 GeV, $\phi = 45°$ and four different θ angles. One must note that the cluster position is defined via the center of gravity method. Comparing this figure with the Fig. 6.4 where the Z-axis is in log scale, one can see that the shapes are similar, that the photons are reconstructed at the good positions (see red dots) and also that the "ring" corresponding to the projection on the (x-y) plane of the barrel hits is still visible.

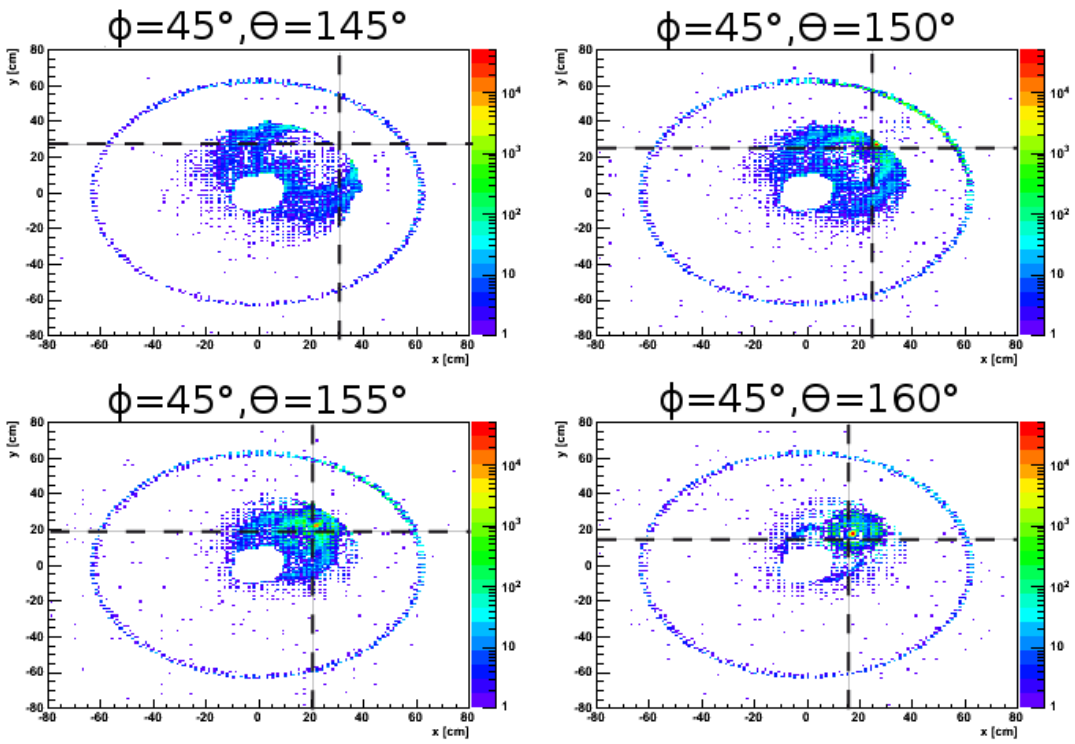

Figure 6.6: Cluster positions in the (x-y) plane for E=0.25 GeV, $\phi = 45°$. The upper left picture stands for $\theta = 145°$, the upper right for $\theta = 150°$, the bottom left for $\theta = 155°$ and the bottom right for $\theta = 160°$. One bin per cm for both x and y axis.

6.3.2 Cluster Multiplicity

Having a look to the cluster multiplicity, one can see that about 65% of the events have a cluster multiplicity which is at least two. In order to have a multiplicity equal to one, the more energetic cluster per event is kept. Fig. 6.7 presents as an example the case E=0.25 GeV, $\phi = 45°$ and $\theta = 160°$. On the left hand is the multiplicity, on the middle the cluster positions and on the right hand the cluster positions with the condition on the energy deposit. One can see that applying this condition, all the outer clusters are removed. Bremsstrahlung and pair creation effects are nevertheless still present. The same results can be observed for all cases. Now, the next step is to check the energy distribution of the clusters without and with this condition.

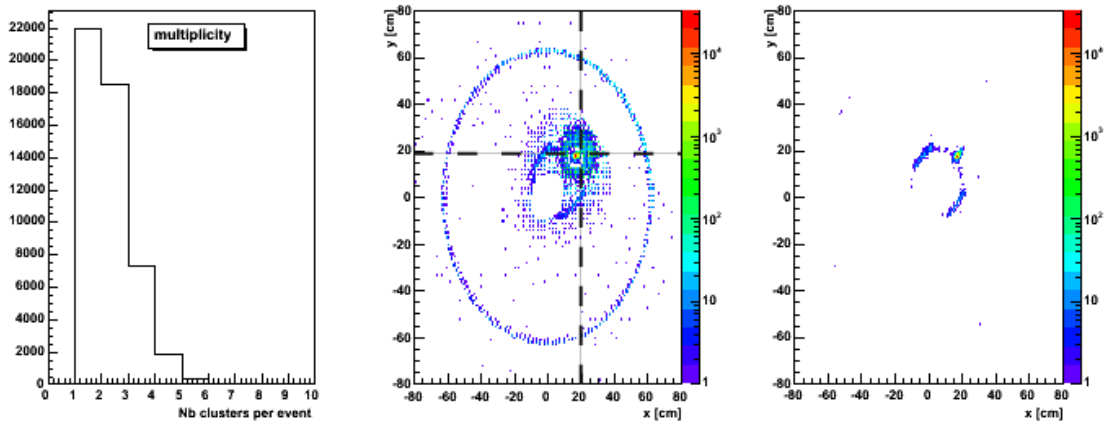

Figure 6.7: Cluster positions in the (x-y) plane for E=0.25 GeV, $\phi = 45°$ and $\theta = 155°$. The left hand side picture displays the cluster multiplicity. The central picture shows the corresponding cluster positions. In the right hand side picture, only the most energetic cluster per event is plotted. One bin per cm for both x and y axis.

6.3.3 Energy distribution

Here, one example of the energy distribution. Fig. 6.8(a) presents the energy distribution for the case: E=0.25 GeV, $\phi = 45°$ and $\theta = 160°$. Going to the Fig. 6.9, one can see a zoom over the region $E < 0.02$ GeV (left hand) and $E > 0.15$ GeV (right hand).

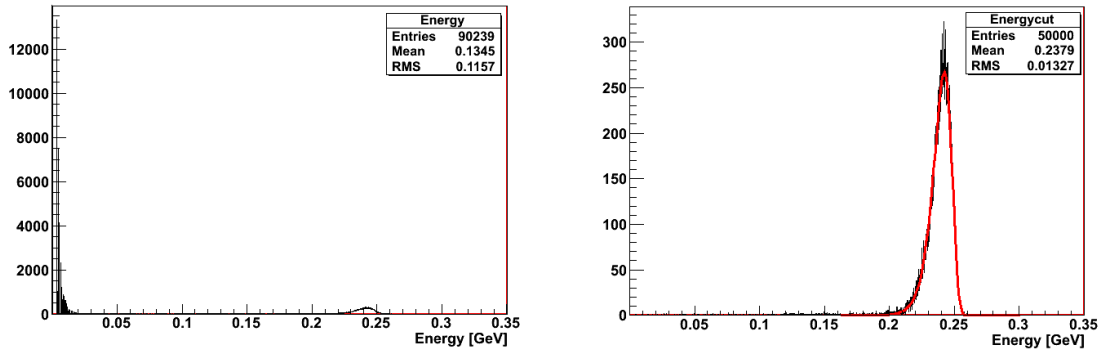

(a) Without cluster selection

(b) With cluster selection

Figure 6.8: Energy distribution of the clusters for E=0.25 GeV, $\phi = 45°$ and $\theta = 160°$. On the left side the energy distribution for the overall clusters. On the right side, the energy distribution keeping only the most energetic cluster for each events.

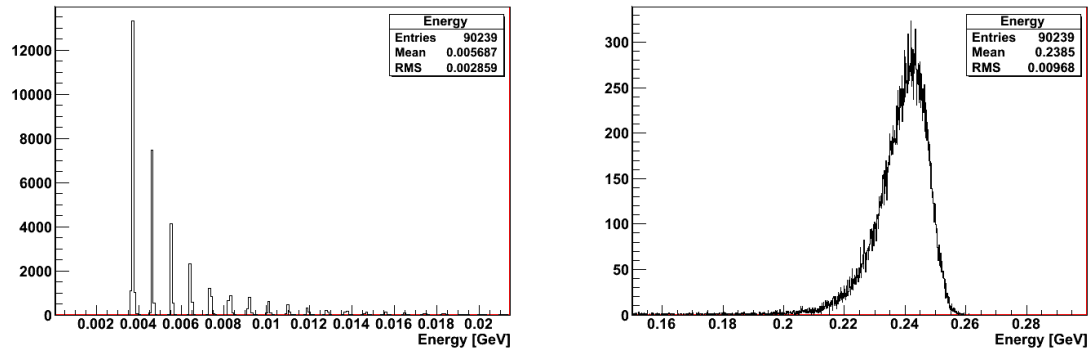

(a) Low energy

(b) Peak energy

Figure 6.9: Zoom on Fig. 6.8(a)

Looking to peak energy, one can see that its position is correct. Going to the low energy peak, a very well structure starting from 3 MeV (corresponding to the threshold energy of a cluster) is seen: around 0.9 MeV between each peak. This is problematic in case of studies at low energy like 30 MeV and even for 100 MeV. Looking to the EMC parameters for the digitalization, it appears that the parameter "EnergyRange" is equal to 15 and the parameter "NBits" is 14. This implies a quantization step of 15 GeV/$(2^{14}-1) = 0.92$ MeV and that two conversion slopes are necessary.

Fig. 6.8(b) to compare to Fig. 6.8(a) presents energy distribution of the clusters after selection for E=0.25 GeV, $\phi = 45°$ and $\theta = 160°$. The main difference comes from the suppression of the low energy counts. One can also note that the Novosibirsk fit (red) nicely agrees with the spectrum. The Novosibirsk function was defined as

$$f(E) = A \exp\left\{ -\frac{1}{2}\left[\frac{\ln^2\left[1 + \frac{(E-E_0)}{\sigma}\frac{\sinh\left(\tau\sqrt{\ln 4}\right)}{\sqrt{\ln 4}}\right]}{\tau^2} + \tau^2 \right] \right\}, \tag{6.1}$$

where A is a normalization factor, E_0 is the most probable value and τ corresponds to the tail parameter. The full width at half maximum (FWHM) can be expressed as $FWHM = 2\sqrt{ln4}\sigma$.

6.4 Resolution and Efficiency

In the resolution and efficiency studies, have been taken into account the energy distribution spectra applying the cluster selection.

Fig. 6.10, Fig. 6.11 and Fig. 6.12 show the results for the resolution and the efficiency at E=0.5 GeV, E=0.25 GeV and E=0.1 GeV. The resolution is defined as the ratio of the full width at half maximum (FWHM) to the most probable value. The efficiency is the ratio of the integral from $E_0 - 3\sigma$ up to $E_0 + 2\sigma$ of the Novosibirsk function to the generated energy. The left hand picture presents the resolution and the right one

the efficiency. The errors on the resolution is plotted and is very small due to the high statistics used for the simulation. The horizontal error bar is due to the binning (one degree per bin). Due to the lack of time, results for E=0.03 GeV and E=0.7 GeV are not presented here. One can see that at low energy the resolution is around 12% and gets better increasing the energy.

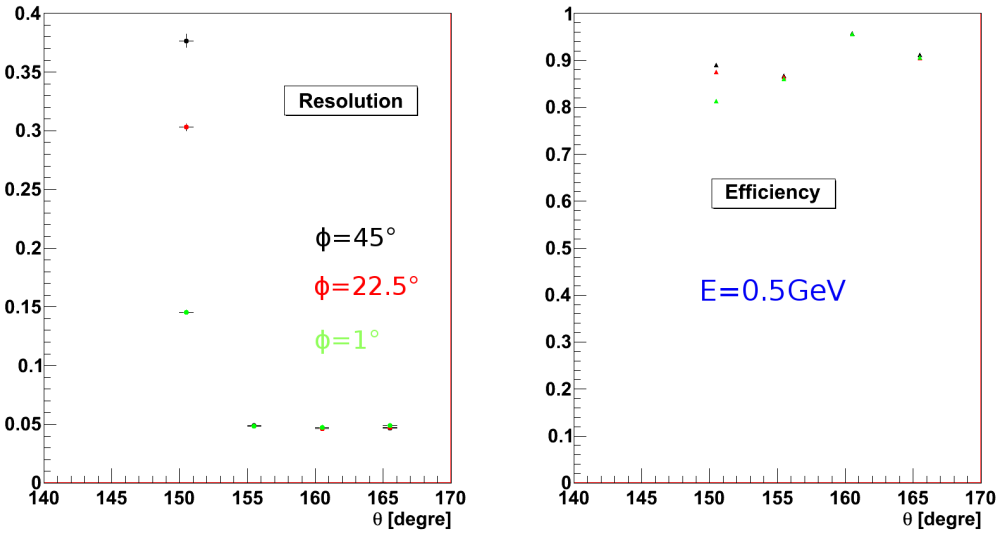

Figure 6.10: Resolution and efficiency at E=0.5 GeV. Black color stands for $\phi = 45°$, red for $\phi = 22.5°$ and green for $\phi = 1°$. Left hand picture presents the resolution and the right one the efficiency. One degree per bin.

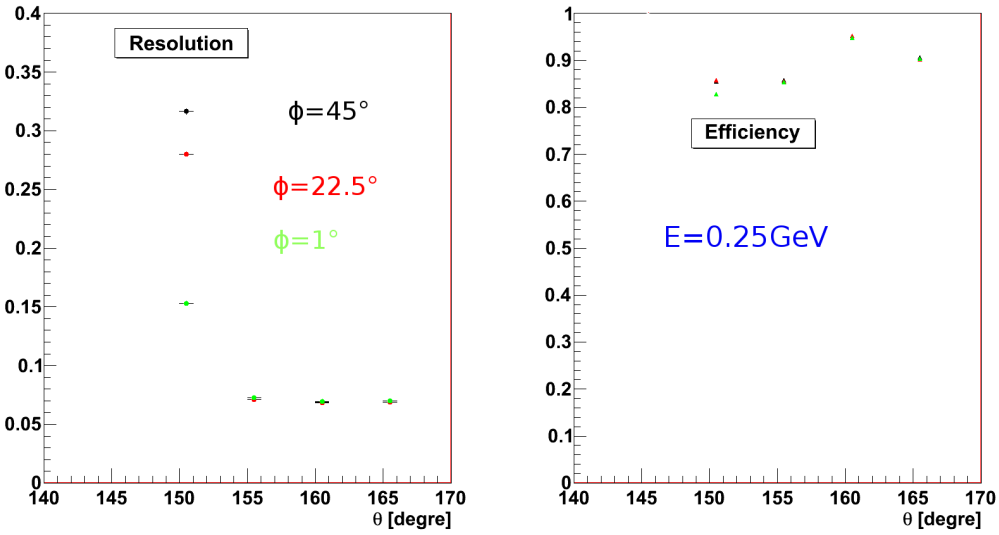

Figure 6.11: Resolution and efficiency at E=0.25 GeV. Black color stands for $\phi = 45°$, red for $\phi = 22.5°$ and green for $\phi = 1°$. Left hand picture presents the resolution and the right one the efficiency. One degree per bin.

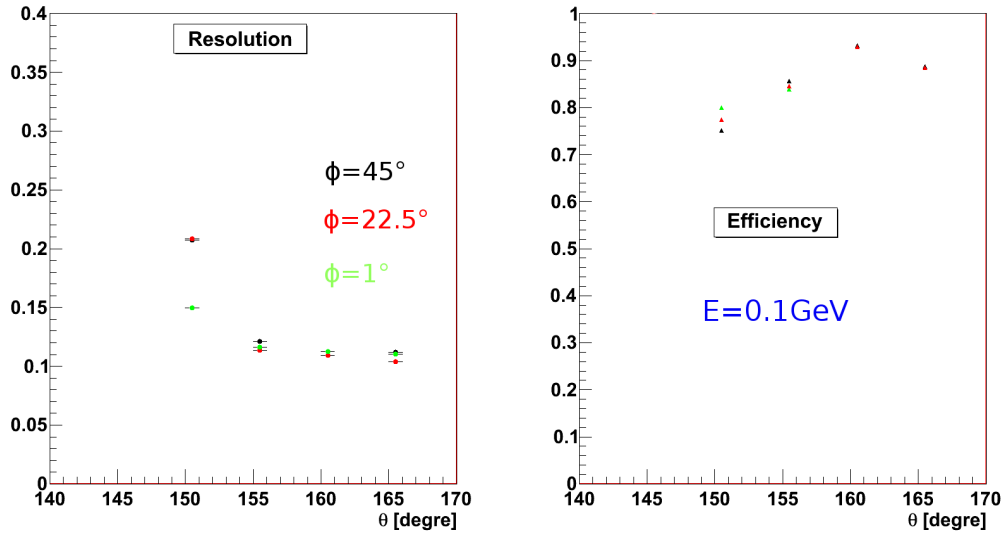

Figure 6.12: Resolution and efficiency at E=0.1 GeV. Black color stands for $\phi = 45°$, red for $\phi = 22.5°$ and green for $\phi = 1°$. Left hand picture presents the resolution and the right one the efficiency. One degree per bin.

Concerning the resolution, one can see that there is no point at $\theta = 145°$. Indeed, as no primary photons hit the backward end cap, no peak can be fitted on the spectra. Then looking to $\theta = 150°$, a bad resolution is obtained. In this case the fact is that the photons enter via the front face of the calorimeter but part of the shower could spread outside of the backward end cap (see Fig. 6.3) which implies bad energy reconstruction for the photon and therefore bad resolution. Consequently, the useful θ range would be from 155° to 165°. Furthermore, one can note that over this range the resolution does not seem to depend on the θ angle.

The resolution as a function of the energy of an electromagnetic calorimeter can be expressed as $\sigma/E = a/\sqrt{E} \oplus b/E \oplus c$ where a depends on the statistics, b on the electronic noise and c on the calibration. Since the digitalization process assumes a perfect calibration, the c must be 0. Fig. 6.13 shows the resolution σ/E as a function of the energy which once fitted gives a resolution $\sigma/E = 3.09/\sqrt{E} \oplus 0.5/E \oplus 0$ to compare to the expected resolution from section 2.2.2 of $\sigma/E \approx 1/\sqrt{E} \oplus 1$ (see also prototype results in Chapter 7).

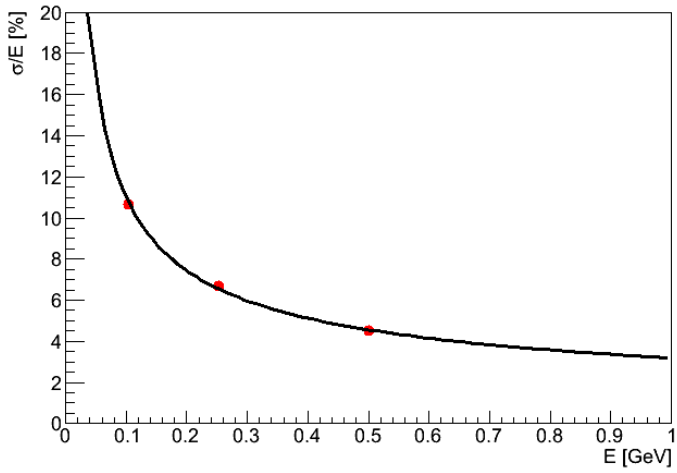

Figure 6.13: Backward end cap energy resolution obtained from simulation. Fit gives $\sigma/E = 3.09/\sqrt{E} \oplus 0.5/E \oplus 0$.

Concerning the efficiency, values are above 80% which is in principle very nice. A surprising point here is the high efficiency for $\theta = 160°$. Looking more in detail to the crossed material before the photons reach the backward end cap, one can see that in case of $\theta = 160°$ there is no crossed material (photons are shoot between the beam pipe and the MVD, see Fig. 6.14). Consequently, there is no photon conversion and higher efficiency. One should note that dead material like cables have not been implemented. Consequently the efficiency might slightly optimistic.

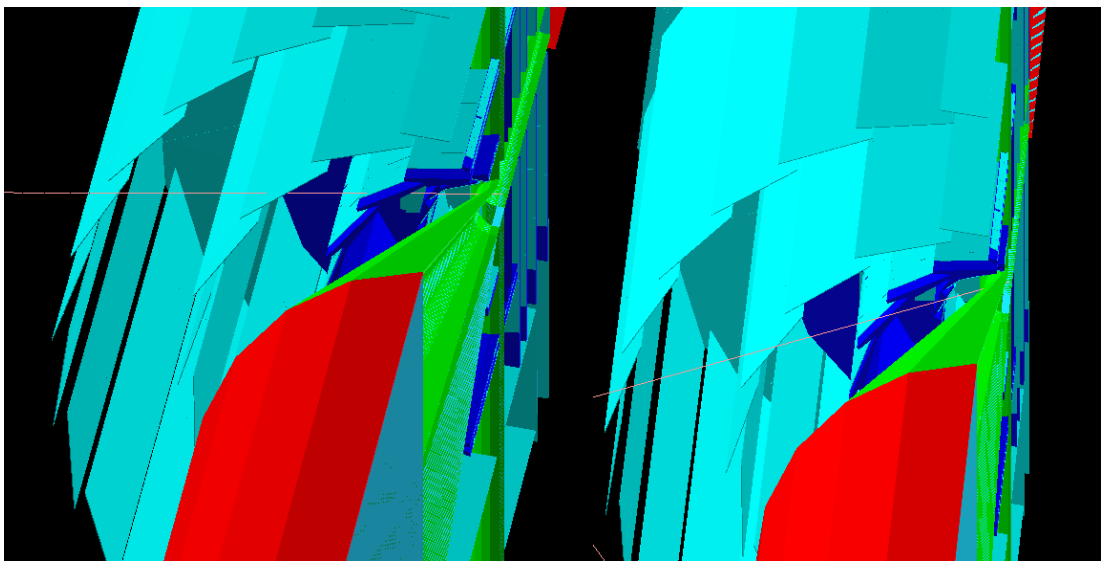

Figure 6.14: Crossed material in the MVD for $\phi = 45°$, on the left side $\theta = 155°$ and on the right side $\theta = 160°$. Pink track is photon track.

To conclude, the backward end cap has an effective coverage (i.e.: coverage with good resolution and efficiency) of $2\pi\left(cos155° - cos165°\right)/4\pi = 3\%$ of the total 4π.

Chapter 7

The proto60

Several test setups using real size components of the $\overline{\text{P}}$ANDA electromagnetic calorimeter have been constructed in order to validate the concepts of physics performance, mechanical stability, thermal robustness and integration into the $\overline{\text{P}}$ANDA solenoid together with other detector components. The most complete setup is the real size proto60.

7.1 General description

The 60 crystal prototype was constructed at the "Institut de Physique Nucléaire d´Orsay" (IPNO) in France (See Fig. 7.1). It can be divided in four parts: the 60 crystal block, the cooling system, the light pulse generator box and the electronic system. Those parts will be detailed as well as the the running of the prototype. Table 7.1 presents the used acronyms.

(a) High voltage and electronic

(b) 60 crystal block, cooling system and light pulse generator

Figure 7.1: 60 crystal prototype at Orsay, from [65].

Acronym	Description
Shaping	Signal shaper
Disc	Discriminator
ADC	Analog to Digital Converter
TDC	Time to Digital Converter
DAQ	Data AcQuisition
FEE	Front End Electronic
HV	High Voltage
APD	Avalanche Photo Diode

Table 7.1: Used acronyms.

7.1.1 The 60 crystal block

The 60 crystal block is made of 30 right crystals and 30 left crystals of $PbWO_4$. Crystals have a trapezoidal shape. Front face section is: 21,9x21,3 mm^2, rear face section is: 27,5x27,3 mm^2 and the crystal length is equal to 200 mm. The 60 crystals of the proto60 are positioned in 6 rows of 10 crystals. Each crystal is surrounded by VM2000 which is a reflecting polymer with a variable refractive index. The VM2000 is used to confine gammas inside scintillators. Crystals are grouped in 4 carbon alveoles. The overall carbon alveole system ensure the precise mechanical positioning of all crystals. Pre-amplifiers are then connected near the rear APD faces. After, pre-amplifiers output are linked to the motherboards which are themselves connected to the electronic acquisition system outside of cooling system. Fig. 7.2 shows on the left side a 3D representation of the block with carbon alveoles, crystals, avalanche photo diodes, light fibers and motherboards. On the right side, a picture of the rear face is presented. The use of light fibers will be explained in the light pulse generator part.

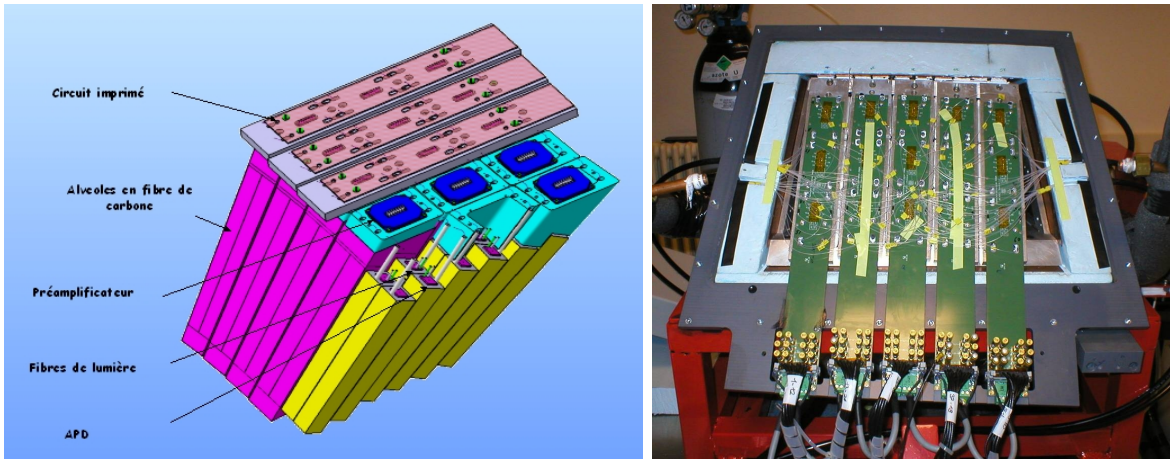

(a) 3D representation of the 60 crystal block (b) Rear face of the proto60

Figure 7.2: 60 crystal block, from [66].

7.1.2 Cooling system

The proto60 cooling system was developed in Orsay. It is a crucial part. PWO crystals have to be isolated and cooled down with a stability of 0.1°C. Crystal gain as well as APD gain strongly depends on temperature. The energy calibration will become more complex with temperature instabilities. Typically, those instabilities have to be at least five time smaller than $1/\sqrt{E}$ resolution. To control on-line variations of temperature, probes were positioned in key points. Tests showed that for a decrease of 8°C of ambient temperature (in real experiment the ambient temperature is also stabilized), the temperature variation inside the bloc is smaller than 0.5 degree.

7.1.3 Light pulse generator

Each crystal of the proto60 is connected via light fibers to the light pulse generator box. All the light fibers have the same characteristics (length, radius, ...), they are packed together and connected to the light pulse generator. It is assumed that, through the light fibers, the same amount of light is sent to each crystal. Furthermore, the box contains filters which allow to change on a large scale the amount of sent light. So, the light pulse generator box could in principle enable the energy calibration of the proto60.

7.1.4 Electronic system

The electronic system is composed of a shaping system (shapes signals), discriminators (DISC), a charge to digital converter (ADC) and a time to digital converter (TDC) to produce respectively energy and time informations for each signal. Finally the trigger requires a coincidence between one of the ten upper row crystals and one of the ten crystals of the lower row to save raw data via the acquisition system (DAQ).

Electronic pedestal corresponds to the measured peak value by the ADC without signal (i.e.: electronic "zero"). It is important to precisely know this value to determine the real physical measured one.

7.1.5 Data taking and analysis

First, when an event has been triggered, charge and time informations corresponding to the 60 crystals are saved into binary data. Then, raw data are obtained. The conversion software was developed by Peter Drexler[1] to go from the binary to raw data.

7.2 Beam tests with tagged photons

The proto60 has been tested under tagged photon beam in february 2009 thanks to the MAMI facility located at Mainz university (Germany). The present section will describe the MAMI facility as well as the experimental setup, then focus on the energy calibration and data analysis. Finally, results and resolution will be shown.

[1] Physikalisches Institut, Giessen Universität, Germany

7.2.1 MAMI facility

The development of a continuous wave electron accelerator was started at Mainz university around 1975. Thanks to the Race Track Microtron (RTM) scheme which allows to have multiple beam recirculations through the same accelerating unit, electrons of relatively high energy can be created. Based on this technology, MAMI B was constructed in 1990. Later in 2007, MAMI B was updated to an extended complex namely MAMI C. The proto60 was placed in the A2 hall. The parity violation experiment and the spectrometer hall are located in the A4 and A1 hall respectively. X-ray experiments are performed in the X1 hall.

7.2.1.1 MAMI B

MAMI B was constructed in 1990 and is based on a three-staged race track microtron cascade with an rf-linac as injector. A RTM is composed of one linac and two 180 bending magnets. After each recirculation, the electron will gain an energy ΔE but its curvature radius will also increase. This implies a maximum number of recirculations before extracting the electrons via one more magnet. MAMI B was able to produce a high quality beam of electron up to 882 MeV and 100 μA continuous wave.

7.2.1.2 MAMI C

MAMI C is an upgrade of MAMI B in order to reach higher electron beams (up to 1.538 GeV) by adding a fourth stage. This fourth stage consists into a Harmonic Double Sided Microtron (HDSM). The electron beam coming from MAMI B is used as injector of this fourth stage. The extracted electron beam from the HDSM will reach 1.508 GeV. The HDSM is composed by four 90 bending magnets and two linacs. After 43 recirculations, electron beam will go from 0.855 to 1.508 GeV. This beam is then sent to one of the three halls.

7.2.1.3 Tagged photons

Tagged photons are photons with a well defined energy. They are obtained from the MAMI C electron beam using the Glasgow photon tagging spectrometer. The incident electron beam goes through a radiator ($10\mu m$ thick Cu). Then, the outgoing electrons are bent to focal plane detectors via a 1.8 T magnet and photons are produced due to Bremsstrahlung effect. The focal plane detector is equipped with 353 overlapping plastic scintillators which cover an energy range from 5 to 95% of the beam energy. The tagged energy range covered by each detector is roughly constant. All the scintillators were glued and connected to photomultiplier tubes (PMT). Coupling the 1.508 GeV electron beam from MAMI C and the Glasgow photon tagging spectrometer, it provides tagged photons from 0.08 to 1.401 GeV with an energy resolution of 4 MeV.

7.2.2 Experimental setup

7.2.2.1 Beam settings

The proto60 was installed in the hall A2 and the electron beam used at its maximum energy (1.538 GeV) with an event rate around 320 event per second. Fifteen energy of tagged gammas were chosen in the allowed range (see Tab. 7.2).

Tag number γ energy (MeV)	1 1441	2 1357	3 1257	4 1157	5 1058	6 957	7 858	
Tag number γ energy (MeV)	8 757	9 657	10 557	11 456	12 356	13 256	14 158	15 189

Table 7.2: Energy of tagged photons

7.2.2.2 Tests

To take advantage of the available beam time (only 7 hours), the following options were tested:

1. run with the beam shooting the center of the crystal 35
2. run with the beam shifted by 5 mm in horizontal axis from the center of the crystal 35
3. run with the beam shifted by 10 mm in horizontal axis from the center of the crystal 35
4. run with the beam shooting the center of the crystal 35 adding a 2 mm lead sheet in front of the proto60
5. run with the beam shooting the center of the crystal 35 changing the electronic to KVI[2] one.

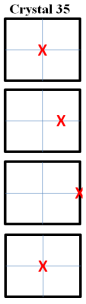

Figure 7.3: Beam positions

7.2.2.3 Proto60 settings

The proto60 was cooled at -25°C and each crystal individually calibrated for a gain 150.

[2]Nuclear physics institute in Groningen, Netherlands

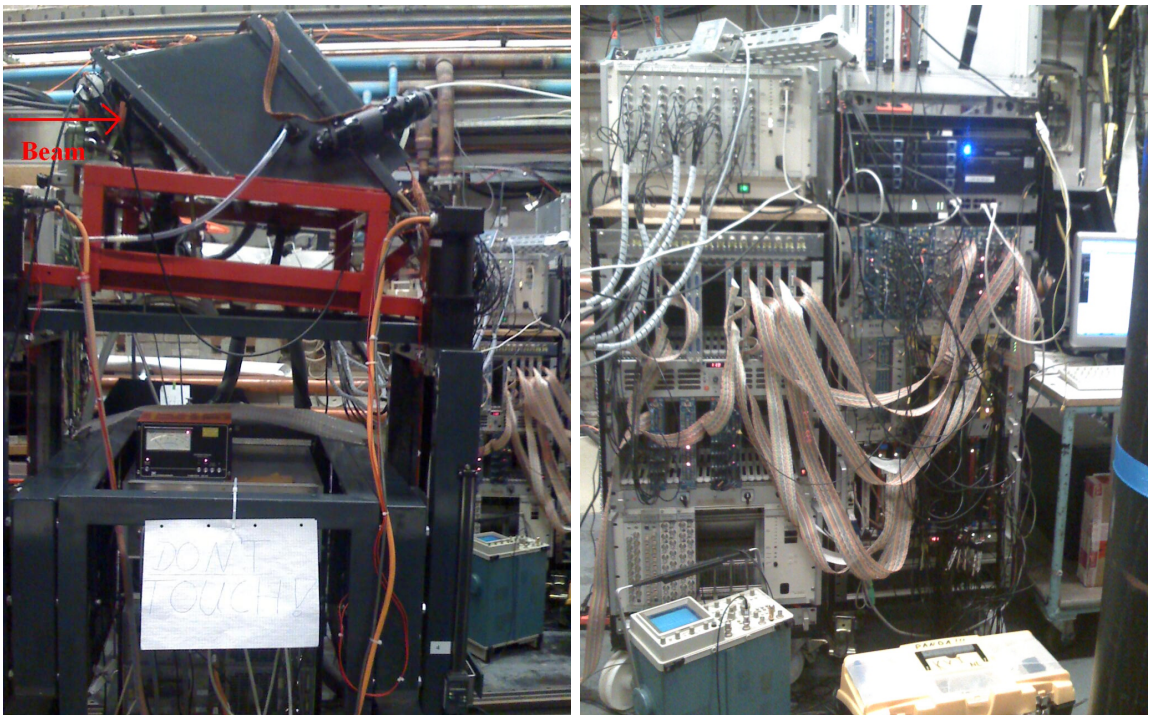

(a) Proto60 (b) Proto60 electronics

Figure 7.4: Proto60 at MAMI C, from [61].

7.2.3 Energy calibration methods

The idea is to use vertical cosmic rays to calibrate the prototype i.e. to determine the conversion factor (CF) from channels to MeV. Two different approaches are valid to take into account the energy distribution of the cosmic rays. The first one is based on the Bethe-Bloch formula (mean energy loss) whereas the second one is based on the Landau, Vavilov and Bichsel formula (most probable energy loss).

The conversion factor has been defined as follows: $\frac{(dE/dx) * \text{material density} * \text{crystal thickness}}{\text{number of channels}}$. Tab. 7.3 presents the notations and values used in the present chapter.

Symbol	Definition	Units or Value
ρ	$PbWO_4$ density	8.3 g cm^{-3}
x	Crystal thickness	2.42 cm
N_A	Avogadro´s number	6.0221415 10^{23} mol^{-1}
M_e	Electron mass	0.510998 MeV/c^2
M_μ	Incident particle mass : M_μ	105.658367 MeV/c^2
z	Incident particle charge	$\pm$ 1
r_e	Classical electron radius	2.8179403 fm
K	$4\pi N_A r_e^2 M_e c^2$	0.307075 $MeVg^{-1}cm^2$
Z/A	for $PbWO_4$	0.41315
I	Mean excitation energy	eV
$\delta(\beta\gamma)$	Density effect correction	

Table 7.3: Summary of the variables used in this section

7.2.3.1 Energy of cosmic rays

Fig. 7.5, taken from Ref. [67], shows $p^{1.7}dN/dp$ where p_μ is the cosmic ray momentum from different experiments. Unfortunately, its axis can not be handled easily. Therefore, data for cosmic rays at $\theta = 0°$ have been plotted in the following way dN/dp_μ depending on p_μ, see for instance Fig. 7.6. Fitting this plot, the most probable momentum of the cosmic rays is 2.5 GeV/c and the cosmic ray mean momentum is 4.289 GeV/c assuming that the tail stops at 20 GeV/c. Because of the effect of the tail cut (i.e.: choosing 10 GeV/c or 100 GeV/c instead of 20 GeV/c also changes the mean value), the precision on the mean momentum is lower than the one on the most probable momentum.

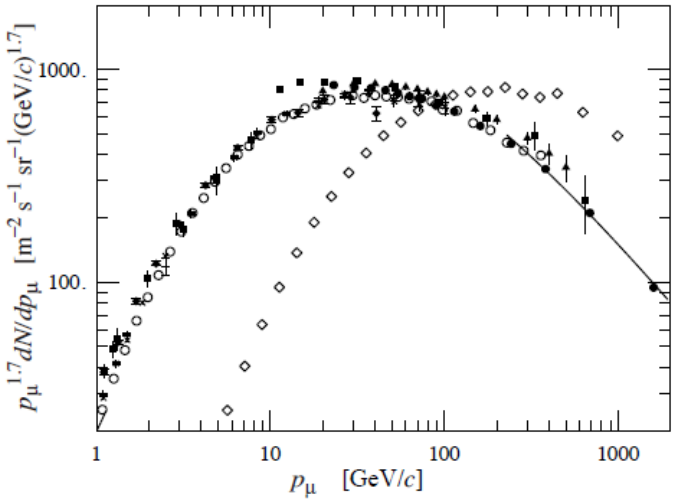

Figure 7.5: Spectrum of muons from Ref. [67] (⧫, ■, ▼, ▲, ×, +, ○ and ● correspond to cosmic rays at $\theta = 0°$ and ◊ to $\theta = 75°$).

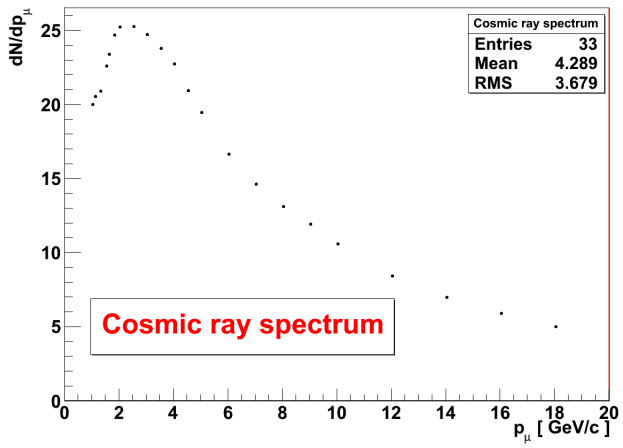

Figure 7.6: Cosmic ray spectrum (for cosmic rays at $\theta = 0°$ at sea level). From this plot are determined the most probable and the mean cosmic ray momenta.

7.2.3.2 Number of channels

To get this value, one needs to fit the pedestal as well as the deposit energy spectrum of the cosmic rays for each crystal. Gaussian fits have been used for the pedestal. Selecting vertical events (also called one-column events, Fig. 7.7), one limits the angular distribution of the cosmic rays crossing the crystals and the path length of the cosmic rays in each crystal. With this selection, the mean path length in each crystal is 2.42 cm. Then each deposit energy spectrum has been fitted using Landau curve. In this case, the most probable value is easy to get and different from the mean one (the MPV is one of the parameters of the Landau fit function). The mean value has been further determined using the counts in the spectrum. As an example, the Fig. 7.8 shows the raw data of the crystal 24 corresponding to one night of cosmic ray acquisition. One can note that the fits nicely agree with the data but also that the most probable value of the Landau is well defined whereas the mean one is less precise (again the tail cuts).

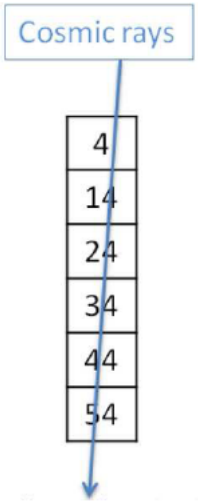

Figure 7.7: Vertical event

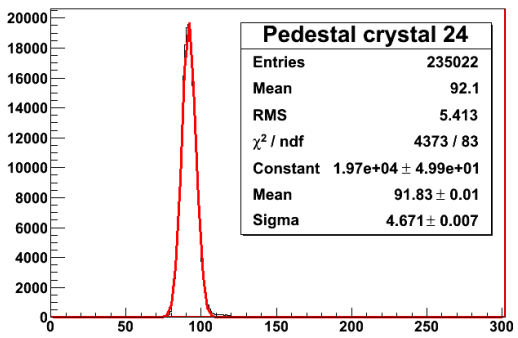

(a) Pedestal

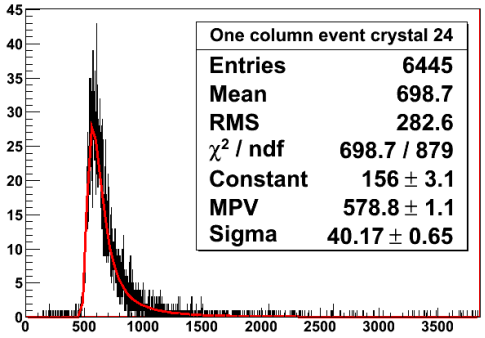

(b) One-column event signal

Figure 7.8: Raw data of the crystal 24. The MPV of the Landau is clearly different from the mean value.

7.2.3.3 Bethe-Bloch method

Here is the so-called Bethe-Bloch formula for the mean differential energy loss:

$$-\frac{dE}{dx} = Kz^2\frac{Z}{A}\frac{1}{\beta^2}\left\{\frac{1}{2}ln\left(\frac{2M_ec^2\beta^2\gamma^2T_{max}}{I^2}\right) - \beta^2 - \frac{\delta\left(\beta\gamma\right)}{2}\right\} \quad [\mathrm{MeVg^{-1}cm^2}] \tag{7.1}$$

where:

$$T_{max} = \frac{2M_ec^2\gamma^2\beta^2}{1 + \frac{2\gamma M_e}{M_\mu} + (\frac{M_e}{M_\mu})^2} \tag{7.2}$$

and

$$\delta(\beta\gamma) \text{ is the density effect correction.} \tag{7.3}$$

Assuming that the mean momentum of the incident cosmic rays is 4.289 GeV/c, the mean energy loss is 1.58 $\mathrm{MeVg^{-1}cm^2}$. Here, the density effect correction has been computed using Sternheimer´s parametrization [68]. Fig. 7.9 shows the energy losses as a function of the muon kinetic energy. Red dashed line corresponds to the Bethe-Bloch formula without the density correction and the red line to the Bethe-Bloch formula with the density correction.

To have the conversion factor for each crystal, only remains to use this dE/dx with the mean channel number of each crystal.

7.2.3.4 Landau, Vavilov, Bichsel method

For detector of moderate thickness x (in $\mathrm{gcm^{-2}}$), the energy loss probability distribution is well described by the Landau-Vavilov distribution [69]. The most probable energy loss for a detector with a thickness x is defined in the following way:

$$\Delta p = \xi \left[ln(\frac{2M_e c^2 \beta^2 \gamma^2}{I}) + ln(\frac{\xi}{I}) + j - \beta^2 - \delta(\beta\gamma) \right] \quad [\mathrm{MeVg^{-1}cm^3}] \tag{7.4}$$

where:

$$\xi = \frac{K}{2}\frac{Z}{A}\frac{x}{\beta^2},\ j = 0.200 \tag{7.5}$$

and

$$\delta(\beta\gamma) \text{ is the density effect correction.} \tag{7.6}$$

Normalizing Δp by x (here 2.42 cm) and assuming that the most probable cosmic ray momentum is 2.5 GeV/c, the most probable energy loss is 1.19 $\mathrm{MeVg^{-1}cm^2}$. Again, the density effect correction has been computed using Sternheimer´s parametrization. Fig. 7.9 shows the energy losses as a function of the muon kinetic energy. Black dashed line corresponds to the Bichsel formula without the density correction and the black line to the Bichsel formula with the density correction.

To have the conversion factor for each crystal, only remains to use this Δp/x with the most probable channel number of each crystal.

7.2.3.5 Sternheimer´s parametrization

This parametrization quantifies the density effect. In Ref. [68], one can find the analytic expression of $\delta(\beta\gamma)$ as follows:

$$\begin{aligned} \delta(\beta\gamma) &= 4.606x + C + a(x_1 - x)^m, && (x_0 < x < x_1) \\ \delta(\beta\gamma) &= 4.606x + C, && (x > x_1) \end{aligned}$$

where $x = log_{10}(p/M)$ of the incident particle and a, m, C are constants depending on the substance. Here a=0.136, m=2.71, C=-6.03, x_0=0.38 and x_1=3.0. Results are shown in Fig. 7.10.

7.2.3.6 Comparison

Fig. 7.9 presents a comparison between the Bethe-Bloch and the Bichsel formula. Full lines take into account the density correction whereas dashed one do not. One can see that the effect of the density correction is really important at the present energy and also that depending on the method used for the calibration, the energy loss value is quite different.

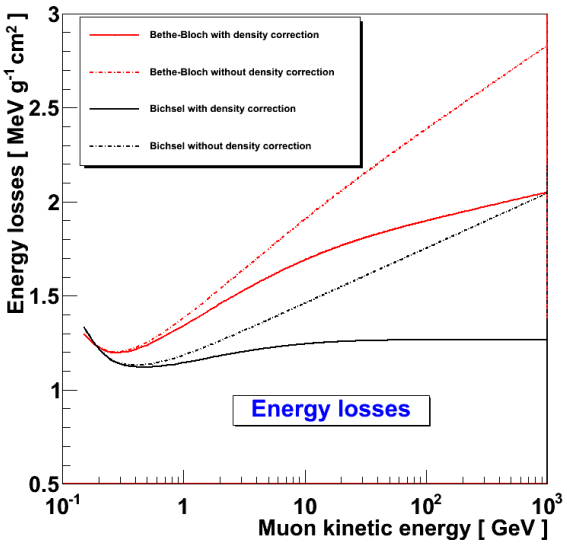

Figure 7.9: Energy losses obtained by the Bethe-Bloch formula (mean energy, red color) and by the Bichsel one (most probable energy, black color) by unit of crystal thickness. The full lines take into account the density correction using the Sternheimer´s parametrization whereas the dashed lines do not.

Furthermore, Fig. 7.10 shows the effect of the crystal thickness on $\Delta p/x$. From this picture, it can be concluded that selecting one column events, the variations of the path length of the cosmic rays through the crystals are small enough to not affect drastically the energy loss value.

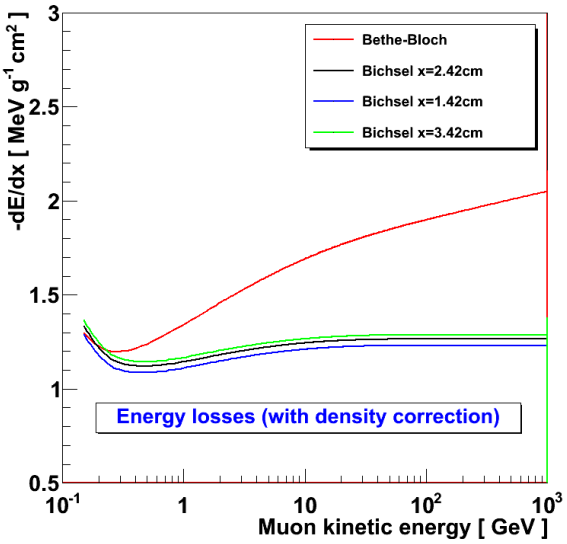

Figure 7.10: Energy losses calculated by the Bethe-Bloch formula (mean energy) and by the Bichsel one (most probable energy) by unit of crystal thickness. The full red and black lines are the same as in Fig. 7.9. The green and the blue one correspond to different crystal thicknesses.

As a consequence, the Bichsel method is used for the calibration using cosmic rays and data were analysed for all beam options.

7.2.4 Data analysis

7.2.4.1 Raw data

The Fig. 7.11 shows the raw data in case of the beam option 1. On the left hand, raw data are presented and pedestal as well as a few peaks can be seen. On the right side, an overlay of the results obtained when a coincidence with each tagger value is asked. On this figure, the 15 peaks corresponding to the 15 selected energies are clearly visible.

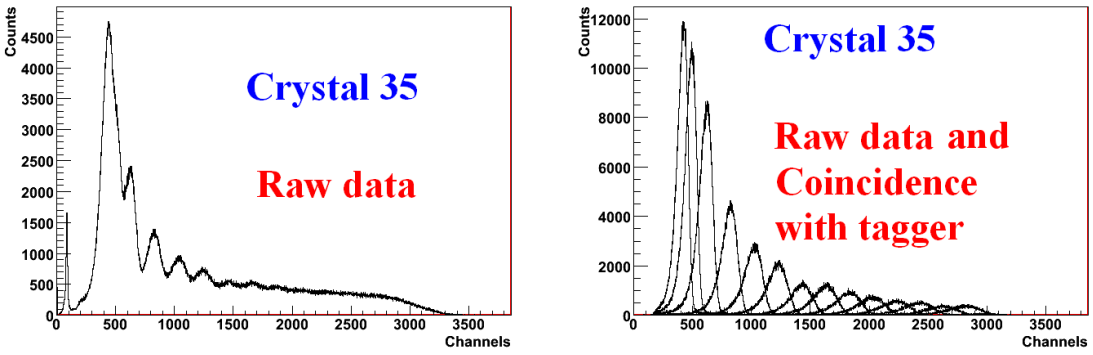

(a) Raw data (b) Raw data and coincidence with tagger

Figure 7.11: Crystal 35, raw data (beam at Mainz)

7.2.4.2 Energy deposit reconstruction

After a proper calibration of each crystal using the method previously described, the energy deposit of all tagged photons has to be reconstructed in order to compare the tagged energy with the reconstructed one. Usually, due to the shower extension over the neighbour crystals, the energy deposit in each crystal is summed over the matrix 3X3 or 5X5. The analysis has been done using 9, 25 and 60 crystals. But, only results for 60 crystals will be presented here (best case).

Fig. 7.12 presents the lineshape for the photons tagged at 1.057 GeV. Red curve stands for the spectrum of the crystal 35, the green one is the spectrum of the sum over the 59 other crystals. The black curve represents the sum over the 60 crystals.

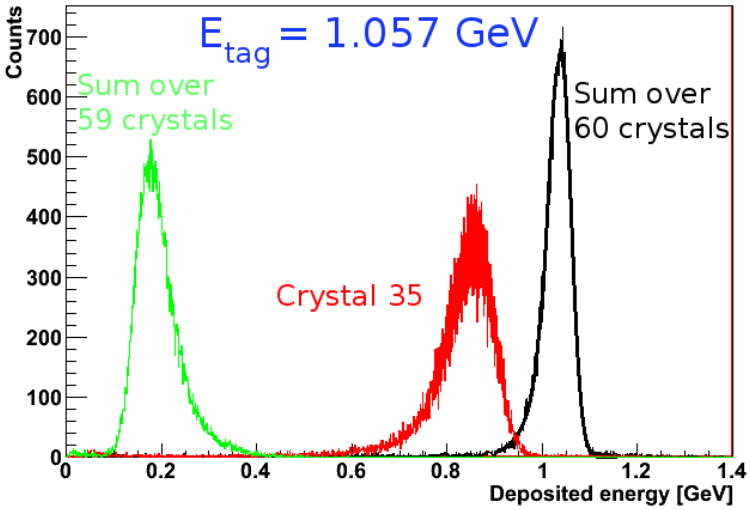

Figure 7.12: Lineshape of the deposit energy for $E_{tag} = 1.057$ GeV and beam option 1.

7.2.5 Results

7.2.5.1 Linearity

The first step was to fit the shape of the deposited energy (sum over the 60 crystals). The Gabler function has been used and defined in the following way:

$$f(E, FWHM_G, \lambda) = G + exp\left[\frac{(E - E_0}{\lambda}\right](1 - G)\ \theta(E_0 - E) \tag{7.7}$$

$$\text{where } G = exp\left[-\frac{4ln(2)(E - E_0)^2}{FWHM_G^2}\right], \tag{7.8}$$

$$\text{and } \theta(x) = 0 \text{ if } x < 0 \text{ else } \theta(x) = 1. \tag{7.9}$$

E_0 is the position of the maximum, λ describes the tail and G is a gaussian function.

In Fig. 7.13, one can see the measured energy (E_0 obtained via the Gabler fit) as a function of the tagged one. The red circles represent the peak positions obtained via the Gabler function. Those points have been fitted with a linear function ax+b. Results are good since a=0.9651 ± 0.0001 and b=0.01958 ± 0.00003.

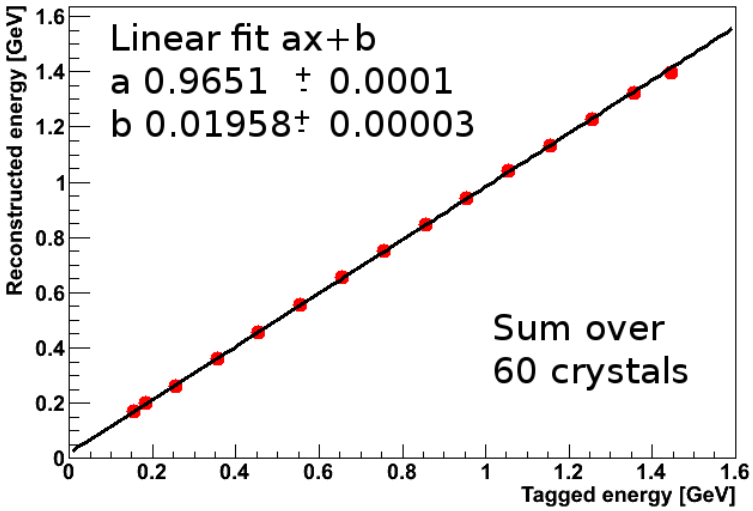

Figure 7.13: Deposited energy as a function of tagged energy for beam option 1. The linear fit shows good agreement.

7.2.5.2 Threshold

The resolution was determined as σ/E and the effect of the threshold on the deposited energy in each crystal. The Fig. 7.14 presents for two extreme cases: $E_{tag} = 0.158$ GeV and $E_{tag} = 1.441$ GeV, the resolution as a function of the threshold (from 0 to 2 MeV). The best results were found for a threshold of 0.7 MeV. Therefore, for the following results this threshold has been applied.

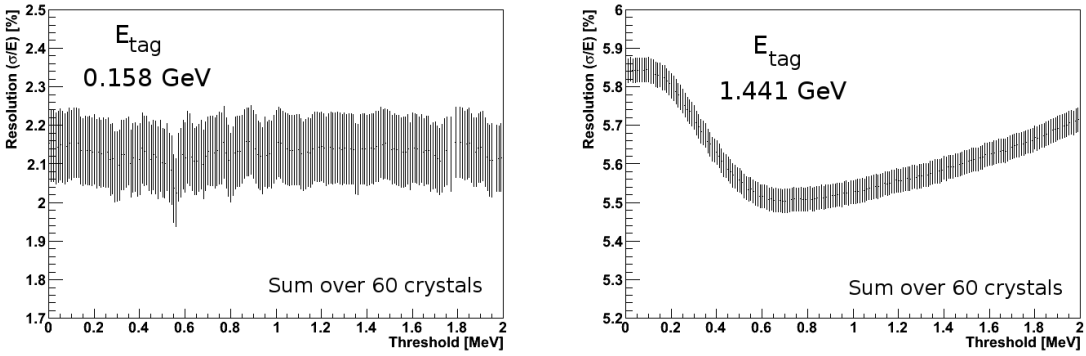

(a) $E_{tag} = 0.158$ GeV (b) $E_{tag} = 1.441$ GeV

Figure 7.14: Resolution as a function on the threshold applied on the deposit energy in each crystal (beam option 1). Best results for a 0.7 MeV threshold.

7.2.5.3 Resolution

The resolution of a calorimeter is typically: $\frac{\sigma}{E} = \frac{a}{\sqrt{E}} \oplus \frac{b}{E} \oplus c$, where a stands for the statistics, b for electronic noise and c for calibration errors as well as non-linearities. The Fig. 7.15 shows the resolution as a function of the tagged photons applying a threshold at 0.75 MeV on the deposit energy on each crystal (for beam option 1). Fit gives a=2.09, b=0.001 and c=1.33 which is slightly higher than the requirements (a <2% and c <1%). The resolution at 1 GeV is 2.47% which is better than the one obtained in the backward end cap simulations.

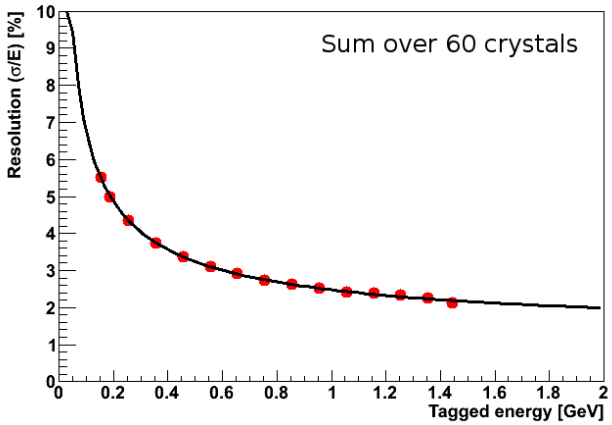

Figure 7.15: Energy resolution for beam option 1.

One can see in Fig. 7.16 the resolutions obtained for all beam options. Red color stands for the beam option 1, blue for beam option 2, pink for beam option 3 and green for beam option 4. Here the best case (beam option 1) and the worse case (beam option 3) are visible. Concerning the beam option 4, one can see that the lead sheet decreases the resolution at low energy but at high energy its effect is almost negligible.

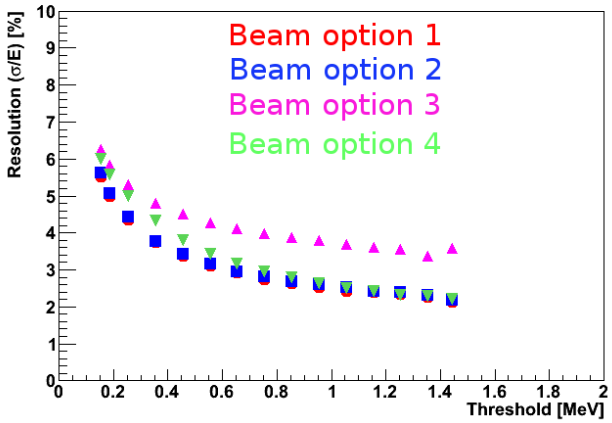

Figure 7.16: Energy resolution for all beam options.

Chapter 8

Conclusion and outlook

The $\overline{p}p \rightarrow \pi^{\circ}e^{+}e^{-}$ reaction has been proposed to access the proton electromagnetic form factors in the so-called unphysical region which is neither accessible via the electron-proton elastic scattering reaction nor via $\overline{p}p \leftrightarrow e^{+}e^{-}$ annihilation reactions. This thesis presents the feasibility of the $\overline{p}p \rightarrow \pi^{\circ}e^{+}e^{-}$ reaction with the future $\overline{\mathrm{P}}$ANDA detector and a related technical work devoted to the $\overline{\mathrm{P}}$ANDA electromagnetic calorimeter.

To describe the $\overline{p}p \rightarrow \pi^{\circ}e^{+}e^{-}$, a Lagrangian based approach was developed within the group. Assuming that the electron-positron pair comes from a virtual photon (spin 1), the 5-fold differential cross section was determined. The model has been constrained by the few available $\overline{p}p \rightarrow \pi^{\circ}\gamma$ data and the proton off-shellness is taken into account by introducing a form factor on the propagator. It was shown that the positron (or electron) angular distribution in the virtual photon rest frame is given by linear combinations of hadronic tensors which weight the spherical harmonic functions up to only L=2 (spin of γ^{*}=1).

Under the assumption of one nucleon exchange, the hadronic tensors were related to the nucleon electromagnetic form factors. Following the method developed in the feasibility studies of the $\overline{p}p \rightarrow e^{+}e^{-}$ reaction, an extraction method of the relevant quantities was developed. This method uses the shape of the positron (or electron) angular distribution in the virtual photon rest frame only and not the absolute normalization. It provides an access to the proton electromagnetic form factor ratio $R = |G_E|/|G_M|$ and for the first time in an unpolarized experiment to the cosine of the phase difference $cos(\varphi_E - \varphi_M)$. Such measurements have never been performed in the unphysical region up to now.

Studies were performed within a vector meson dominance parametrization of the proton electromagnetic form factors. It was found that at $T_{\overline{p}} = 1$ GeV is the most favourable case in terms of signal counting rates. Two q^2 values were studied in detail: $q^2 = 0.605 \pm 0.005$ $(\mathrm{GeV/c^2})^2$ which is close to the ω resonance and $q^2 = 2.0 \pm 0.125$ $(\mathrm{GeV/c^2})^2$ which is located in a structureless region. For these two q^2 regions and for 3 laboratory angular ranges of the θ_{π^0} ($10^{\circ} < \theta_{\pi^0} < 30^{\circ}$, $80^{\circ} < \theta_{\pi^0} < 100^{\circ}$ and $140^{\circ} < \theta_{\pi^0} < 160^{\circ}$), extended simulations were performed to determine the signal to background cross section ratio and the precision on the determination of R and $cos(\varphi_E - \varphi_M)$.

The $\overline{p}p \rightarrow \pi^{\circ}\pi^{+}\pi^{-}$ reaction has been considered as the most dangerous background. A first order model was developed and constrained by data from the LEAR experiment. At $q^2 = 0.605 \pm 0.005$ $(\mathrm{GeV/c^2})^2$ and $q^2 = 2.0 \pm 0.125$ $(\mathrm{GeV/c^2})^2$, the background to signal cross section ratio was estimated to be of the order of 10^4 and 10^7 respectively. The main experimental challenge is the rejection of this background. Combining particle identification information from the different detectors and kinematic fits, the background contribution can be reduced to the percent level or even less. The corresponding signal efficiency ranges from a few % to 30%. The precision on the determination of R and $cos(\varphi_E - \varphi_M)$ was determined using Monte Carlo method. Within the signal efficiency, the precision on R at $q^2 = 0.605 \pm 0.005$ $(\mathrm{GeV/c^2})^2$ is of the percent level whereas at $q^2 = 2.0 \pm 0.125$ $(\mathrm{GeV/c^2})^2$ it is few percent. The precision on $cos(\varphi_E - \varphi_M)$ is about 10% at $q^2 = 0.605 \pm 0.005$ $(\mathrm{GeV/c^2})^2$ and 20% at $q^2 = 2.0 \pm 0.125$ $(\mathrm{GeV/c^2})^2$.

When the $\overline{\mathrm{P}}$ANDA experiment will be running, all subdetectors must be tested and their capabilities precisely determined. These capabilities should then be compared to the one used in the simulations to validate the present feasibility study. One could then extrapolate this feasibility study to the Transition Distribution Amplitude (TDA) case since they are also related to the $\overline{p}p \rightarrow \pi^{\circ}e^{+}e^{-}$ reaction.

Since the $\overline{\mathrm{P}}$ANDA detector has an almost 4π coverage, the complete measurement of the $\overline{p}p \rightarrow \pi^{\circ}\gamma$ reaction at low antiproton beam kinetic energy would be of great interest. Indeed, these measurements are necessary since they would contribute in reaching a common and unified description of the $N \rightarrow N\pi$ vertex in similar kinematical conditions.

Another important work would be the measurement of hadronic channels over the whole phase space. The complete measurement of the $\overline{p}p \rightarrow \pi^{\circ}\pi^{+}\pi^{-}$ reaction at low antiproton kinetic energy must be compared to the model. The constraints provided up to now by the data are insufficient. Precise determination of the contribution of the different involved resonances is mandatory to provide precise angular dependances and correlations. This will allow to further improve on the cuts to reach the best possible signal to background ratio.

Finally, the measurement of the $\overline{p}p \rightarrow \pi^{\circ}e^{+}e^{-}$ differential cross section $d\sigma/dq^2$ may provide evidence of vector meson dominance at low q^2 energy. The complete measurement of the $\overline{p}p \rightarrow \pi^{\circ}e^{+}e^{-}$ reaction will allow to test the one nucleon exchange model developed here. In the feasibility study presented in this thesis, the proton form factors are assumed to be only q^2 dependent (on-shell proton). To test this hypothesis, it would be interesting to extract the ratio R and $cos(\varphi_E - \varphi_M)$ at a fixed q^2 for several s and $\theta_{\pi^{\circ}}$. One of the limitation of the model is the one nucleon exchange assumption. In particular, the extraction of R in the kinematical domain where $q^2 \gtrsim 4M_p^2$ from the $\overline{p}p \rightarrow \pi^{\circ}e^{+}e^{-}$ reaction must be compared to R extrated in other experiment from the $\overline{p}p \rightarrow e^{+}e^{-}$ and $e^{+}e^{-} \rightarrow \overline{p}p$ reactions. Any difference would be an evidence that the proton exchange is not dominant. If the one nucleon exchange is not the dominant diagram, one may need to add the N* or the Δ exchange diagrams. A deviation from a constant would mean either that the assumption is wrong or that the one proton exchange is not dominant in the whole kinematical domain.

Concerning the electromagnetic calorimeter, backward endcap simulations have shown a resolution σ/E of 3.1% at $E = 1$ GeV. The 60 crystal barrel prototype was also studied and data taken with a tagged photon beam were analysed. After proper calibration using cosmic rays, the resolution is determined to be $\sigma/E = 2.47\%$ at 1 GeV. This activity will continue with the construction of the full size electromagnetic calorimeter.

Appendix A

Acceptance and efficiency matrices

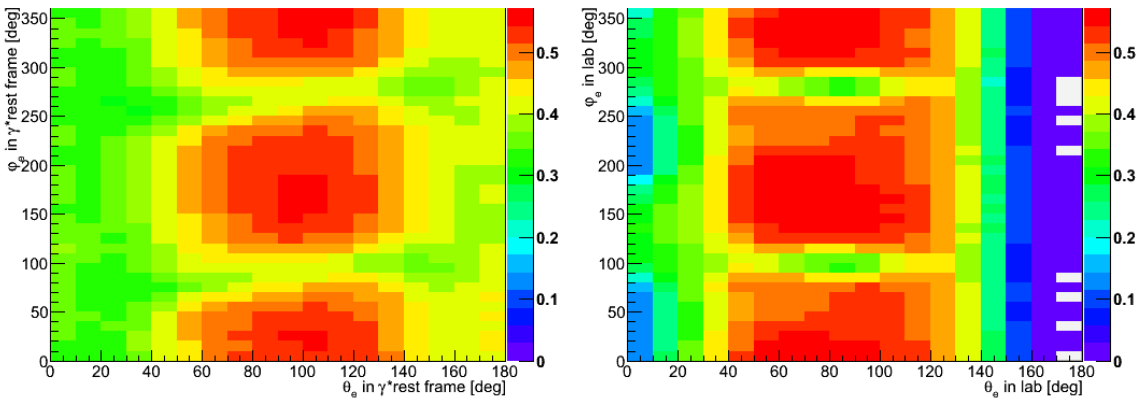

(a) in γ^* rest frame

(b) in laboratory frame

Figure A.1: Acceptance and efficiency matrices (PID cut only) for $q^2 = 2 \pm 0.125$ $(\mathrm{GeV/c^2})^2$ and $10° < \theta_{\pi^0} < 30°$ (with 10° bins for $\theta^*_{e^+}$ and $\varphi^*_{e^+}$).

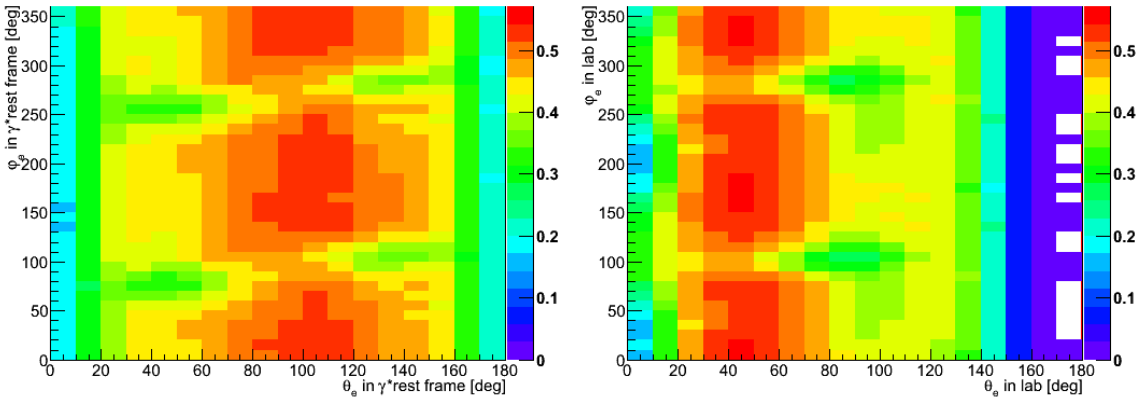

(a) in γ^* rest frame (b) in laboratory frame

Figure A.2: Acceptance and efficiency matrices (PID cut only) for $q^2 = 2 \pm 0.125$ $(\mathrm{GeV/c^2})^2$ and $80° < \theta_{\pi^0} < 100°$ (with 10° bins for $\theta^*_{e^+}$ and $\varphi^*_{e^+}$).

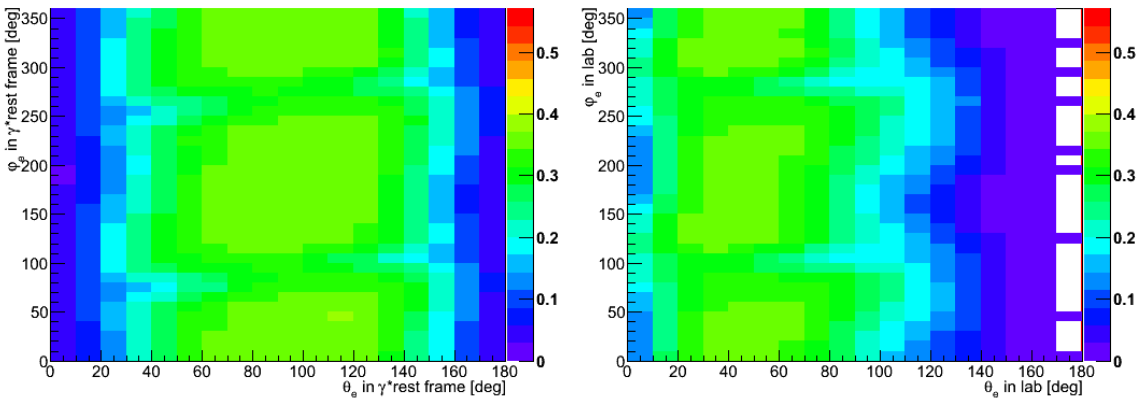

(a) in γ^* rest frame (b) in laboratory frame

Figure A.3: Acceptance and efficiency matrices (PID cut only) for $q^2 = 2 \pm 0.125$ $(\mathrm{GeV/c^2})^2$ and $140° < \theta_{\pi^0} < 160°$ (with 10° bins for $\theta^*_{e^+}$ and $\varphi^*_{e^+}$).

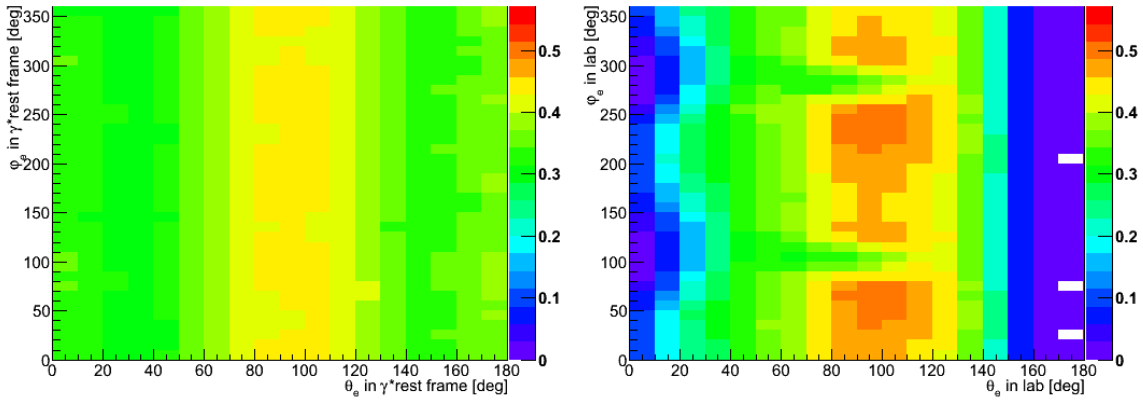

(a) in γ^* rest frame (b) in laboratory frame

Figure A.4: Acceptance and efficiency matrices (PID cut only) for $q^2 = 0.605 \pm 0.005$ $(\mathrm{GeV/c^2})^2$ and $10° < \theta_{\pi^0} < 30°$ (with 10° bins for $\theta^*_{e^+}$ and $\varphi^*_{e^+}$).

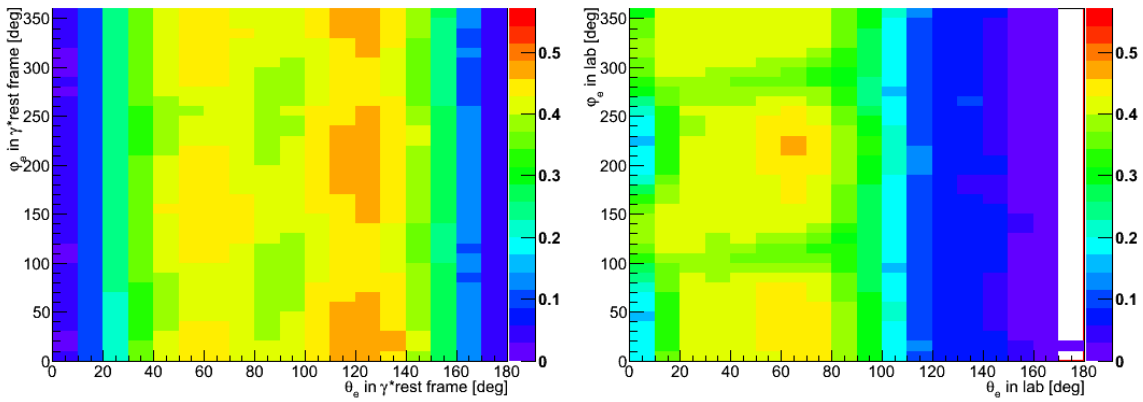

(a) in γ^* rest frame (b) in laboratory frame

Figure A.5: Acceptance and efficiency matrices (PID cut only) for $q^2 = 0.605 \pm 0.005$ $(\mathrm{GeV/c^2})^2$ and $80° < \theta_{\pi^0} < 100°$ (with 10° bins for $\theta^*_{e^+}$ and $\varphi^*_{e^+}$).

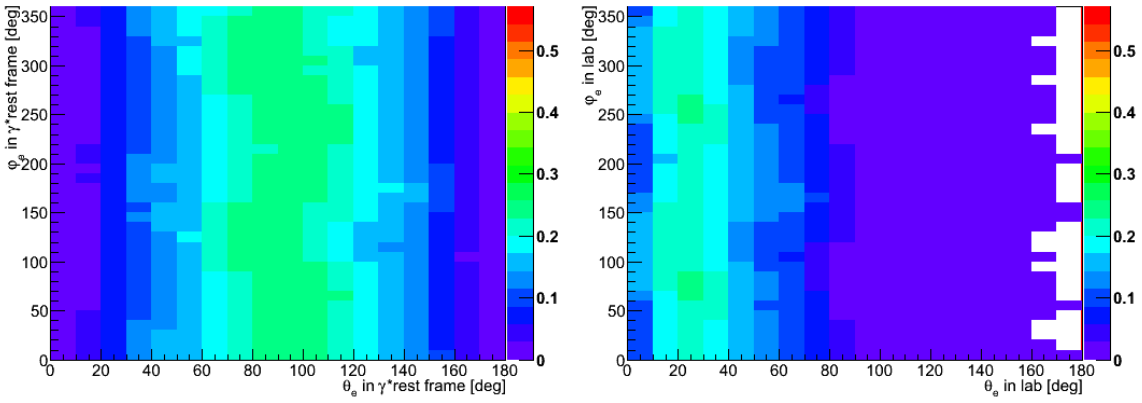

(a) in γ^* rest frame (b) in laboratory frame

Figure A.6: Acceptance and efficiency matrices (PID cut only) for $q^2 = 0.605 \pm 0.005$ $(\mathrm{GeV/c^2})^2$ and $140° < \theta_{\pi^0} < 160°$ (with 10° bins for $\theta^*_{e^+}$ and $\varphi^*_{e^+}$).

Bibliography

[1] FAIR Baseline Technical Report. http://www.fair-center.de/publications.171.0.html. 2006.

[2] $\overline{\text{P}}$ANDA webpage. http://www-panda.gsi.de/.

[3] CBM webpage. http://www.gsi.de/forschung/fair_experiments/cbm/1intro_e.html.

[4] NuSTAR webpage. http://www.gsi.de/forschung/fair_ experiments/nustar/projects_e.html.

[5] APPA webpage. http://www.fair-center.org/appa-physics.187.0.html.

[6] A. Dolinskii et al. Antiproton complex at the FAIR project. *NIM A*, 629:16–24, 2011.

[7] Physics performance report, March 2009. arXiv:0903.3905v1.

[8] M. Sudoł et al. Feasibility studies of the time-like proton electromagnetic form factor measurement with $\overline{\text{P}}$ANDA at fair. *Eur. Phys. J.*, A44:373–384, 2010.

[9] Technical Progress Report for $\overline{\text{P}}$ANDA: Strong Interaction Studies with Antiprotons. http://www.panda.gsi.de/archive/public/panda_tpr.pdf. $\overline{\text{P}}$ANDA Collaboration, 2005.

[10] Emc technical design report, October 2008. arXiv:0810.1216v1.

[11] CMS webpage. http://cms.web.cern.ch.

[12] R. W. Novotny et al. Stimulated recovery of the optical transmission of $PbWO_4$ scintillation crystals for electromagnetic calorimeters after radiation damage. *NIM A*, 623:1082–1085, 2010.

[13] R. W. Novotny et al. Performance of the prototype of the electromagnetic calorimeter for $\overline{\text{P}}$ANDA. *NIM A*, 648:77–91, 2011.

[14] M.J. Berger and S.M. Seltzer. Table of energy losses and ranges of electrons and positrons. Technical report, NASA-SP-3012, 1964.

[15] E. Longo and I. Sestili. Monte carlo calculation of photon-initiated electromagnetic showers in lead glass. *NIM*, 128:283–307, 1975.

[16] Solenoid and dipole spectrometer magnet (technical design report), 2009.

[17] M.P. Rekalo. *Sov. J. Nucl. Phys.*, 1:760, 1965.

[18] H. Fonvieille and V. A. Karmanov. Antiproton-nucleus electromagnetic annihilation as a way to access the proton time-like form factors. *Eur. Phys. J. A*, 42:287–298, 2009.

[19] O. Stern. *Nature*, 132:103, 1933.

[20] M.N. Rosenbluth. High energy scattering of electrons on protons. *Phys. Rev.*, 79:615–619, 1950.

[21] R. Hofstadter. Electron scattering and nuclear structure. *Rev. Mod. Phys.*, 28:214–254, 1956.

[22] S. Venkat et al. Relativistic transverse images of the proton charge and magnetic densities. *Phys. Rev. C*, 83:015203, 2011.

[23] E. Phragmén and E. Lendelöf. Sur une extension d´un principe classique de l´analyse et sur quelques propriétés des fonctions monogènes dans le voisinage d´un point singulier. *Acta Math.*, 31:381–406, 1908.

[24] L. Andivahis et al. Measurements of electric and magnetic form factors of the proton from Q^2=1.75 to 8.83 $(GeV/c)^2$. *Phys. Rev. D*, 50:5491, 1994.

[25] M. E. Christy et al. Measurements of electron-proton elastic cross sections for $0.4 < Q^2 < 5.5$ $(GeV/c)^2$. *Phys. Rev. C*, 70:015206, 2004.

[26] I. A. Qattan et al. Precision Rosenbluth measurement of the proton elastic form factors. *Phys. Rev. Lett.*, 94:142301, 2005.

[27] C. F. Perdrisat et al. Nucleon electromagnetic form factors. *Prog. Part. Nucl. Phys.*, 59:694–764, 2007.

[28] P. E. Bosted. Empirical fit to the nucleon electromagnetic form factors. *Phys. Rev. C*, 51:409–411, 1995.

[29] M.K. Jones et al. G_{E_p}/G_{M_p} ratio by polarization transfer in $\overrightarrow{e}p \to e\overrightarrow{p}$. *Phys. Rev. Lett.*, 84:1398–1402, 2000.

[30] O. Gayou et al. Measurement of G_{E_p}/G_{M_p} in $\overrightarrow{e}p \to e\overrightarrow{p}$ to q^2=5.6 GeV^2. *Phys. Rev. Lett.*, 88:092301, 2002.

[31] A. J. R. Puckett et al. Recoil polarization measurements of the proton electromagnetic form factor ratio to Q^2=8.5 GeV^2. *Phys. Rev. Lett.*, 104:242301, 2010.

[32] B. Aubert et al. Study of $e^+e^- \to p\overline{p}$ using initial state radiation with BABAR. *Phys. Rev. D*, 73:012005, 2006.

[33] G. Bardin et al. *Nucl. Phys. B*, 411:3, 1994.

[34] J. J. Sakurai. Vector meson dominance and high energy electron-proton inelastic scattering. *Phys. Rev. Lett.*, 22:981–984, 1969.

[35] F. Iachello and Q. Wan. Structure of the nucleon from electromagnetic time-like form factors. *Phys. Rev. C*, 69(055204):055204, 2004.

[36] F. Iachello et al. Semi-phenomenological fits to nucleon form factors. *Phys. Lett. B*, 43:191–196, 1973.

[37] W. R. Frazer and J. R. Fulco. Effect of a pion-pion scattering resonance on nucleon structure. *Phys. Rev. Lett.*, 2(8):1959, April 1959.

[38] C. Adamuščín et al. Testing axial and electromagnetic nucleon form factors in time-like regions in the processes $\overline{p}+n \to \pi^- + l^- + l^+$ and $\overline{p}+p \to \pi^0 + l^- + l^+$, $l = e, \mu$. *Phys. Rev. C*, 75(045205):045205, 2007.

[39] M. Ablikim et al. Measurements of the cross section for $e^+e^- \to p\overline{p}$ at center-of-mass energies from 2.0 to 3.07 GeV. *Phys. Lett. B*, 630:14, 2005.

[40] M. Ambrogiani et al. Measurements of the magnetic form factor of the proton in the time-like region at large momentum transfer. *Phys. Rev. D*, 60:032002, 1999.

[41] M. Andreotti et al. Measurements of the magnetic form factor of the proton for the time-like momentum transfers. *Phys. Lett. B*, 559:20–25, 2003.

[42] A. Zichichi et al. *Nuovo Cim.*, 24:170, 1962.

[43] E. Tomasi-Gustafsson et al. Nucleon electromagnetic form factors and polarization observables in space-like and time-like regions. *Eur. Phys. J. A*, 24:419–430, 2005.

[44] T. A. Armstrong et al. Two-body neutral final states produced in antiproton-proton annihilations at $2.911 < \sqrt{s} < 3.686$ GeV. *Phys. Rev. D*, 56:2509–2531, 1997.

[45] A. Berglund et al. A study of the reaction $\overline{p}p \to \pi^-\pi^+$ at 10 GeV/c. *Nucl. Phys. B*, 137:276, 1978.

[46] C. Baglin et al. Measurement of the $\pi^\circ\pi^\circ$ cross section in $\overline{p}p$ annihilations at $\sqrt{s} \approx 3.0$ GeV/c. *Nucl. Phys. B*, 368:175, 1999.

[47] T. Buran et al. Antiproton-proton annihilation into $\pi^+\pi^-$ and k^+k^- at 6.2 GeV/c. *Nucl. Phys. B*, 116:51, 1976.

[48] R. S. Dulude et al. Measurement of $\overline{p}p \to \pi^\circ\pi^\circ, \quad \pi^\circ\eta^\circ$ in the t and u-meson region. *Phys. Lett. B*, 79:329, 1978.

[49] E. Eisenhandler et al. Measurement of differential cross sections for antiproton-proton annihilation into charged pion and kaon pairs between 0.79 and 2.43 GeV/c. *Nucl. Phys. B*, 96:109, 1975.

[50] V. A. Matveev et al. Automodellism in the large-angle elastic scattering and structure of hadrons. *Lett. Nuovo. Cim.*, 7:719, 1973.

[51] S. J. Brodsky and G. R. Farrar. Scaling laws at large transverse momentum. *Phys. Rev. Lett.*, 31:1153, 1973.

[52] E. L. Lomon. Effect of recent Rp and Rn measurements on extended Gari-Krumpelmann model fits to nucleon electromagnetic form factors. *Phys. Rev. C*, 66:045501, 2002.

[53] E. Tomasi-Gustafsson et al. Nucleon electromagnetic form factors and polarization observables in space-like and time-like regions. *Eur. Phys. J. A*, 24:419, 2005.

[54] G. I. Gakh et al. Polarization effects in $\overline{N} + \mathrm{N} \to \pi^0 + l^- + l^+$ reaction: General analysis and numerical estimations. *Phys. Rev. C*, 83:025202, 2011.

[55] J.P. Lansberg et al. Production of a pion in association with a high-Q^2 dilepton pair in antiproton-proton annihilation at gsi-fair. *Phys. Rev. D*, 76(111502):111502, 2007.

[56] J. Van de Wiele. Private communication.

[57] R. Kunne. Private communication.

[58] A. Dbeyssi and E. Tomasi-Gustafsson. Classification of $\overline{p} + p$ induced reactions. Internal note.

[59] J. Van de Wiele and S. Ong. Regge description of two pseudoscalar meson production in antiproton-proton annihilation. *Eur. Phys. J. A*, 46:291–298, 2010.

[60] T. Liu. Study of the resolution effect in $\overline{p}p \to e^+e^-\pi^0$ with the detector $\overline{\text{P}}$ANDA. Internal note.

[61] M. Sudoł. Private communication.

[62] T. C. Bacon et al. $\overline{p}p$ annihilations into $\pi^+\pi^-$, k^+k^-, $\pi^+\pi^-\pi^\circ$, and $\pi^+\pi^-$ + neutrals near center-of-mass energy 2200 MeV. *Phys. Rev. D*, 7:No. 3, 1973.

[63] D. Khaneft. Private communication.

[64] D. Rodriguez. Private communication.

[65] T. Hennino. Private communication.

[66] P. Rosier. Private communication.

[67] Journal of Physics G. Nuclear and particle physics. Review of Particle Physics, Vol 33, July 2006.

[68] R. M. Sternheimer. The density effect for the ionization loss in various materials. *Phys. Rev.*, 88(4):851–859, November 1952.

[69] H. Bichsel. Straggling in thin silicon detectors. *Rev. Mod. Phys*, 60(3):663–699, July 1988.

Abstract

Among all possible realizations of quark and antiquark assembly, the nucleon (the proton and the neutron) is the most stable of all hadrons and consequently has been the subject of intensive studies. Mass, shape, radius and more complex representations of its internal structure are measured since several decades using different probes. The proton (spin 1/2) is described by the electric G_E and magnetic G_M form factors which characterise its internal structure. The simplest way to measure the proton form factors consists in measuring the angular distribution of the electron-proton elastic scattering accessing the so-called Space-Like region where $q^2 \leq 0$. Using the crossed channel $\overline{p}p \leftrightarrow e^+e^-$, one accesses another kinematical region, the so-called Time-Like region where $q^2 > 0$. However, due to the $\overline{p}p \leftrightarrow e^+e^-$ threshold q^2_{th}, only the kinematical domain $q^2 > q^2_{th} > 0$ is available. To access the unphysical region, one may use the $\overline{p}p \rightarrow \pi^\circ e^+e^-$ reaction where the π° takes away a part of the system energy allowing q^2 to be varied between q^2_{th} and almost 0. This thesis aims to show the feasibility of such measurements with the PANDA detector which will be installed on the new high intensity antiproton ring at the FAIR facility at Darmstadt.

To describe the $\overline{p}p \rightarrow \pi^\circ e^+e^-$ reaction, a Lagrangian based approach is developed. The 5-fold differential cross section is determined and related to linear combinations of hadronic tensors. Under the assumption of one nucleon exchange, the hadronic tensors are expressed in terms of the 2 complex proton electromagnetic form factors. An extraction method which provides an access to the proton electromagnetic form factor ratio $R = |G_E|/|G_M|$ and for the first time in an unpolarized experiment to the cosine of the phase difference is developed. Such measurements have never been performed in the unphysical region up to now. Extended simulations were performed to show how the ratio R and the cosine can be extracted from the positron angular distribution. Furthermore, a model is developed for the $\overline{p}p \rightarrow \pi^\circ\pi^+\pi^-$ background reaction considered as the most dangerous one. The background to signal cross section ratio was estimated under different cut combinations of the particle identification information from the different detectors and of the kinematic fits. The background contribution can be reduced to the percent level or even less. The corresponding signal efficiency ranges from a few % to 30%. The precision on the determination of the ratio R and of the cosine is determined using the expected counting rates via Monte Carlo method. A part of this thesis is also dedicated to more technical work with the study of the prototype of the electromagnetic calorimeter and the determination of its resolution.

Résumé

Parmi toutes les configurations d'agrégats de quark et d'antiquark, le nucléon (le proton et le neutron) est le plus stable des hadrons et a été par conséquent le sujet d'études intensives. Sa masse, sa forme, son rayon et des représentations plus complexes sont mesurés depuis plusieurs décennies grâce à différentes sondes. Le proton (spin 1/2) est décrit par les facteurs de forme électrique et magnétique qui caractérisent sa structure interne. Le moyen le plus simple de mesurer les facteurs de forme consiste à mesurer la distribution angulaire de la diffusion élastique électron-proton: dans cette région dite espace q^2 est négatif. En utilisant la réaction croisée $\overline{p}p \leftrightarrow e^+e^-$, on atteint une autre région cinématique appelée région temps où $q^2 > 0$. Cependant, à cause du seuil q^2_{th} de les réactions $\overline{p}p \leftrightarrow e^+e^-$, seul le domaine cinématique $q^2 > q^2_{th} > 0$ est autorisé. Pour atteindre la région non physique, on utilise la réaction $\overline{p}p \rightarrow \pi^\circ e^+e^-$ où le π° emporte une partie de l'énergie autorisant ainsi q^2 à varier entre q^2_{th} et presque 0. Cette thèse vise à démontrer la faisabilité de ces mesures avec le détecteur $\overline{\mathrm{P}}$ANDA qui sera installé sur le nouvel anneau d'antiprotons à haute intensité du futur complexe accélérateur FAIR à Darmstadt.

Pour décrire la réaction $\overline{p}p \rightarrow \pi^\circ e^+e^-$ une approche basée sur des lagrangiens est développée. La section efficace 5 fois différentielle est determinée et reliée à des combinaisons linéaires de tenseurs hadroniques. Sous l'hypothèse de l'échange d'un nucléon, les tenseurs hadroniques sont exprimés en fonctions des 2 facteurs de forme électromagnétiques complexes du proton. Une méthode est développée, qui donne accès au rapport des facteurs de forme électromagnétiques du proton $R = |G_E|/|G_M|$ et pour la première fois avec une expérience non polarisée au cosinus de la différence de phase. A ce jour, de telles mesures n'ont jamais été faites dans la région non physique. Des simulations détaillées ont été effectuées pour montrer comment le rapport R et le cosinus peuvent être extraits de la distribution angulaire du positron. De plus, un modèle est développé pour la réaction parasite $\overline{p}p \rightarrow \pi^\circ\pi^+\pi^-$ considérée comme la plus dangereuse. Le rapport des sections efficaces est estimé pour différentes coupures combinant l'identification de particules et les fits cinématiques. La contribution du bruit de fond peut être réduite à quelques pour-cent voire moins. L'efficacité typique de détection du signal correspondante varie de l'ordre de 5 pour-cent à 30 pour-cent. La précision sur la détermination du rapport R et du cosinus est determinée pour le nombre de coups attendu via la méthode Monte Carlo. Une partie de cette thèse est aussi dédiée à un travail plus technique avec l'étude du prototype du calorimètre électromagnétique et la détermination de sa résolution.

Zusammenfassung

Unter allen möglichen Anwendungen von Quark und Antiquark Montage ist das Nukleon (das Proton und das Neutron) das stabilste aller Hadronen und folglich war es Gegenstand intensiver Untersuchungen. Masse, Form, Radius und komplexe Darstellungen von seiner inneren Struktur sind seit mehreren Jahrzehnten mit verschiedenen Sonden gemessen worden. Das Proton (Spin 1/2) ist durch die elektrischen G_E und magnetischen G_M Formfaktoren, die die interne Struktur charakterisieren, beschrieben. Der einfachste Weg um die Formfaktoren der Protonen zu messen, besteht aus der Messung der Winkelverteilung der elastischen Streuung des eptoep, zugreifend auf die sogenannte Space-Like Region, wo $q^2 \leq 0$ ist. Mit dem Cross-Channel $\overline{p}p \leftrightarrow e^+e^-$, greift die kinematische Region, die sogenannte Time-Like Region, wo $q^2 > 0$ ist. Aufgrund der $\overline{p}p \leftrightarrow e^+e^-$ Schwelle q^2_{th}, ist allerdings nur die kinematische Domain $q^2 > q^2_{th} > 0$ verfügbar. Um auf die unphysikalische Region zuzugreifen, kann man mit die $\overline{p}p \rightarrow \pi^\circ e^+e^-$ Reaktion nutzen, bei der π° einen Teil der Systemenergie nimmt, was erlaubt q^2 zwischen q^2_{th} bis nahezu 0 zu variieren. Diese Arbeit zielt darauf hin, die Durchführbarkeit solcher Messungen mit dem PANDA-Detektor zu zeigen, der auf dem neuen hochintensiven Antiproton-Ring an der FAIR-Anlage installiert werden soll in Darmstadt.

Zur Beschreibung der $\overline{p}p \rightarrow \pi^\circ e^+e^-$ Reaktion wird ein Lagrange-Ansatz entwickelt. Der 5-fache Differentialquerschnitt ist bestimmt und verwandt mit linearen Kombinationen von hadronischen Tensoren. Unter der Annahme eines Nukleonenaustauschs sind die hadronischen Tensoren in Bezug auf das 2-Komplex-Proton elektromagnetischer Formfaktoren wiedergegeben. Eine Extraktionsmethode, die einen Zugriff auf des Protons elektromagnetische Formfaktorverhältnis $R = |G_E|/|G_M|$ bietet und zum ersten Mal in einem unpolarisierten Experiment ist um Cosinus die Phasenverschiebung entwickelt. Solche Messungen wurden bis heute noch nie in der unphysikalischen Region durchgeführt. Es wurden erweiterte Simulationen durchgeführt um zu zeigen, wie das Verhältnis R und der Cosinus von der Positronen-Winkelverteilung extrahiert werden können. Darüber hinaus ist ein Modell für die $\overline{p}p \rightarrow \pi^\circ\pi^+\pi^-$ Hintergrundreaktion entwickelt, die als die gefährlichste betrachtet wird. Der Hintergrund zum Querschnittsverhältnissignal wurde unter verschiedenen Kombinationen von Schnitten der Teilchenidentifizierungsinformationen aus den verschiedenen Detektoren und kinematischen Passformen geschätzt. Die Hintergrundsdistribution kann auf das Prozent-Niveau oder sogar noch weniger reduziert werden. Die entsprechende Signaleffizienz reicht von wenigen % bis 30%. Die Genauigkeit der Bestimmung des Verhältnisses R und des Cosinus wird anhand der erwarteten Zählraten über die Monte-Carlo-Methode ermittelt. Ein Teil dieser Arbeit ist auch mehr der technischen Arbeit mit dem Studium des Prototyps der elektromagnetischen Kalorimeter und der Bestimmung ihrer Auflösung gewidmet.